

Universiteit
Leiden
The Netherlands

From the macro- to the microvasculature : temporal and spatial visualization using arterial spin labeling

Suzuki, Y.

Citation
Suzuki, Y. (2018, November 1). *From the macro- to the microvasculature : temporal and spatial visualization using arterial spin labeling*. Retrieved from https://hdl.handle.net/1887/66665

Version:	Not Applicable (or Unknown)
License:	Licence agreement concerning inclusion of doctoral thesis in the Institutional Repository of the University of Leiden
Downloaded from:	https://hdl.handle.net/1887/66665

Note: To cite this publication please use the final published version (if applicable).

Cover Page



Universiteit Leiden

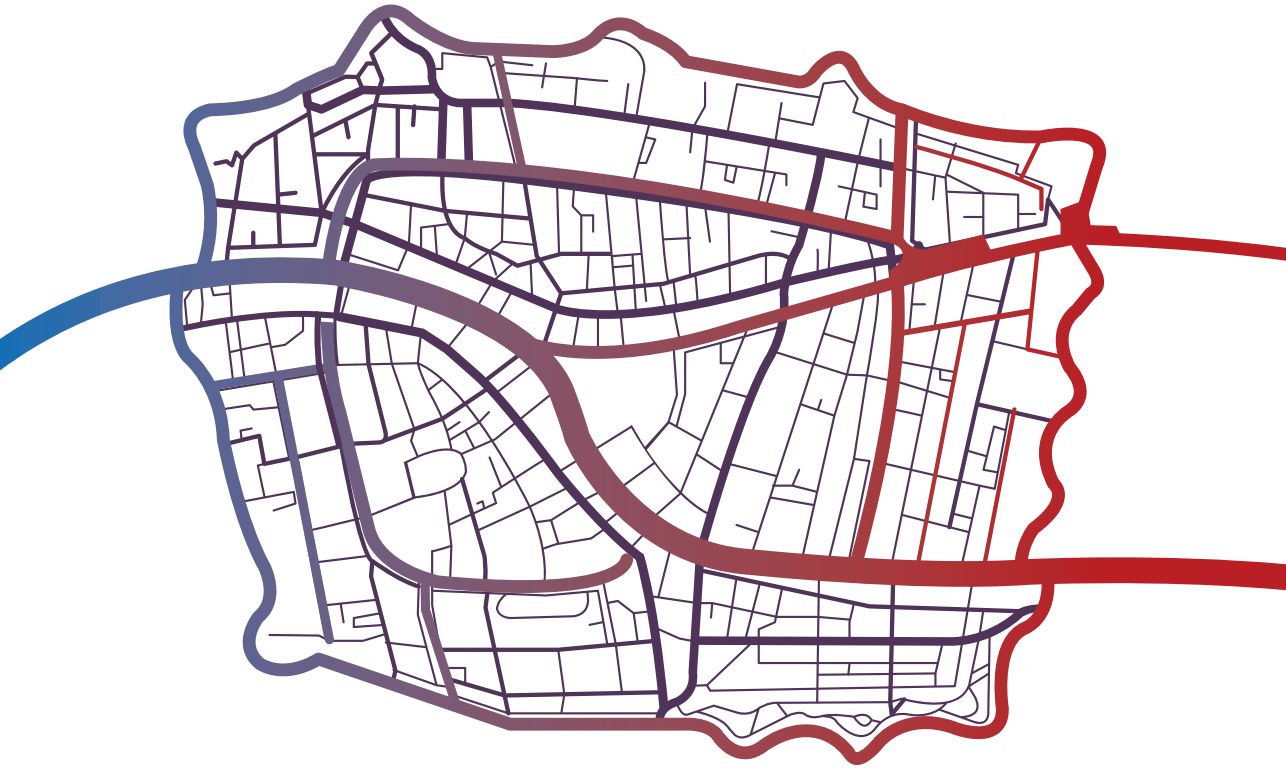


The handle http://hdl.handle.net/1887/66665 holds various files of this Leiden University dissertation.

Author: Suzuki, Y.
Title: From the macro- to the microvasculature : temporal and spatial visualization using arterial spin labeling
Issue Date: 2018-11-01

From the Macro- to the Microvasculature:

Temporal and Spatial Visualization using Arterial Spin Labeling



Yuriko Suzuki

From the Macro- to the Microvasculature:

Temporal and Spatial Visualization using Arterial Spin Labeling

Yuriko Suzuki

Cover designed by proefschrift-aio.nl and Yuriko Suzuki
(Inspired by beautiful canals and streets in Leiden)
Print & layout by proefschrift-aio.nl
ISBN: 978-94-92801-53-1

The research in this thesis was funded by the EU under the Horizon2020 program
(project: CDS-QUAMRI, project number 634541).

© Yuriko Suzuki, 2018
Copyright of the published chapters is held by the publisher of the journal in which the work appeared. All rights reserved. No part of this book may be reproduced or transmitted in any form or by any means without permission of the copyright owner.

From the Macro- to Microvasculature:
Temporal and Spatial Visualization using Arterial Spin Labeling

Proefschrift

Ter verkrijging van
de graad van Doctor aan de Universiteit Leiden,
op gezag van Rector Magnificus prof.mr. C.J.J.M. Stolker,
volgens besluit van het College voor Promoties
te verdedigen op donderdag 1 november 2018
klokke 13:45 uur

door

Yuriko Suzuki

Geboren te Ibaraki, Japan

Promotor:	Prof. dr. A.G. Webb
Co-promotores:	Prof. dr. ir. M.J.P. van Osch
	Dr. T.W. Okell University of Oxford
Promotiecommissie:	Prof. dr. ir. B.P.F. Lelieveldt
	Prof. dr. ir. A.J. Nederveen Academic Medical Center Amsterdam
	Dr. I. Asllani Rochester Institue of Technology
	P.D. Dr. M. Helle Philips GmbH Innovative Technologies

Table of Contents

Chapter 1 09
Introduction and thesis outline

Chapter 2 25
Acceleration of ASL-Based Time-Resolved MR Angiography by Acquisition of Control and Labeled Images in the Same Shot (ACTRESS)
Magn Reson Med 2018;79(1):224-233.

Chapter 3 45
Optimization of the Spatial Modulation Function of Vessel-Encoded Pseudo-Continuous ASL and its Application to Dynamic Angiography
Magn Reson Med 2018;00:1-13. https://doi.org/10.1002/mrm.27418

Chapter 4 73
Acceleration of Vessel-Selective Dynamic MR Angiography by pCASL in Combination with Acquisition of Control and Labeled Images in the Same Shot (ACTRESS)
Magn Reson Med, in revision

Chapter 5 95
Simultaneous Acquisition of Perfusion Image and Dynamic Angiography Using Time-Encoded Pseudo-Continuous ASL
Magn Reson Med 2018;79(5):2676-2684.

Chapter 6 115
A Framework for Motion Correction of Background Suppressed Arterial Spin Labeling Perfusion Images Acquired with Simultaneous Multi-Slice EPI
Magn Reson Med 2018: 1-13. https://doi.org/10.1002/mrm.27499

Chapter 7 141
Summary and general discussion

Nederlandse samenvatting 152
Acknowledgements 154
Curriculum Vitae 156
List of publications

Chapter 1

Introduction and thesis outline

Blood circulation, which delivers oxygen and nutrition by arterial blood, while removing waste products on the venous side, is an essential prerequisite for the survival of biological tissue. Particularly for brain tissue, even a short interruption of the blood circulation can result in critical consequences (1). Because of this great importance, the vascular system has amazing compensatory mechanisms. One of the most important mechanisms is the circle of Willis, which is a circular structure of arteries in the brain allowing collateral blood flow from one hemisphere to the other as well as between the anterior and posterior circulation (2,3). However, when the collateral circulation at the circle of Willis is not sufficient, the pre-existing collateral arterioles start to expand their lumen and eventually result in the development of functional collateral circulation (4-6). This process is induced by increased shear stress following the stenosis/occlusion of a main artery, which is termed arteriogenesis. In contrast, angiogenesis is triggered by tissue hypoxia and results in sprouting of new capillaries. Because these newly generated capillaries do not have vascular smooth muscle cells, they are more fragile.

Detection of such neo-vascularization plays an important role for assessing the severity of several diseases and predicting the patients' outcome. For example, there are abundant reports suggesting that the extent of collateral circulation in patients with ischemic stroke implies not only the prognosis after the onset (7-10), but also the clinical response to the recanalization treatments (11-13). This evidence could encourage the application of the recanalization treatments for a wider time window so that more patients can receive the treatment (14). Another example is Moyamoya disease, which is characterized by progressive steno-occlusion of basal cerebral arteries with a still unknown etiology. Patients with Moyamoya disease generally have a higher potential for arteriogenesis and angiogenesis compared to patients with other types of cerebral ischemia (15), thereby preventing acute progress to

stroke. However, because the progression of the steno-occlusion cannot be stopped by medication, the revascularization surgery is recommended proactively to avoid further ischemic or hemorrhagic events (16,17). Successful restoration of the cerebral blood supply by revascularization can reduce the risks for further events, as well as improving the postoperative activities of daily living (ADL) and long-term prognosis of higher brain functions (16). Therefore, postoperative assessments of revascularization and follow-up are considered very important. Untreated asymptomatic Moyamoya patients (diagnosed before the events) are also considered potentially at risk for future progress and onset of event, thereby requiring careful long-term observation.

On the other hand, angiogenesis is also a hallmark of pathological processes, e.g. to supply tumors with oxygen and nutrient rich blood which is needed to support tumor growth (18,19). Perfusion measurements of tumor blood flow provide important information for condition, staging and differentiation of the disease (20-23). For highly vascularized tumors, such as meningioma, preoperative endovascular embolization is often applied before surgical resection to reduce blood loss during surgery (24). In such cases, information about the feeding arteries (e.g. whether the dominant supply is from internal carotid artery or external carotid artery) is useful for treatment planning. Cerebral arteriovenous malformation (AVM) is also an example of a cerebrovascular disease with increased vascularity, in which abnormal, tangled blood vessels connect arteries directly to veins without the presence of a normal capillary bed in between. Such AVMs provided an increased risk of intracranial hemorrhages. General treatment options of AVMs are surgical resection, gamma knife and endovascular embolization, and the optimal treatment is decided upon by taking the anatomic and hemodynamic properties of the AVM (e.g. size and location of nidus, arterial feeders and pattern of the venous drainage) into account.

In summary, for many cerebrovascular diseases visualization of blood flow through the large vasculature, as well as quantitative information on tissue perfusion, is very important. Arterial spin labeling (ASL) magnetic resonance imaging (MRI) enables the visualization of arterial flow by labeling the magnetization of arterial blood using radiofrequency (RF) pulses. The labeled arterial blood acts as an endogenous tracer, allowing ASL to be used both for MR angiography (MRA) (25-28) and perfusion imaging (29-31) without relying on the use of contrast agents. Although such non-invasive examinations can at the moment not be considered a complete replacement for other more invasive examinations such as X-ray digital subtraction angiography (DSA) and contrast-enhanced (CE) MRI and MRA, many technological innovations have been proposed aiming at providing a non-invasive alternative to those examinations, thereby reducing the burden on patients. For example, pediatric

patients with Moyamoaya disease (the highest peak onset is between 5 to 9 years of age (32)), need numerous diagnostic scans to monitor disease progression and for them establishment of a non-invasive examination without the associated risks of catheter procedures, anesthesia or contrast agent injections would be highly desirable. Moreover, the recently found accumulation of Gadolinium in the brain is another urgent reason to develop non-invasive alternatives.

This doctoral thesis describes the development of several new techniques for dynamic MRA (4D-MRA) and perfusion imaging based upon ASL MRI. The purpose of those developments is to implement clinically useful and feasible techniques, while being as patient-friendly as possible.

Acceleration of ASL-based dynamic angiography (ACTRESS)

In the last decade, 4D-MRA using ASL has become an important alternative to CE-4D-MRA in the brain, by demonstrating advantages over a CE-4D-MRA examination, such as, needless to say, the ability to visualize arteries without using contrast agent, as well as two other main advantages: firstly, in the acquisition of CE-4D-MRA, it is desired to capture the first passage of the contrast agent bolus by means of a real-time dynamic acquisition. Due to very fast passage of the contrast agent through the vascular tree and the early appearance of venous signal, each dynamic must be acquired very quickly, and therefore spatial resolution is usually compromised. In ASL, on the other hand, the labeling of the arterial blood and following data acquisition can be repeated until sufficient information is acquired for both high spatial and temporal resolution, because it is not necessary to acquire all information during a single passage of the bolus.

It should be noted that, however, the scan time of ASL-based 4D-MRA acquisition is generally much longer than CE-4D-MRA. This is not only because of the repeated acquisition to achieve high spatial and temporal resolution, but also because ASL techniques require the acquisition of two types of images: labeled and control images. Subtraction of these two images eliminates the background static tissue signal, thereby isolating the signal of the labeled blood. As Figure 1 illustrates, labeled and control images are usually acquired in separate Look-Locker cycles, resulting in a doubling of the scan time. In previous studies, the mean scan time of ASL-based 4D-MRA was approximately 7 minutes (5 min – 8.5 min) (33-38), which is not always suitable for clinical use.

In chapter 2, the development of a novel ASL-based 4D-MRA technique, named ACTRESS (ACquisition of conTRol and labEled image in the Same Shot) is described. In

the ACTRESS approach, a single control image is acquired before applying the labeling pulse followed by multi-phase Look-Locker readout, and all labeled images are subtracted from this single control image (39). This allows 4D-MRA images to be acquired with similar image quality in nearly half the scan time of the conventional ASL-based 4D-MRA acquisition using pulsed ASL (PASL).

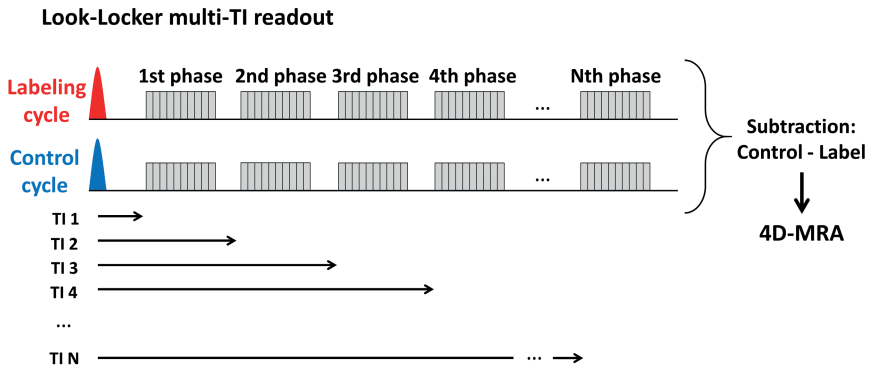


Figure 1: A schematic figure of ASL-based 4D-MRA using Look-Locker readout.

Vessel-selective dynamic angiography using vessel-encoded pseudo-continuous ASL

The second advantage of ASL-based 4D-MRA over CE-4D-MRA is the ability to perform vessel specific visualization, in which the vascular tree arising from a selected artery can be exclusively visualized by means of spatially selective labeling. This technique could provide clinically important information for smoother examination and treatment by X-ray DSA, or even be a potential alternative of X-ray DSA examination for treatment planning and follow-up of many cerebrovascular diseases, such as depiction of collateral flow in patients with steno-occlusive diseases (48) and identification of feeding arteries for AVM (40).

In PASL, a spatially selective inversion slab is applied to the targeted artery, which is generally planned parallel to the artery in the neck (right and left carotid arteries and vertebrobasilar arteries) in the inferior-superior direction (as an angulated coronal or sagittal slab), so that the labeling pulse covers the target artery over a large distance to label a sufficient amount of arterial blood. However, it frequently results in unwanted inclusion of other untargeted arteries, for example because of tortuous vascular anatomy. Also, separation of the internal and external carotid artery (ICA

and ECA) is difficult because the labeling slab usually includes the common carotid artery. In contrast, in pseudo-continuous ASL (pCASL), labeling of arterial blood is performed by means of flow-driven pseudo-adiabatic inversion in a thin labeling plane planned perpendicular to the flow direction. Vessel-selective labeling can be achieved by applying additional gradients in the in-plane direction, generating in-plane differences in labeling efficiency. Therefore, pCASL allows vessel-selective planning with very little restrictions and a low risk of partial labeling of blood in untargeted arteries when tortuous vascular anatomy is present.

In chapter 3, a new implementation of vessel-selective 4D-MRA using vessel-encoded (ve) pCASL (41) is proposed. Ve-pCASL consists of several labeling patterns played out according to a Hadamard matrix, instead of pair-wise acquisition of labeled and control images. For successful implementation, there are two hurdles to overcome. First, the scan time of 4D-MRA using ve-pCASL will increase proportionally to the number of Hadamard-encodings. For perfusion imaging, the acquisition of different vessel-encodings can be performed instead of signal averaging, therefore vessel-selective imaging can be achieved without extra scan time or loss in signal to noise ratio (SNR). However, this is not true for an MRA acquisition, because in ASL-based MRA the entire scan time is usually spent to obtain high spatial resolution, rather than signal averaging. In this study, therefore, separate visualization of three arterial trees arising from the right ICA (RICA), left ICA (LICA) and both vertebral arteries (VAs) is proposed by using four Hadamard-encodings, to minimize the scan time. The measured signal in this study can be written as follows:

$$\boldsymbol{y} = \begin{pmatrix} -1 & 1 & 1 & 1 \\ 1 & -1 & 1 & 1 \\ 1 & 1 & -1 & 1 \\ -1 & -1 & -1 & 1 \end{pmatrix} \begin{pmatrix} RICA \\ LICA \\ VAs \\ S \end{pmatrix} \quad [1]$$

where **y** is the measured signal and *S* is static tissue. Each arterial tree arising from RICA, LICA and VAs is calculated by applying the pseudo-inverse matrix of equation [1].

To achieve visualization of three arterial trees by four Hadamard-encodings as expressed by equation [1], it is essential to have (i) a sharp spatial transition between the labeling and control conditions to accurately separate the target artery (-1 in eq [1]) and other untargeted arteries (1 in eq [1]), and (ii) a broad and flat control condition to provide the same control condition to two, separated arteries. In conventional ve-pCASL, however, the spatial transition between the labeling and control conditions is rather gradual, following a sinusoidal-like pattern, and the control condition is not

broad and flat enough, thereby increasing the risk of partial labeling of non-targeted arteries, which will compromise the accurate separation of the arterial trees in the selective angiograms. In this chapter the shape of the spatial inversion modulation is optimized by changing the pCASL labeling parameters (maximum and mean labeling gradient strength), so that a sharper transition between the labeling and control conditions and broader, flatter control regions can be achieved. This enables the acquisition of ve-pCASL 4D-MRA in half the time of previous implementations (42).

Acceleration of vessel-selective dynamic angiography using the ACTRESS approach

When considering the separate visualization of the ICA and the ECA, applying ve-pCASL with four Hadamard encodings will be difficult due to the number of arteries that need to be differentiated and their location with respect to each other. Instead of ve-pCASL scan, therefore, a simple one-by-one labeling of ICA and ECA might be easier to obtain the desired information. However, a pair-wise acquisition of labeled and control images for each target artery will be time-consuming.

In chapter 4, an extension of the ACTRESS approach is proposed to achieve vessel-selective 4D-MRA. As will be described in chapter 2, the most crucial factor to obtain similar image quality by 4D-MRA using ACTRESS as compared to conventional ASL-based 4D-MRA, is to keep the signal intensity of the static tissue as constant as possible over all readouts of different delay times. When the static tissue signal is stable over all readouts, the signal from static tissue can be successfully eliminated by subtraction. Fluctuations in static tissue signal would cause elevated background signal after subtraction, which would corrupt the visualization of smaller peripheral arteries. To achieve a constant static tissue signal, there are two essential elements that should be considered for the design of the sequence: (i) to keep the readout interval constant to allow the establishment of a steady-state, and (ii) to minimize the effect of the labeling pulse on the magnetization of the imaging volume. As described above, vessel-selective labeling using PASL is generally applied parallel to the target artery in the inferior-superior direction, which will be perpendicular to the imaging slices. The intersection of the labeling slab with the imaging volume will directly violate the above-mentioned second design element of the ACTRESS sequence. For pCASL in which the labeling with spatially-varying labeling efficiency can be achieved within a thin labeling plane perpendicular to the flow direction, vessel-selective labeling can be achieved without affecting the magnetization of the imaging volume. However, the long pCASL labeling train would violate the ACTRESS sequence design element-(i), thereby destroying the steady-state condition and introducing large signal changes of the static tissue during the Look-Locker readout.

Moreover, there is another inconvenience caused by the long pCASL labeling train. Unlike the PASL technique that relies on a very short labeling pulse (approximately 10-20 ms), the pCASL labeling train lasts from hundreds to thousands of milliseconds, after which the front of the bolus of labeled blood will already have reached the peripheral arteries. Therefore, the conventional subtraction would only depict the outflow of labeled blood.

In this study, a WET pre-saturation module (43) was inserted before the pCASL labeling train to minimize the signal variation of the static tissue over the Look-Locker acquisitions. Moreover, a new subtraction scheme was introduced to depict arteries with wide range of temporal information from the early inflow to the late peripheral phase.

Simultaneous acquisition of 4D-MRA and perfusion images using time-encoded pCASL

For assessment of the hemodynamic condition of brain tissue, it is essential not only to visualize large vessel pathology, such as stenosis or collateral flow, but also to know the microvascular status of downstream tissue, i.e. quantitative information on the cerebral perfusion of the tissue. However, including both acquisitions of 4D-MRA and perfusion imaging into a clinical protocol would be hampered by long scan time. To address this issue, in chapter 5, the development of a simultaneous acquisition scheme of 4D-MRA and perfusion imaging is described.

From the technical point-of-view, the main differences between 4D-MRA and perfusion imaging are the spatial resolution of the readout module and the optimal timing of the readout module after the ASL preparation. In 4D-MRA, the readout is started quickly after the labeling and repeated several times using a Look-Locker readout to dynamically visualize the inflow of labeled blood into the arterial tree. To depict even the smallest arteries, a high-resolution 3D readout is employed. In perfusion imaging, on the other hand, a low-resolution readout module needs to be used to detect the subtle signal change arising from the tissue perfusion. Before starting the readout, a long enough delay needs to be inserted so that all (or at least most of the) labeled blood has arrived in the brain tissue and no signal arises from arteries. These differences between 4D-MRA and perfusion sequences suggest something very important: during the delay time of perfusion imaging, readout modules for 4D-MRA can be inserted, which implies that a single labeling module can be shared. However, when a multi-delay Look-Locker readout for 4D-MRA is inserted before the readout for perfusion imaging, the longitudinal magnetization would be consumed too much, i.e. there would be too little label left to obtain perfusion images with sufficient SNR.

In chapter 5, we propose the use of time-encoded pCASL (te-pCASL) to obtain the different temporal information for the 4D-MRA and perfusion image (44). Unlike the Look-Locker readout that was used in previous chapters, in te-pCASL images with N delays are obtained by dividing the long pCASL labeling train into N segments (a.k.a. subboli) with either a label or a control condition. The acquisitions are repeated N+1 times, with different combinations of label/control condition according to a Hadamard matrix of order N+1 (N=7 in Figure 2). By employing the appropriate decoding step, only the ASL signal from a single subbolus can be reconstructed, i.e. N ASL images with different post-labeling delays (PLDs) are obtained. In this study, the first subbolus was optimized for perfusion imaging with a long labeling duration and a PLD of 1.8 sec, whereas the other subboli were optimized for 4D-MRA with relatively short labeling durations to achieve a high temporal resolution as desired in 4D-MRA.

Subbolus 1	2	3	4	5	6	7	Readout module
Label (L)	L	L	L	L	L	L	Image A1
Control (C)	L	C	L	C	L	C	Image A2
Label (L)	C	C	L	L	C	C	Image A3
Control (C)	C	L	L	C	C	L	Image A4
Label (L)	L	L	C	C	C	C	Image A5
Control (C)	L	C	C	L	C	L	Image A6
Label (L)	C	C	C	C	L	L	Image A7
Control (C)	C	L	C	L	L	C	Image A8

Figure 2: A schematic figure of time-encoded (te) pCASL.

ASL perfusion imaging with simultaneous multi-slice EPI acquisition

Compared to 4D-MRA the ASL perfusion signal, i.e. the difference in magnetization between labeled and control images arising from the inflow of labeled arterial blood into the capillary bed and tissue, is much smaller. It is also much smaller than the signal from the brain static tissue (typically less than 1% of the gray matter signal (45)). Therefore, signal fluctuations from static tissue as a result of e.g. motion can be a large disturbance (noise) to the perfusion signal. Because the noise level is proportional to the signal intensity of the static tissue, decreasing the static tissue signal results in a higher SNR of the perfusion images, which can be achieved by applying background suppression (BGS) pulses (45).

There is another factor why ASL signal in perfusion imaging is much lower compared to 4D-MRA: during the delay time that allows all labeled arterial blood to arrive in the brain tissue, the ASL signal will decrease with the T_1 relaxation of the blood. In general, a PLD of 1.8 to 2 seconds is recommended for adult examinations, because too short PLD would not only cause an underestimation of the perfusion signal, since not all labeled arterial blood has arrived yet, but also cause hyperintense vascular artefacts from arteries where labeled blood is still present.

Compared to a 3D readout, unfortunately, multi-slice 2D acquisitions will face even lower SNR, since optimization of BGS-timing is usually performed for the first slice. In distal slices that are typically acquired hundreds of milliseconds later than the first slice, the effectiveness of BGS will be reduced due to longitudinal relaxation. Similarly, the effective PLD of the distal slices will be hundreds of milliseconds longer than the PLD of the first slice, leading again to a loss of SNR in more distal slices.

To address these issues, the application of simultaneous multi-slice (SMS) EPI acquisition to ASL imaging was recently proposed (46,47). The combination of SMS and BGS in ASL perfusion imaging, however, could also potentially introduce new problems when motion correction is required. In chapter 6, these new problems caused by the combined use of SMS and BGS are described, and a new framework to address these problems is proposed. By means of a functional ASL study the effectiveness of the proposed framework is proven.

References

1. Saver JL. Time is brain--quantified. Stroke 2006;37(1):263-266.
2. Liebeskind DS. Collateral circulation. Stroke 2003;34(9):2279-2284.
3. Hartkamp MJ, van Der Grond J, van Everdingen KJ, Hillen B, Mali WP. Circle of Willis collateral flow investigated by magnetic resonance angiography. Stroke 1999;30(12):2671-2678.
4. Heil M, Eitenmuller I, Schmitz-Rixen T, Schaper W. Arteriogenesis versus angiogenesis: similarities and differences. J Cell Mol Med 2006;10(1):45-55.
5. Liu J, Wang Y, Akamatsu Y, Lee CC, Stetler RA, Lawton MT, Yang GY. Vascular remodeling after ischemic stroke: mechanisms and therapeutic potentials. Prog Neurobiol 2014;115:138-156.
6. Buschmann I, Schaper W. The pathophysiology of the collateral circulation (arteriogenesis). J Pathol 2000;190(3):338-342.
7. Henderson RD, Eliasziw M, Fox AJ, Rothwell PM, Barnett HJ. Angiographically defined collateral circulation and risk of stroke in patients with severe carotid artery stenosis. North American Symptomatic Carotid Endarterectomy Trial (NASCET) Group. Stroke 2000;31(1):128-132.
8. Maas MB, Lev MH, Ay H, Singhal AB, Greer DM, Smith WS, Harris GJ, Halpern E, Kemmling A, Koroshetz WJ, Furie KL. Collateral vessels on CT angiography predict outcome in acute ischemic stroke. Stroke 2009;40(9):3001-3005.
9. Lima FO, Furie KL, Silva GS, Lev MH, Camargo EC, Singhal AB, Harris GJ, Halpern EF, Koroshetz WJ, Smith WS, Yoo AJ, Nogueira RG. The pattern of leptomeningeal collaterals on CT angiography is a strong predictor of long-term functional outcome in stroke patients with large vessel intracranial occlusion. Stroke 2010;41(10):2316-2322.
10. Liebeskind DS, Cotsonis GA, Saver JL, Lynn MJ, Turan TN, Cloft HJ, Chimowitz MI, Warfarin-Aspirin Symptomatic Intracranial Disease I. Collaterals dramatically alter stroke risk in intracranial atherosclerosis. Ann Neurol 2011;69(6):963-974.
11. Kucinski T, Koch C, Eckert B, Becker V, Kromer H, Heesen C, Grzyska U, Freitag HJ, Rother J, Zeumer H. Collateral circulation is an independent radiological predictor of outcome after thrombolysis in acute ischaemic stroke. Neuroradiology 2003;45(1):11-18.
12. Bang OY, Saver JL, Kim SJ, Ha Y, Kim GM, Chung CS, Ovbiagele B, Lee KH, Liebeskind DS. Collateral Flow Predicts Response To Endovascular Therapy For Acute Ischemic Stroke. Stroke 2011;42(3):E95-E95.
13. Bang OY, Saver JL, Kim SJ, Kim GM, Chung CS, Ovbiagele B, Lee KH, Liebeskind DS, Collaborators U-SS. Collateral Flow Averts Hemorrhagic Transformation After Endovascular Therapy for Acute Ischemic Stroke. Stroke 2011;42(8):2235-U2329.
14. Ribo M, Flores A, Rubiera M, Pagola J, Sargento-Freitas J, Rodriguez-Luna D, Coscojuela P, Maisterra O, Pineiro S, Romero FJ, Alvarez-Sabin J, Molina CA. Extending the time window for endovascular procedures according to collateral pial circulation. Stroke 2011;42(12):3465-3469.
15. Rafat N, Beck G, Pena-Tapia PG, Schmiedek P, Vajkoczy P. Increased levels of circulating endothelial progenitor cells in patients with Moyamoya disease. Stroke 2009;40(2):432-438.
16. Research Committee on the P, Treatment of Spontaneous Occlusion of the Circle of W, Health Labour Sciences Research Grant for Research on Measures for Infractable D. Guidelines for diagnosis and treatment of moyamoya disease (spontaneous occlusion of the circle of Willis). Neurol Med Chir (Tokyo) 2012;52(5):245-266.
17. Acker G, Fekonja L, Vajkoczy P. Surgical Management of Moyamoya Disease. Stroke 2018;49(2):476-482.
18. Folkman J. Tumor angiogenesis: therapeutic implications. N Engl J Med 1971;285(21):1182-1186.
19. Nishida N, Yano H, Nishida T, Kamura T, Kojiro M. Angiogenesis in cancer. Vasc Health Risk Manag 2006;2(3):213-219.

20. Fujima N, Kudo K, Yoshida D, Homma A, Sakashita T, Tsukahara A, Khin Khin T, Yuri Z, Satoshi T, Hiroki S. Arterial spin labeling to determine tumor viability in head and neck cancer before and after treatment. J Magn Reson Imaging 2014;40(4):920-928.
21. Kikuchi K, Hiwatashi A, Togao O, Yamashita K, Kamei R, Yoshimoto K, Iihara K, Suzuki SO, Iwaki T, Suzuki Y, Honda H. Arterial spin-labeling is useful for the diagnosis of residual or recurrent meningiomas. Eur Radiol 2018.
22. Kikuchi K, Hiwatashi A, Togao O, Yamashita K, Yoshimoto K, Mizoguchi M, Suzuki SO, Iwaki T, Suzuki Y, Honda H. Correlation between arterial spin-labeling perfusion and histopathological vascular density of pediatric intracranial tumors. J Neurooncol 2017;135(3):561-569.
23. Yamashita K, Yoshiura T, Hiwatashi A, Togao O, Yoshimoto K, Suzuki SO, Kikuchi K, Mizoguchi M, Iwaki T, Honda H. Arterial spin labeling of hemangioblastoma: differentiation from metastatic brain tumors based on quantitative blood flow measurement. Neuroradiology 2012;54(8):809-813.
24. Raper DM, Starke RM, Henderson F, Jr., Ding D, Simon S, Evans AJ, Jane JA, Sr., Liu KC. Preoperative embolization of intracranial meningiomas: efficacy, technical considerations, and complications. AJNR Am J Neuroradiol 2014;35(9):1798-1804.
25. Dixon WT, Du LN, Faul DD, Gado M, Rossnick S. Projection angiograms of blood labeled by adiabatic fast passage. Magn Reson Med 1986;3(3):454-462.
26. Nishimura DG, Macovski A, Pauly JM, Conolly SM. MR angiography by selective inversion recovery. Magn Reson Med 1987;4(2):193-202.
27. Nishimura DG, Macovski A, Jackson JI, Hu RS, Stevick CA, Axel L. Magnetic resonance angiography by selective inversion recovery using a compact gradient echo sequence. Magn Reson Med 1988;8(1):96-103.
28. Edelman RR, Siewert B, Adamis M, Gaa J, Laub G, Wielopolski P. Signal targeting with alternating radiofrequency (STAR) sequences: application to MR angiography. Magn Reson Med 1994;31(2):233-238.
29. Edelman RR, Siewert B, Darby DG, Thangaraj V, Nobre AC, Mesulam MM, Warach S. Qualitative mapping of cerebral blood flow and functional localization with echo-planar MR imaging and signal targeting with alternating radio frequency. Radiology 1994;192(2):513-520.
30. Williams DS, Detre JA, Leigh JS, Koretsky AP. Magnetic resonance imaging of perfusion using spin inversion of arterial water. Proc Natl Acad Sci U S A 1992;89(1):212-216.
31. Detre JA, Leigh JS, Williams DS, Koretsky AP. Perfusion imaging. Magn Reson Med 1992;23(1):37-45.
32. Hoshino H, Izawa Y, Suzuki N, Research Committee on Moyamoya D. Epidemiological features of moyamoya disease in Japan. Neurol Med Chir (Tokyo) 2012;52(5):295-298.
33. Yan L, Wang S, Zhuo Y, Wolf RL, Stiefel MF, An J, Ye Y, Zhang Q, Melhem ER, Wang DJ. Unenhanced dynamic MR angiography: high spatial and temporal resolution by using true FISP-based spin tagging with alternating radiofrequency. Radiology 2010;256(1):270-279.
34. Yan L, Salamon N, Wang DJ. Time-resolved noncontrast enhanced 4-D dynamic magnetic resonance angiography using multibolus TrueFISP-based spin tagging with alternating radiofrequency (TrueSTAR). Magn Reson Med 2014;71(2):551-560.
35. Iryo Y, Hirai T, Kai Y, Nakamura M, Shigematsu Y, Kitajima M, Azuma M, Komi M, Morita K, Yamashita Y. Intracranial dural arteriovenous fistulas: evaluation with 3-T four-dimensional MR angiography using arterial spin labeling. Radiology 2014;271(1):193-199.
36. Iryo Y, Hirai T, Nakamura M, Inoue Y, Watanabe M, Ando Y, Azuma M, Nishimura S, Shigematsu Y, Kitajima M, Yamashita Y. Collateral circulation via the circle of Willis in patients with carotid artery steno-occlusive disease: evaluation on 3-T 4D MRA using arterial spin labelling. Clin Radiol 2015;70(9):960-965.
37. Uchino H, Ito M, Fujima N, Kazumata K, Yamazaki K, Nakayama N, Kuroda S, Houkin K. A novel application of four-dimensional magnetic resonance angiography using an arterial spin labeling technique for noninvasive diagnosis of Moyamoya disease. Clin Neurol Neurosurg 2015;137:105-111.

38. Yu S, Yan L, Yao Y, Wang S, Yang M, Wang B, Zhuo Y, Ai L, Miao X, Zhao J, Wang DJ. Noncontrast dynamic MRA in intracranial arteriovenous malformation (AVM), comparison with time of flight (TOF) and digital subtraction angiography (DSA). Magn Reson Imaging 2012;30(6):869-877.
39. Suzuki Y, Fujima N, Ogino T, Meakin JA, Suwa A, Sugimori H, Van Cauteren M, van Osch MJP. Acceleration of ASL-based time-resolved MR angiography by acquisition of control and labeled images in the same shot (ACTRESS). Magn Reson Med 2018;79(1):224-233.
40. Fujima N, Osanai T, Shimizu Y, Yoshida A, Harada T, Nakayama N, Kudo K, Houkin K, Shirato H. Utility of noncontrast-enhanced time-resolved four-dimensional MR angiography with a vessel-selective technique for intracranial arteriovenous malformations. J Magn Reson Imaging 2016;44(4):834-845.
41. Wong EC. Vessel-encoded arterial spin-labeling using pseudocontinuous tagging. Magnetic Resonance in Medicine 2007;58(6):1086-1091.
42. Okell TW, Schmitt P, Bi X, Chappell MA, Tijssen RH, Sheerin F, Miller KL, Jezzard P. Optimization of 4D vessel-selective arterial spin labeling angiography using balanced steady-state free precession and vessel-encoding. NMR Biomed 2016;29(6):776-786.
43. Ogg RJ, Kingsley PB, Taylor JS. WET, a T1- and B1-insensitive water-suppression method for in vivo localized 1H NMR spectroscopy. J Magn Reson B 1994;104(1):1-10.
44. Wells JA, Lythgoe MF, Gadian DG, Ordidge RJ, Thomas DL. In vivo Hadamard encoded continuous arterial spin labeling (H-CASL). Magn Reson Med 2010;63(4):1111-1118.
45. Alsop DC, Detre JA, Golay X, Gunther M, Hendrikse J, Hernandez-Garcia L, Lu H, MacIntosh BJ, Parkes LM, Smits M, van Osch MJ, Wang DJ, Wong EC, Zaharchuk G. Recommended implementation of arterial spin-labeled perfusion MRI for clinical applications: A consensus of the ISMRM perfusion study group and the European consortium for ASL in dementia. Magn Reson Med 2015;73(1):102-116.
46. Feinberg DA, Beckett A, Chen L. Arterial spin labeling with simultaneous multi-slice echo planar imaging. Magn Reson Med 2013;70(6):1500-1506.
47. Zhang K, Yun SD, Shah NJ. Tripled Readout Slices in Multi Time-Point pCASL Using Multiband Look-Locker EPI. PLoS One 2015;10(11):e0141108.
48. Okell TW. Assessment of Collateral Blood Flow in the Brain using Magnetic Resonance Imaging: A thesis submitted for the degree of Doctor of Philosophy. University of Oxford, 2011

Chapter 2

Acceleration of ASL-Based Time-Resolved MR Angiography by Acquisition of Control and Labeled Images in the Same Shot (ACTRESS)

Magn Reson Med 2018; 79 (1): 224-233

Yuriko Suzuki
Noriyuki Fujima
Tetsuo Ogino
James Alastair Meakin
Akira Suwa
Hiroyuki Sugimori
Marc Van Cauteren
Matthias J. P. van Osch

Abstract

Purpose: Non-contrast 4D-MR-angiography (MRA) using arterial spin labeling (ASL) is beneficial because high spatial and temporal resolution can be achieved. However, ASL requires acquisition of labeled and control images for each phase. The purpose of this study is to present a new accelerated 4D-MRA approach that requires only a single control acquisition, achieving similar image quality in approximately half the scan time.

Methods: In a multi-phase Look-Locker sequence, the first phase was used as the control image and the labeling pulse was applied before the second phase. By acquiring the control and labeled images within a single Look-Locker cycle, 4D-MRA was generated in nearly half the scan time of conventional ASL. However, this approach potentially could be more sensitive to off-resonance and magnetization transfer (MT) effects. To counter this, careful optimizations of the labeling pulse were performed by Bloch simulations. In in vivo studies arterial visualization was compared between the new and conventional ASL approaches.

Results: Optimization of the labeling pulse successfully minimized off-resonance effects. Qualitative assessment showed that residual MT effects did not degrade visualization of the peripheral arteries.

Conclusion: This study demonstrated that the proposed approach achieved similar image quality as conventional ASL-MRA approaches in just over half the scan time.

Introduction

Evaluation of cerebrovascular hemodynamics provides crucial information for accurate diagnosis, treatment selection and follow-up of diseases such as arteriovenous malformation, arteriovenous fistula and steno-occlusive disease. Recently, there has been an increasing number of clinical reports using arterial spin labeling (ASL) for non-contrast enhanced (non-CE) magnetic resonance angiography (MRA) (1-6), mainly due to the possibility of time-resolved (4D) MRA as well as vessel-specificity by restricting the labeling to a single vessel (7,8).

4D-MRA can be achieved by acquiring images with different inversion time (TIs), for example, by using a Look-Locker readout (9). The benefit of 4D-MRA using ASL is that injection of the contrast agent is not required and that both high temporal and spatial resolution can be achieved. Unlike CE-MRA, which must capture the quick first passage of the contrast agent and therefore suffers from a compromise between temporal and spatial resolution, labeling of arterial blood can be repeated until sufficient data are acquired to achieve both high temporal and spatial resolution, thus enabling detailed visualization of arterial flow hemodynamics by ASL. To achieve this advantage, ASL-based 4D-MRA usually requires a longer acquisition time than CE-MRA. A second reason for the longer acquisition time of ASL-based 4D-MRA is that ASL techniques require acquisition of two images: one in which the arterial blood is inverted (labeled image) and in the other in which the arterial blood is not inverted (control image). By subtraction of these two images, the background static tissue signal is cancelled out and the inflow of the labeled arterial blood is visualized. The mean acquisition time of previously reported ASL-based 4D-MRA is approximately 7 minutes (5 min – 8.5 min) (1-6), which is not always fast enough to enable its use in clinical protocols.

In this article, we present a novel, ASL-based 4D-MRA technique, named ACTRESS (ACquisition of conTRol and labEled image in the Same Shot), which nearly halves the acquisition time by restricting image acquisition to only the labeled condition. Subtraction can be performed by shifting the labeling pulse to the second phase of the Look-Locker readout and using the first phase as the control image (Figure 1). However, this approach potentially could induce several artefacts because the subtraction is performed between images acquired in different phases of the Look-Locker readout. Moreover, the control image acquired with this approach might not perfectly cancel out the magnetization transfer (MT) effects, unlike conventional ASL sequences designed to keep label and control images as identical as possible with similar level of MT effects.

The purpose of this article is to optimize ACTRESS MRA so that it enables generation of 4D-MRA images of a similar quality to the conventional ASL sequence in nearly half the scan time while avoiding possible artefacts caused by the absence of the separate acquisition of control images. This approach can significantly improve the clinical usability of 4D-MRA due to shorter scan time, which also reduces the occurrence of motion artefacts associated with longer scan duration.

METHODS

Introduction of the ACTRESS Sequence

The principle of ACTRESS-MRA is illustrated in Figure 1. The sequence consists of a 3D multi-shot, multi-phase (multi-TI) Look-Locker readout in combination with a spatially selective labeling pulse, which is applied prior to the readout of the second phase. It is assumed that the image acquired in the first phase does not have a contribution from labeled blood and can therefore be employed as a control image. In the second and later phases, arterial blood that has been inverted by the labeling pulse will flow into the arterial system, thereby reducing the signal from blood. 4D-MRA images can be generated by subtracting all labeled images (2nd – Nth phase) from the single control image, that is, the first phase. By choosing a long-enough cycle duration, all labeled blood has left the arterial system before the next control phase is acquired. The ACTRESS approach acquires all images necessary to generate 4D-MRA in approximately half the scan time of a conventional ASL approach because by employing the first phase as control image it is no longer necessary to acquire a full, separate set of control images.

For this approach to render similar image quality to the conventional ASL approach, the signal from static tissue should be constant over all phases so that the signal from static tissue will cancel upon subtraction between the first phase image and all subsequent phases. To be more specific, the spatially selective labeling pulse played out before the second readout should have no or minimal influence on the imaging volume. However, when a labeling pulse is applied proximal to the imaging volume, the labeling pulse might affect off-resonant magnetization within the imaging region, depending on the bandwidth (BW) of the labeling pulse and applied slab-selection gradient strength during the pulse, which combined will be referred to as *off-resonance effects* in this paper. When keeping the labeling thickness equal, a radiofrequency (RF) pulse with narrower BW will be combined with a smaller selection gradient, thereby leading to a smaller frequency difference between labeling and imaging regions and thus severer off-resonance effects on imaging region. Possible regions

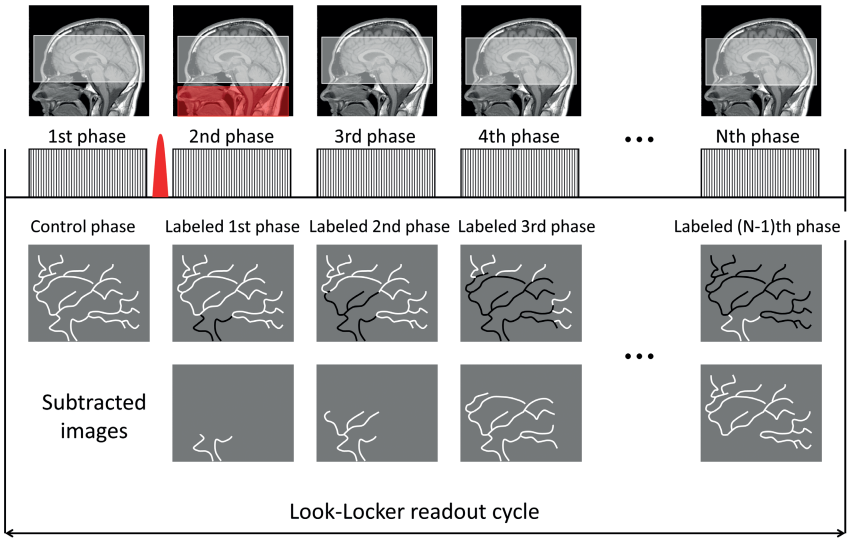


Figure 1: Basic sequence diagram of ACTRESS approach. A spatially selective labeling pulse is applied prior to the second phase readout, whereas the first phase is employed as control image. By subtracting all labeled images from the single control image, 4D-MRA images are generated.

of off-resonance effects include fat and tissue surrounding the paranasal sinuses. Such an influence would result in changes of the static tissue signal after the labeling pulse and recovery in the following phases, leading to subtraction artefacts. In a conventional ASL sequence, such off-resonance effects are avoided by saturating the imaging slices before and after the labeling pulse. For ACTRESS, however, saturation pulses cannot be used because the signal from static tissue should be as constant as possible over all phases to avoid subtraction artefacts. Similarly, on-resonant tissue can show subtraction artefacts when the inversion profile of the labeling pulse is not sharp enough and the tissue magnetization inside the imaging volume is directly affected by the labeling pulse. Finally, MT effects from the labeling pulse could affect the static tissue signal. In conventional ASL, MT effects are eliminated by using a noninverting control pulse with the same RF power for the control condition so that MT effects will be similar between label and control images and therefore subtracted out. For pulsed ASL (PASL) techniques, application of a post-labeling saturation pulse helps to eliminate residual MT effects even further. However, to minimize MT effects in ACTRESS-MRA for which no RF pulse is applied for the control condition and a post-labeling saturation pulse cannot be applied, RF energy for the labeling pulse should be kept as low as possible. Considering all these potential issues, the labeling RF pulse should be optimized to 1) exhibit minimal off-resonance and 2) minimal

MT effects, 3) provide an excellent labeling efficiency and 4) a sharp profile. In this study, we will consider both hyperbolic secant (HS) (10) as well as Frequency offset corrected inversion (FOCI) (11) pulses for performing the labeling.

Optimization of the Labeling RF Pulse

The HS inversion pulse is one of the most commonly used adiabatic labeling pulses for PASL. It enables uniform inversion over a wide range of B_1 amplitudes and can be described by:

$$B_1^{HS}(t) = [A_0 \text{sech}(\beta t)]^{1+i\mu} \quad [1]$$

in which A_0 is the maximum B_1 field, β is the angular frequency which determines the truncation level, and μ is a dimensionless scaling parameter that defines the degree of phase modulation (12,13). The BW of the HS inversion pulse can be calculated to be

$$\Delta f = \mu\beta / \pi \text{ (in Hz)} \quad [2]$$

For convenience of RF pulse implementation, the parameter β_{norm} was introduced (defined as

$$\beta_{norm} = \beta \, RF_{dur} / 2 \quad [3]$$

with RF_{dur} the duration of the RF pulse in seconds).

A disadvantage of the HS pulse is that the BW is rather narrow and therefore is prone to exert large off-resonance effects, which therefore might be less ideal for our single acquisition approach. The FOCI pulse is a modification of the HS inversion pulse (11,14-16), which provides a sharper inversion profile as well as a broader BW by multiplying the RF amplitude, frequency modulation and gradient amplitude with an additional modulation function α(t):

$$A^{FOCI}(t) = \alpha(t) A^{HS}(t)$$

$$\Delta\omega^{FOCI}(t) = \alpha(t) \Delta\omega^{HS}(t)$$

$$G^{FOCI}(t) = \alpha(t) G^{HS}$$

$$\alpha(t) = \begin{cases} \cosh(\beta t) & \text{when } \cosh(\beta t) < \alpha_{max} \\ \alpha_{max} & \text{otherwise} \end{cases} \quad [4]$$

in which G^{HS} is the selection gradient amplitude used for the HS pulse. In this study, an additional Gaussian modulation is applied to the amplitude modulation aiming for further improvement of the slab profile:

$$A^{FOCI}(t) = \alpha(t)\, A^{HS}(t) \exp(-GG2\, t^2) \quad [5]$$

in which GG2 is a parameter that defines the strength of Gaussian modulation.

Bloch equation simulations were performed in MATLAB (Mathworks, Natick, MA, USA) using the maximum B_1 amplitude of 13.47 μT allowed on our clinical 3.0 tesla (T) scanner. The inversion profile, off-resonance effects and labeling efficiency of HS and FOCI pulses were investigated while optimizing the RF pulse parameters: β_{norm}, μ and RF integral (defined as

$$\text{RF integral} = \gamma \int_0^{RF\ dur} A(t)dt \quad [6]$$

corresponding to the RF energy needed to achieve a certain flip angle by a simple nonadiabatic RF pulse) for both the HS and FOCI pulses, and α_{max} and GG2 for the FOCI pulse. The time-varying BW of FOCI pulse $\Delta f^{FOCI}(t)$ was calculated from the time-varying gradient $G^{FOCI}(t)$, the labeling slab thickness Δz and gyromagnetic ratio γ,

$$\Delta f^{FOCI}(t) = \gamma G^{FOCI}(t) \Delta z \quad [7]$$

and its mean value was defined as the effective BW of the FOCI pulse to reduce the resulting off-resonance effects. The default settings on our scanner for β_{norm}, μ and RF integral of the HS labeling pulse for the Signal Targeting with Alternating Radio Frequency (STAR) sequence (17) are 4.0, 5.0 and 850, respectively. These values were used for comparison and will be referred to as *default settings*. In this simulation, the labeling slab thickness was set to 100 mm, and the T_1 and T_2 value of 1450 ms and 85 ms, which were approximate mean value of gray matter and white matter in 3T (18), were used.

In Vivo Healthy Volunteer Study

The study was approved by the local institutional review board, and all volunteers provided written informed consent before inclusion into this study. A total of six volunteers (male = 2, female = 4, mean age = 31 years [range,19-62 years]) without known cerebrovascular disease participated in the study.

Following the results of the Bloch equation simulation (see Results/Discussion section), an in vivo healthy volunteer study was performed using the optimized HS- and FOCI-labeling pulses focusing on finding the optimal inversion thickness of the labeling slab. Also, the images acquired with the ACTRESS sequence were compared to a traditional ASL-based 4D-MRA sequence (STAR), with similar imaging parameters.

The thickness of the labeling slab was set to 80, 100, 120, 160 and 200 mm, whereas the gap between the labeling and imaging volume was fixed at 20 mm. Care was taken to select the appropriate polarity of the volume selection gradient of the labeling pulse to avoid off-resonance effects of the fat within the imaging volume. For the first volunteer, the default settings of the HS labeling pulse were used and compared to the optimized HS and FOCI pulses. However, because severe off-resonance effects were observed with the default HS pulse (see Figure 4), only the optimized HS and FOCI pulses were used for the other five volunteers. For these five volunteers, 4D-MRA using the STAR sequence was added for comparison. Table 1b shows the RF pulse parameters used for the first and other five volunteers.

All MR scans were performed on a Philips 3.0T Ingenia scanner (Philips, Best, The Netherlands) using a 32-channel head coil. Other imaging parameters were as follows: multi-shot multi-phase Look-locker readout with 3D turbo field echo planar imaging (TFEPI) sequence (TFE factor of 13 in feet-head direction and EPI factor of 5 in anterior-posterior direction), field of view = 220 mm, scan matrix = 176 × 176, reconstructed as 256 × 256 by zero-filling, and 70 slices with thickness of 1.3 mm were acquired and reconstructed as 140 slices of 0.65 mm, sensitivity encoding (SENSE) factor = 2.3 in anterior-posterior direction and 1.2 in feet-head direction, echo time/repetition time = 4.9/13.0 ms, and flip angle = 10°. A total of 12 phase images (the first phase acts as the control image, and other 11 are labeled images) were acquired with an interval of 200 ms, resulting in TIs between 49 ms and 2049 ms. The duration of the Look-Locker readout cycle was set to 2.4 seconds. Before starting the actual acquisition of the data, one dummy cycle consisting of 12 Look-Locker phases was performed to reach steady-state. Scan time was 3:40 min. Parameters for 4D-MRA using the STAR sequence were identical to the parameters of ACTRESS, except for the number of phases being set to 11 to acquire the same number of subtracted image as ACTRESS MRA. The scan time of the STAR sequence was 6:50 min.

Image Processing of *In Vivo* Data

First, magnitude subtraction of all labeled images (2nd – Nth phase; N=12) from the control image acquired during the first phase of the sequence was performed. Maximum intensity projection (MIP) images for each temporal phase were generated in sagittal, transverse and coronal directions.

In order to assess MT effects of the tested labeling pulses, the signal intensity of the background brain tissue on the subtracted images was measured through all temporal phases. For each volunteer, MIPs were produced across all temporal phases for each slice (temporal MIP), and two regions of interest (ROIs) were manually drawn on the left and right side of the brain on the 10th, 20th, 30th, 40th and 50th slice, avoiding obvious vessels and artefacts. These ten ROIs were copied to the substracted, non-MIP images and the mean value was calculated as a function of TIs.

To investigate the relation between the labeling slab thickness and the bolus shape of the labeled blood, signal intensity in the M3 segment of both middle cerebral arteries was measured. A MIP image across all phases in the transverse orientation was generated (4D-MIP). On one of them, two ROIs were manually drawn to indicate the M3, and these two ROIs were copied to all other 4D-MIPs. In these ROIs, 20 pixels with the highest signal intensity were chosen, and the mean signal intensity curves over all temporal phases were obtained.

Finally, a qualitative comparison of image quality and visualization of arteries was performed between ACTRESS-MRA and 4D-MRA acquired using the STAR sequence by a board-certified neuroradiologist with 12 years of experience (N.F.). The scoring system was as following:

- Visualization of peripheral arteries, superficial temporal artery (STA) and occipital artery (OA):
  4 = excellent, 3 = good, 2 = moderate, 1 = poor
- Noise from the background tissue and off-resonance artefacts:
  3 = almost no noise/artefacts, 2 = slight degree of noise/artefacts with no influence for diagnosis, 1 = certain degree of noise/artefacts with influence for diagnosis

Results

Optimization of the Labeling RF Pulse

Table 1a shows the simulated values of BW and RF duration produced by changing the RF pulse parameters. When varying β_{norm} while keeping μ and the RF integral fixed at default settings of 5.0 and 850, respectively, a higher β_{norm} prolonged the RF pulse duration in a nearly linear relationship, because the maximum B_1 amplitude was limited by that of the MRI scanner. Due to the concomitant increase in pulse duration, the increase of BW, which would help to reduce the off-resonance effects, was limited. Therefore, similar inversion profiles and off-resonance effects were observed for β_{norm} of 4.0, 6.0 and 8.0 (Figure 2a). For further optimization, β_{norm} was set to 6.0 with a truncation level of 0.5 % of the maximum HS amplitude and RF duration of 15.9 ms (for an RF integral of 850), both which are presumed not to generate degradation of the slice profile. A higher value of μ resulted in an increase of BW. However, the simulated inversion profile showed reduced labeling efficiency with higher μ (Figure 2b), which can be counteracted by increasing the RF integral (Figure 2c). Based on these results, β_{norm} of 6.0, μ of 10.0 and an RF integral of 1000, resulting in RF duration of 18.7 ms, were used as the optimized HS pulse in the in vivo studies.

A higher value of α_{max} resulted in wider effective BW, although larger distortions were observed in the simulated inversion profile (Figure 2d). These distortions were reduced with higher RF integral (Figure 2e). The distortions also could be minimized (Figure 2f) by increasing the level of the GG2. However, too high values in GG2 resulted in asymmetrical distortion when off-resonance effects were included in the simulations (Figure 2g). Based on these observations, several combinations of RF parameters were tested in the preliminary study (data not shown) and the following parameters were determined as the optimized FOCI pulse for further investigation in the in vivo studies: β_{norm} = 6.0, μ = 3.0, α_{max} = 4.0, GG2 = 1.2 and RF integral = 950. Optimized RF parameters and simulated inversion profiles are shown in Table 1b and Figure 3 for comparison with the default settings.

Table 1: RF Parameters Used in the Bloch Equation Simulation (a), and In Vivo study (b).

(a)

	β_{norm}	β (s^{-1})	μ	α_{max}	GG2	RF integral	BW (Hz)	RF duration (ms)
HS	4.0	741.9	5.0			850	1180.8	10.8
	6.0	754.9	5.0			850	1204.7	15.9
	8.0	759.0	5.0			850	1207.9	21.1
	6.0	754.9	7.5			850	1807.1	15.9
	6.0	754.9	10.0			850	2409.5	15.9
	6.0	754.9	12.5			850	3011.8	15.9
	6.0	754.9	15.0			850	3614.2	15.9
	6.0	714.9	10.0			900	2275.6	16.8
	6.0	677.3	10.0			950	2155.8	17.7
	6.0	643.4	10.0			1000	2048.0	18.7
FOCI	6.0	756.9	5.0	1.0	0.0	850	1204.7*	15.9
		1138.2		2.0	0.0	850	3352.2*	10.5
		1337.8		3.0	0.0	850	5519.0*	9.0
		1476.6		4.0	0.0	850	7692.8*	8.1
		1321.2		4.0	0.0	950	6883.0*	9.1
		1195.3		4.0	0.0	1050	6227.5*	10.0
		1091.4		4.0	0.0	1150	5686.0*	11.0
		1004.1		4.0	0.0	1250	5231.1*	12.0
		1330.6		4.0	1.0	850	6932.4*	9.0
		1217.4		4.0	2.0	850	6342.6*	9.9
		1126.4		4.0	3.0	850	5868.5*	10.7

(b)

Default HS**	4.0	741.9	5.0			850	1180.8	10.8
Optimized HS	6.0	643.4	10.0			1000	2048.0	18.7
Optimized Foci	6.0	1168.3	3.0	4.0	1.2	950	3652.1*	10.3

* Effective BW calculated using equation [7]

**Also used for STAR sequence

BW: bandwidth, FOCI: frequency offset corrected inversion, HS: hyperbolic secant, RF: radiofrequency, STAR: signal targeting with alternating radio frequency

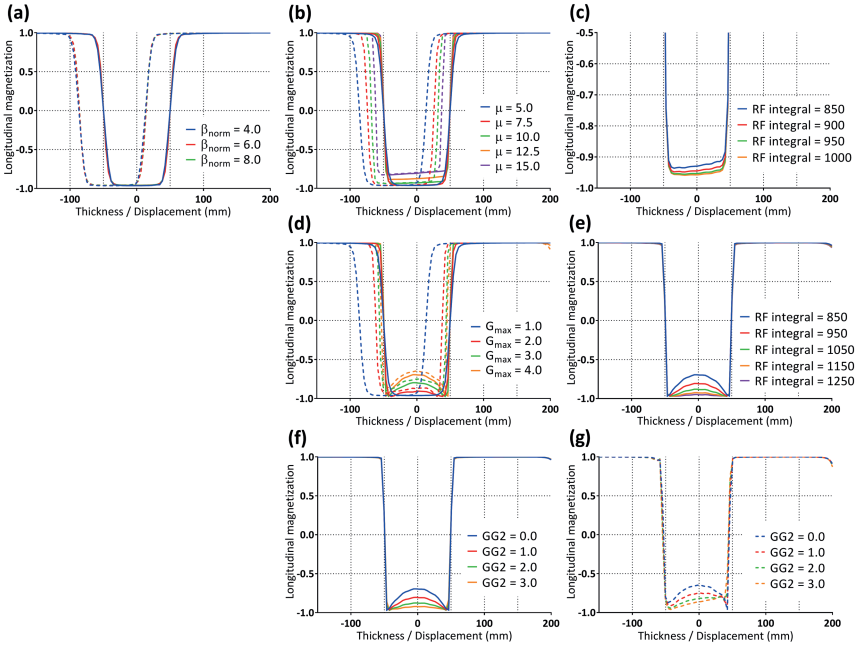


Figure 2: Simulated inversion profile curves. (a) HS pulse, varying β_{norm} with fixed μ and RF integral at default settings of 5.0 and 850, (b) HS pulse with varying μ (β_{norm} = 6.0, RF integral = 850), (c) HS pulse with varying RF integral (β_{norm} = 6.0 μ = 10.0), (d) FOCI pulse with varying α_{max} (β_{norm} = 6.0 μ = 5.0, RF integral = 850, GG2 = 0.0), (e) FOCI pulse with varying RF integral (β_{norm} = 6.0 μ = 5.0, α_{max} = 4.0, GG2 = 0.0), (f) FOCI pulse with varying GG2 (β_{norm} = 6.0 μ = 5.0, RF integral = 850, α_{max} = 4.0) at on-resonance, and (g) off-resonance of 3.4 ppm. For all graphs, solid-line and dashed-line represent on-resonance and off-resonance of 3.4 ppm, respectively.

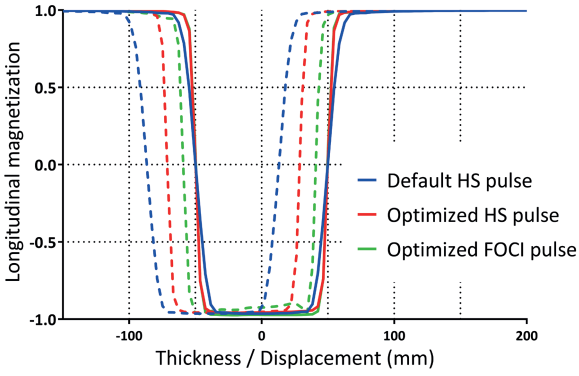


Figure 3: Simulated inversion profile of HS pulse with default settings, optimized HS pulse and optimized FOCI pulse. Solid line and dashed line represent on-resonance and off-resonance of 3.4 ppm, respectively. RF parameters are shown in Table 1b.

In Vivo Studies

Figure 4 shows that severe signal elevation was observed in off-resonant regions, such as tissue surrounding the paranasal sinuses and the petrous part of the temporal bone when the HS labeling pulse with the default settings was used. Similar artefacts were only present for the optimized HS pulses when a labeling slab of 200 mm thickness or thicker were employed. With the optimized FOCI pulses, no off-resonance artefacts were observed in any of the volunteers.

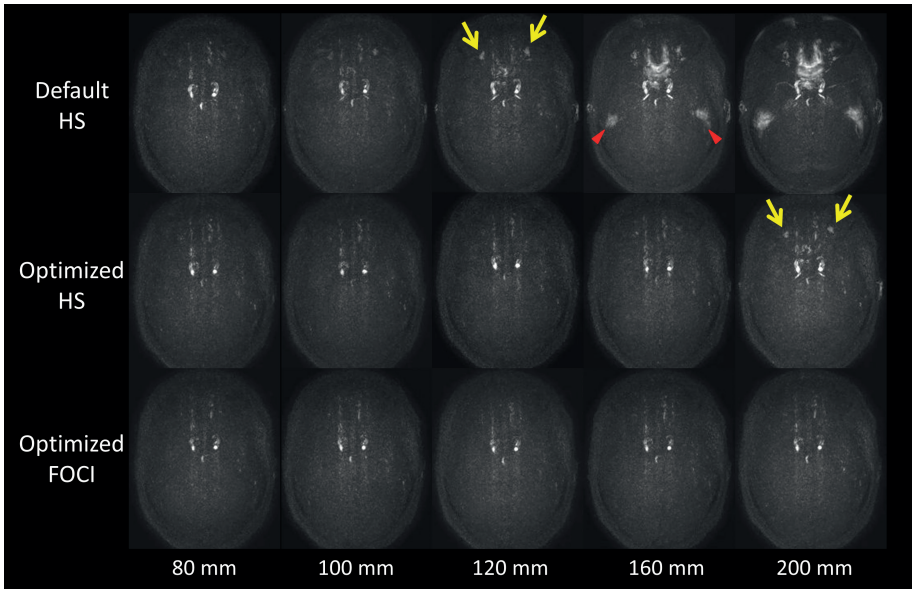


Figure 4: Severe signal elevation was observed at tissue surrounding the paranasal sinuses (yellow arrows) and the petrous part of the temporal bone (red arrow heads) when the HS labeling pulse with the default settings was used. Similar artefacts were only present for the optimized HS pulses when 200 mm thick (or thicker) labeling slabs were employed. With the optimized FOCI pulses, no off-resonance artefacts were observed in any of the volunteers.

Figure 5a shows how the background static tissue signal varied over the readout phases for the different RF pulses, as measured in the first volunteer. Increased static tissue signal intensity was observed in the first few phases, which can be attributed to MT effects by the labeling pulse. These background signal changes were smaller for the optimized HS and FOCI pulses as compared to the HS pulse with the default settings. Figure 5b and c depict the averaged data over all six volunteers showing that weaker MT effects were observed for a thinner labeling slab. This might be attributed to the stronger selection gradient employed for the thinner labeling slabs, which causes larger frequency offsets of the applied RF pulses.

Figure 5d shows the averaged signal intensity time courses, as measured in the M3 segment using the default HS, optimized HS and FOCI pulses. The optimized HS and FOCI pulses generated very similar arterial signal, whereas the default HS pulse showed slightly lower signals during the peak of the bolus curve (Figure 5d). For both optimized pulses (Figure 5e and f), a thinner labeling slab of 80 and 100 mm resulted in lower maximum signal intensity, as well as smaller full-width half-maximum of the bolus curve. However, results from thicker labeling slabs of 160 and 200 mm did not differ significantly from the 120 mm labeling slab thickness, presumably due to the limited range of the body transmit coil.

The results of the qualitative comparison of image quality and visualization of arteries between ACTRESS-MRA and 4D-MRA using the STAR sequence are shown in Table 2, and Figure 6 shows example images from a representative volunteer. These images demonstrate that the ACTRESS approach can provide visualization of the dynamic passage of labeled blood flow through the vascular tree of a similar quality to the standard STAR sequence. This similar performance was corroborated by the observer study, which showed no difference in qualitative scoring measures between ACTRESS and the conventional ASL technique (STAR). Slightly reduced visibility of peripheral arteries was observed for ACTRESS-MRA, with thickness of 80 and 100 mm labeling slab thickness as compared to 120, 160 and 200 mm, as well as the STAR images. Similarly, labeling slab thicker than 120 mm did not have an obvious benefit for visualization of the STA, OA or the peripheral arteries as compared to the labeling slab of 120 mm. In fact, the visibility of OA was slightly weaker for ACTRESS-MRA for a labeling thickness of 160 and 200 mm as compared to 120 mm thickness.

In one of the five volunteers, slight motion was observed in the image acquired with the STAR sequence, resulting in reduced visibility of the peripheral arteries.

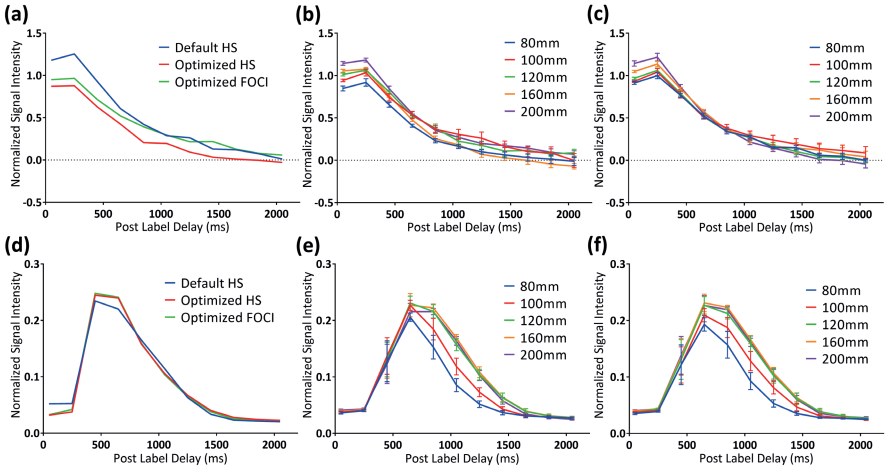


Figure 5: Signal intensity curves over the readout phases acquired from in vivo study. (a) Background static tissue signal acquired with different RF pulses as measured in the first volunteer. (b) Averaged background static tissue signal over all six volunteers acquired with different labeling slab thickness of the optimized HS pulses, and (c) optimized FOCI pulses. (d) Arterial signal measured in the M3 segment using different RF pulses as measured in the first volunteer. (e) Averaged arterial signal over all six volunteers using the optimized HS pulses, and (f) optimized FOCI pulses.

Table 2: The scores of the qualitative comparison of image quality and visualization of arteries between ACTRESS-MRA and conventional 4D-MRA using the STAR sequence.

	Thickness (mm)	Visualization of peripheral arteries	Visualization of STA	Visualization of OA	Noise on the background tissue	Off-resonance artefacts
ACTRESS (Optimized HS)	80	3.2	3.8	3.6	2.8	3.0
	100	3.8	3.8	3.6	2.8	3.0
	120	4.0	3.8	3.6	2.8	3.0
	160	4.0	3.8	3.4	2.8	2.4
	200	4.0	3.8	3.4	2.8	1.6
ACTRESS (Optimized Foci)	80	3.0	3.8	3.6	2.8	3.0
	100	3.6	3.8	3.6	2.8	3.0
	120	4.0	3.8	3.6	2.8	3.0
	160	4.0	3.8	3.4	2.8	3.0
	200	4.0	3.8	3.4	2.8	3.0
STAR	300	3.8	3.8	3.8	2.8	3.0

ACTRESS: acquisition of control and labeled images in the same shot, HS: hyperbolic secant, MRA: MR angiography, OA: occipital artery, STA: superficial temporal artery, STAR: signal targeting with alternating radio frequency.

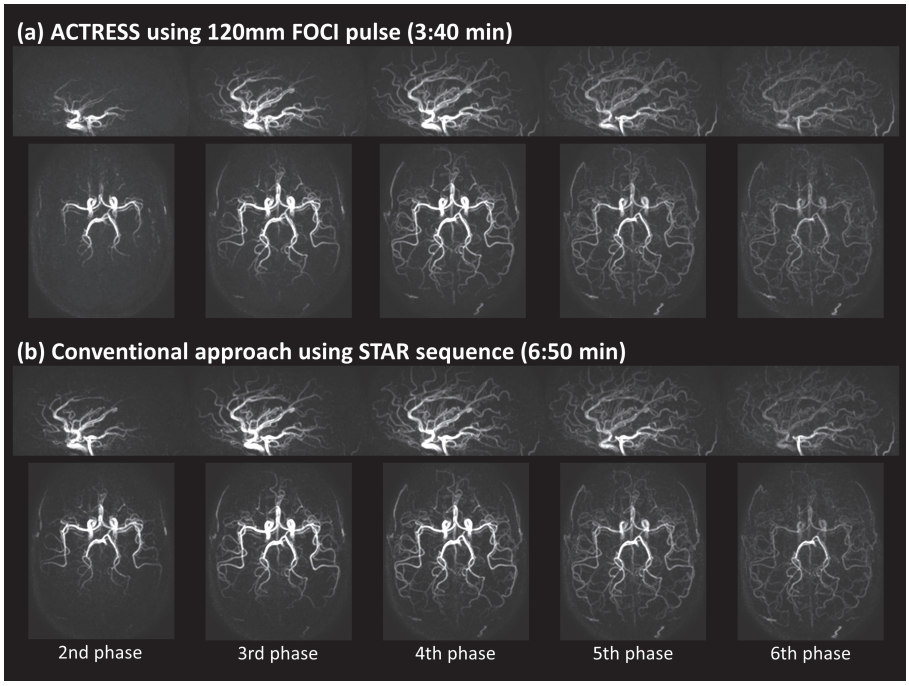


Figure 6: Example images of ACTRESS-MRA and conventional 4D-MRA using the STAR sequence.

Discussion

In this study, we have presented a new ASL-based 4D-MRA technique, ACTRESS, which nearly halves the acquisition time of the conventional sequence by acquiring the labeled and control images in a single Look-Locker readout cycle. This brought down the typical acquisition time of a 4D-MRA sequence from approximately 7 to 3.5 minutes, which in clinical practice could be the difference between inclusion or exclusion of a 4D-MRA sequence in an examination protocol. We optimized the labeling RF pulse to minimize potential artefacts, and our observer study demonstrated that the ACTRESS-MRA achieved a very similar image quality to the standard ASL 4D-MRA.

To provide a comparable image quality to the standard ASL 4D-MRA, careful optimization of the labeling pulse was required. As compared to the HS pulse, the FOCI pulse with use of the Gaussian modulation allowed more flexible optimization. Because of the relatively low, maximally allowed B_1 amplitude of 13.5 µT of our clinical 3.0T scanner when using the body coil for RF pulse transmission, FOCI pulses with higher value of α_{max} showed a distorted inversion profile in the simulation results. Such distortions could be minimized by use of higher maximum B_1 amplitude, which is not

allowed by the employed scanner, or by increasing the RF integral. However, these improvements would be achieved at the expense of increased MT effects. By applying the Gaussian modulation, the distortion of the inversion profile was reduced without a concomitant increase of MT effects, although very strong Gaussian modulation induced asymmetrical distortions at off-resonance. Considering these observations and the fact that our ACTRESS approach is sensitive to MT effects, combination of the increase of RF integral and moderate Gaussian modulation was found to be optimal for the ACTRESS approach. Potentially, other adiabatic pulses such as BASSI-pulses (Bandwidth-modulated Adiabatic RF pulses for uniform Selective Saturation and Inversion) (19) could achieve similar or even slightly better results, which could be tested for future implementations.

After the optimization of the labeling pulse, our in vivo study showed that the artefacts due to the off-resonance effects were minimized by increasing the BW of the HS labeling pulse, and completely annulled by use of the FOCI pulse. Furthermore, it was found that the optimization of the labeling pulse was accompanied by a reduction of MT effects in the static tissue. For both optimized HS and FOCI pulses, a wider range of frequency sweeps was applied to achieve a wider BW as compared to the default settings, and we can deduce that the MT effects within the imaging volume were reduced due to these larger frequency offsets. Control for MT effects is especially essential for perfusion imaging such that the signal intensity of the subtracted image reflects only the inflow of labeled arterial blood, hereby enabling accurate estimation of the cerebral blood flow (CBF). However, the prime goal of 4D-MRA is visualization of blood flow within the vasculature, which allows for some background signal to be present as long as it does not obscure visualization of the small vessels. The observer study demonstrated that the remaining MT effects for the optimized HS and FOCI pulses did not degrade the visualization of peripheral arteries in ACTRESS-MRA. However, it should be noted that for now this approach is applicable only for 4D-MRA, whereas for perfusion imaging it will be difficult to use the same approach because it will be more sensitive to MT effects due to the much lower perfusion signal compared to the intensity of background tissue.

In our in vivo study, artefacts due to the off-resonance effects were only observed when using the optimized HS pulse with a slab thickness of 160 and 200 mm. Because the in vivo study indicated that the labeling slab with thickness of 160 and 200 mm did not provide any improvement in visualization, it seems there is no benefit of using a labeling slab thicker than 120 mm. Considering this fact, it can safely be said that the optimized HS pulse removed the off-resonance artefacts as effectively as the optimized FOCI pulse in our study. However, when subjects have relatively larger

paranasal sinuses, it could cause larger off-resonance, and artefacts may appear even with a labeling thickness of 120 mm. To minimize the risk of artefacts, the use of FOCI pulses is recommended to achieve wider BW.

In the ACTRESS approach, it is assumed that the image acquired in the first phase does not have any labeled blood present to enable the use of the first phase image as the control image. However, this assumption could fail if the Look-Locker multi-phase acquisition is terminated before all labeled blood has disappeared from the arterial vessels by flow and/or decay of the labeling due to T_1 relaxation. If labeled blood were still present in the arterial vessels, this will cause reduced signal intensity from those arteries in the control image, because the last phase of the Look-Locker readout is immediately followed by the first phase of the next Look-Locker readout cycle. Therefore, it is important to set the Look-Locker readout cycle duration long enough such that all labeled blood has flowed away or disappeared due to T_1 relaxation. This requires special attention in patients who have slow arterial flow and thus late arrival of label. Due to the cyclic properties of ACTRESS, an alternative way of presenting the technique would be that the last phase of the Look-Locker readout is used as control image with the label pulse played out just before the readout of the first Look-Locker phase. This alternative viewpoint might be helpful to understand the influence of slow flow on the 4D-MRA ACTRESS images.

The idea to minimize the influence of ASL pulses on the contrast of the control image to enable a shorter total acquisition time by minimizing the time spent on measuring control data has been mentioned previously in literature. An example of such an approach is the un-inverted flow-sensitive alternating inversion recovery (UNFAIR) technique (20). In this technique, spins in the imaging region experience 360-degree rotation by two inversion pulses for both the label as well as the control condition. A small residual saturation of these spins will fully recover after a long enough TI; the authors did suggest that any image acquired with the same imaging parameters without labeling pulse could serve as control image in this technique. However, this approach has not seen frequent application in recent literature or clinical protocols.

Conclusion

A novel accelerated time-resolved ASL-MRA technique, ACTRESS, has been introduced. The labeling pulse was optimized to avoid artefacts due to off-resonance effects while also achieving a minor reduction of MT effects. Qualitative assessment demonstrated that ACTRESS-MRA was capable of producing a 4D-MRA image quality similar to conventional ASL 4D-MRA in close to half the scan time. This approach improves the clinical usability for many cerebrovascular diseases.

References

1. Yan L, Wang S, Zhuo Y, Wolf RL, Stiefel MF, An J, Ye Y, Zhang Q, Melhem ER, Wang DJ. Unenhanced dynamic MR angiography: high spatial and temporal resolution by using true FISP-based spin tagging with alternating radiofrequency. Radiology 2010;256(1):270-279.
2. Yan L, Salamon N, Wang DJ. Time-resolved noncontrast enhanced 4-D dynamic magnetic resonance angiography using multibolus TrueFISP-based spin tagging with alternating radiofrequency (TrueSTAR). Magn Reson Med 2014;71(2):551-560.
3. Iryo Y, Hirai T, Kai Y, Nakamura M, Shigematsu Y, Kitajima M, Azuma M, Komi M, Morita K, Yamashita Y. Intracranial dural arteriovenous fistulas: evaluation with 3-T four-dimensional MR angiography using arterial spin labeling. Radiology 2014;271(1):193-199.
4. Iryo Y, Hirai T, Nakamura M, Inoue Y, Watanabe M, Ando Y, Azuma M, Nishimura S, Shigematsu Y, Kitajima M, Yamashita Y. Collateral circulation via the circle of Willis in patients with carotid artery steno-occlusive disease: evaluation on 3-T 4D MRA using arterial spin labelling. Clin Radiol 2015;70(9):960-965.
5. Uchino H, Ito M, Fujima N, Kazumata K, Yamazaki K, Nakayama N, Kuroda S, Houkin K. A novel application of four-dimensional magnetic resonance angiography using an arterial spin labeling technique for noninvasive diagnosis of Moyamoya disease. Clin Neurol Neurosurg 2015;137:105-111.
6. Yu S, Yan L, Yao Y, Wang S, Yang M, Wang B, Zhuo Y, Ai L, Miao X, Zhao J, Wang DJ. Noncontrast dynamic MRA in intracranial arteriovenous malformation (AVM), comparison with time of flight (TOF) and digital subtraction angiography (DSA). Magn Reson Imaging 2012;30(6):869-877.
7. Fujima N, Osanai T, Shimizu Y, Yoshida A, Harada T, Nakayama N, Kudo K, Houkin K, Shirato H. Utility of noncontrast-enhanced time-resolved four-dimensional MR angiography with a vessel-selective technique for intracranial arteriovenous malformations. J Magn Reson Imaging 2016.
8. Jensen-Kondering U, Lindner T, van Osch MJ, Rohr A, Jansen O, Helle M. Superselective pseudo-continuous arterial spin labeling angiography. Eur J Radiol 2015;84(9):1758-1767.
9. Gunther M, Bock M, Schad LR. Arterial spin labeling in combination with a look-locker sampling strategy: inflow turbo-sampling EPI-FAIR (ITS-FAIR). Magn Reson Med 2001;46(5):974-984.
10. Silver MS, Joseph RI, Hoult DI. Selective spin inversion in nuclear magnetic resonance and coherent optics through an exact solution of the Bloch-Riccati equation. Phys Rev A Gen Phys 1985;31(4):2753-2755.
11. Ordidge RJ, Wylezinska M, Hugg JW, Butterworth E, Franconi F. Frequency offset corrected inversion (FOCI) pulses for use in localized spectroscopy. Magn Reson Med 1996;36(4):562-566.
12. Norris DG. Adiabatic radiofrequency pulse forms in biomedical nuclear magnetic resonance. Concept Magnetic Res 2002;14(2):89-101.
13. Bernstein MA, King KF, Zhou XJ. Handbook of MRI Pulse Sequences: Elsevier Science; 2004.
14. Payne GS, Leach MO. Implementation and evaluation of frequency offset corrected inversion (FOCI) pulses on a clinical MR system. Magn Reson Med 1997;38(5):828-833.
15. Yongbi MN, Branch CA, Helpern JA. Perfusion imaging using FOCI RF pulses. Magn Reson Med 1998;40(6):938-943.
16. Yongbi MN, Yang Y, Frank JA, Duyn JH. Multislice perfusion imaging in human brain using the C-FOCI inversion pulse: comparison with hyperbolic secant. Magn Reson Med 1999;42(6):1098-1105.
17. Edelman RR, Siewert B, Darby DG, Thangaraj V, Nobre AC, Mesulam MM, Warach S. Qualitative mapping of cerebral blood flow and functional localization with echo-planar MR imaging and signal targeting with alternating radio frequency. Radiology 1994;192(2):513-520.
18. Stanisz GJ, Odrobina EE, Pun J, Escaravage M, Graham SJ, Bronskill MJ, Henkelman RM. T1, T2 relaxation and magnetization transfer in tissue at 3T. Magn Reson Med 2005;54(3):507-512.

19. Warnking JM, Pike GB. Bandwidth-modulated adiabatic RF pulses for uniform selective saturation and inversion. Magn Reson Med 2004;52(5):1190-1199.
20. Helpern JA, Branch CA, Yongbi MN, Huang NC. Perfusion imaging by un-inverted flow-sensitive alternating inversion recovery (UNFAIR). Magn Reson Imaging 1997;15(2):135-139.

Chapter 3

Optimization of the Spatial Modulation Function of Vessel-Encoded Pseudo-Continuous ASL and its Application to Dynamic Angiography

Magn Reson Med 2018;00:1-13. https://doi.org/10.1002/mrm.27418

Yuriko Suzuki
Matthias J. P. van Osch
Noriyuki Fujima
Thomas W. Okell

Abstract

Purpose: In vessel-encoded pseudo-continuous arterial spin labeling (ve-pCASL), vessel-selective labeling is achieved by modulation of the inversion efficiency across space. However, the spatial transition between the labeling and control conditions is rather gradual, which can cause partial labeling of vessels, reducing SNR-efficiency and necessitating complex post-processing to decode the vessel-selective signals. The purpose of this study is to optimize the pCASL labeling parameters to obtain a sharper spatial inversion profile of the labeling and thereby minimizing the risk of partial labeling of untargeted arteries.

Methods: Bloch simulations were performed to investigate how the inversion profile was influenced by the pCASL labeling parameters: the maximum (G_{max}) and mean (G_{mean}) labeling gradient were varied for ve-pCASL with unipolar and bipolar gradients. The findings in the simulation study were subsequently confirmed in an in vivo volunteer study. Moreover, conventional and optimized settings were compared for 4D-MRA using four-cycle Hadamard ve-pCASL; the visualization of arteries and the presence of the partial labeling were assessed by an expert observer.

Results: When using unipolar gradient, lower G_{mean} resulted in a steeper spatial transition, whereas the width of the control region was broader for higher G_{max}. The in vivo study confirmed these findings. When using bipolar gradients, the control region was always very narrow. Qualitative comparison of the 4D-MRA demonstrated lower occurrence of partial labeling when using the optimized gradient parameters.

Conclusion: The shape of the ve-pCASL inversion profile can be optimized by changing G_{mean} and G_{max} to reduce partial labeling of untargeted arteries.

Introduction

In the last decade, dynamic MRA (4D-MRA) using arterial spin labeling (ASL) has become an important alternative to contrast-enhanced (CE) 4D-MRA in the brain. The use of ASL for 4D-MRA has several advantages, which are not only its ability to visualize arteries without using contrast agent, but also fewer constraints on the attainable spatial and temporal resolution, because ASL does not need to capture the first passage of the bolus (labeled blood) in real-time, unlike CE-4D-MRA. The ability to exclusively visualize the vascular tree arising from a selected artery by means of vessel selective labeling is an additional advantage of ASL-based MRA, which provides beneficial information for the diagnosis, treatment planning and follow-up of many cerebrovascular diseases (1,2).

Both pulsed-ASL (PASL) and pseudo-continuous ASL (pCASL) can provide vessel selective labeling, but their approaches are fundamentally different. In PASL, a spatially selective inversion slab is applied to the targeted artery or arteries, which is usually planned parallel to the arteries in the neck, so that the labeling pulse covers the target arteries over a long distance to label a sufficient amount of arterial blood (2-4). The benefit of the PASL technique for selective labeling is a sharp profile of the labeling slab, which achieves clear selectivity of the targeted artery from untargeted arteries. However, to label as much arterial blood as possible, the labeling slab has to cover a large part of the target artery, which frequently results in erroneous inclusion of other, untargeted arteries, because of tortuous vascular anatomy (5).

In contrast, in pCASL labeling of arterial blood is performed by means of flow-driven pseudo-adiabatic inversion in a thin labeling plane planned perpendicular to the flow direction. In vessel-encoded pCASL (ve-pCASL), additional gradients are applied in the in-plane (G_{xy}) direction, generating in-plane phase differences which produce a sinusoidal-like pattern of labeling and control conditions within the labeling plane (6). These are used to label different combinations of arteries in a Hadamard-encoding scheme, allowing SNR-efficient calculation of individual vessel-selective images in post-processing. Due to the thin labeling plane used, planning can be done with very little restrictions even when tortuous vascular anatomy is present in the inferior-superior direction. When looking into more detail at the in-plane spatial modulation, however, it will be noted that the transition between the labeling and the control conditions is much more gradual than the PASL profile by e.g. a hyperbolic secant or frequency offset corrected inversion (FOCI) pulse (7,8). This more gradual transition could easily lead to partial labeling of untargeted arteries, leading to reduced SNR-efficiency (6,9) and the requirement for complex post-processing to separate out the

individual contributions from each vessel. Previously, ve-pCASL with eight-cycled Hadamard-encodings was presented for ve-4D-MRA of four arteries with relatively high spatial and temporal resolution (10). For post-processing this study relied on Bayesian inference analysis to solve partial labeling of untargeted arteries (11). When considering application in clinical protocols, the eight encodings and their associated long scan time of 18 minutes, would be an important hurdle for its use and would make the examination prone to artefacts due to subject motion.

In this article, we investigate how the in-plane spatial modulation of the vessel selective inversion labeling in ve-pCASL can be controlled by changing the labeling parameters such as the maximum (G_{max}) and mean (G_{mean}) labeling gradient strength, so that a sharper spatial modulation and broader, flatter control regions can be achieved. With these improvements, a more SNR-efficient encoding can be performed. Moreover, the sharper inversion profile and broader, flatter control regions could enable two or more spatially distinct arterial branches to be encoded in a near-identical manner, such that they can be treated as a single artery in the analysis, allowing a reduced number of vessel-encodings to be performed. To this end, first Bloch simulations are performed to elucidate the relationship between the shape of the inversion profile and the pCASL labeling parameters. Subsequently, these findings are validated in an in vivo study. Finally, the optimized inversion profile of the ve-pCASL sequence is applied to a 4D-MRA protocol (6) to demonstrate the ability to allow both vertebral arteries (VAs) to be encoded as a single entity, despite their spatial separation. This enables a three-vessel encoding scheme, which only requires four-cycled Hadamard-encodings (12), thereby reducing the scan time by a factor of two compared to our previous sequence based on eight Hadamard-encodings (10).

Methods

Spatial modulation of ve-pCASL labeling

To devise a strategy for optimizing the inversion profile of ve-pCASL, we first revisit the mechanism which underlies this process and consider how it might be affected by various sequence parameters. For vessel selective labeling in ve-pCASL, additional gradients (G_{xy}) are applied in between the labeling RF pulses to generate in-plane phase differences. In one implementation G_{xy} is applied alternately positive and negative (Figure 1a) (6), whereas in another approach G_{xy} is not alternated (Figure 1b) (9). These two approaches will be subsequently referred to as the *bipolar approach* and *unipolar approach* throughout this article.

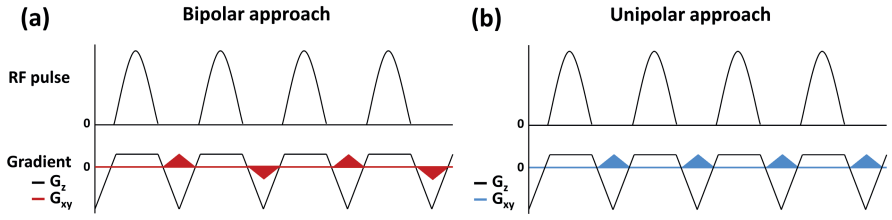


Figure 1: Schematic diagrams of pCASL labeling and additional gradients applied in the in-plane direction (G_{xy}), which are colored in red and blue, to achieve the spatial modulation. (a) In the bipolar approach, G_{xy} is applied alternately positive and negative, and (b) in the unipolar approach, G_{xy} is always played out with the same polarity.

In such vessel selective approaches, the additional phase accrual due to G_{xy} is superimposed upon the phase accrual of the flowing blood due to the non-zero mean gradient in the z-direction (G_{mean}) that produces the flow-driven pseudo-adiabatic inversion in pCASL. The inversion of the flowing blood magnetization will occur, therefore, where the additional net phase accrual due to G_{xy} is close to zero or multiples of 2π (with respect to the pCASL RF pulses), whereas the control condition is produced when this additional phase is in the opposed direction (with π shift). This results in a repeating pattern of labeling and control conditions across the labeling plane. What has not previously been considered, to the best of our knowledge, is the interaction between phase-accruals of the G_{xy} and G_{mean} gradients, both in the xy-plane as well as in the z-direction. In the unipolar approach the consistent application of two orthogonal gradients (G_{mean} and G_{xy}) means that the center of the inversion (where the net phase accrual is zero or a multiple of 2π) occurs on a series of tilted lines ("inversion lines"), as Figure 2a shows. The effective width where adiabatic inversion is performed in the flow direction ("w_{flow}" in Figure 2b) is determined by the gradient strength as used during the pCASL labeling (commonly known as G_{max}) in combination with the bandwidth of the RF pulses. The angle between the inversion line and the labeling plane ("$\theta_{inversion}$" in Figure 2b) will be determined by the relative strengths of G_{mean} and the time-averaged G_{xy} gradient (G_{xy}). Because it can be presumed that the flow-driven adiabatic inversion only occurs if blood water passes through an inversion line within the width of w_{flow}, the width of "W_{label}" in Figure 2b, which represents the in-plane width of labeling condition for vessel selective labeling, will be dependent on $G_{max,}$ G_{mean} and G_{xy}. In contrast, for the bipolar approach, no consistent inversion line is created due to the alternating G_{xy} gradient, as illustrated in Figure 2c. Instead, alternating G_{xy} gradient prevent the continuous accumulation of additional phase due to G_{xy} at off-center locations, thereby resulting in an apparently untilted inversion lines.

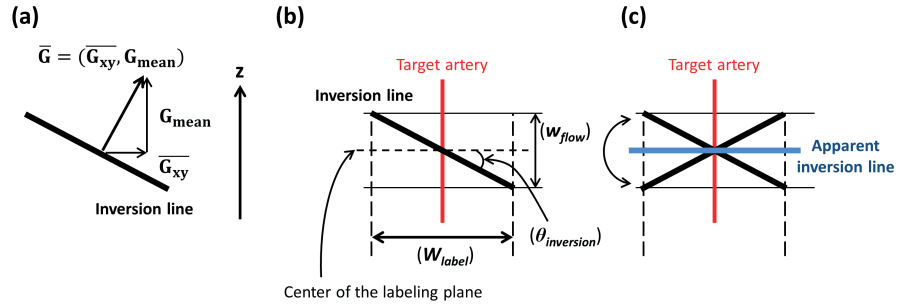


Figure 2: Schematic drawings illustrating: (a) the "inversion line", which is determined by the two orthogonal gradients, G_{mean} and G_{xy}, (b) w_{flow} indicating the distance over which adiabatic inversion occurs in the flow direction, $\theta_{inversion}$ the angle between the inversion line and the labeling plane, and W_{label} which represents the width of the labeling condition for vessel selective labeling. (c) In the bipolar approach, the inversion line is flipped every other G_{xy}, resulting in an averaged inversion line parallel to the labeling plane.

Bloch equation simulations

The inversion profile of ve-pCASL was investigated by Bloch equation simulations performed in MATLAB (Mathworks, Natick, MA, USA). The pCASL labeling parameters were varied to allow the identification of an optimal inversion profile shape with a sharp transition between labeling and control conditions. With both unipolar and bipolar approaches, the longitudinal magnetization (M_z) was simulated in two directions: first in the flow-direction to observe the temporal evolution of the adiabatic inversion, and secondly in the direction of G_{xy} to observe the resultant spatial modulation of the inversion. The shape of inversion profile was obtained at downstream from the center of inversion (z=0) at a distance approximately equivalent or greater than half of w_{flow}, ensuring that the M_z curves were stabilized at that point. The simulation was performed with flow velocities of 5, 10, 20, 30, 40, 50 and 60 cm/s. For the calculation of the inversion profile, M_z from all flow velocities were incorporated, assuming a laminar flow profile. For simplicity it was assumed that G_{xy} was applied only in the x-direction. The amplitude of G_{xy} was chosen to achieve a distance of 50 mm between the center of labeling and control conditions. Moreover, it was assumed that for on-resonance spins the center of the labeling condition occurs at the iso-center (x=0). Parameters for pCASL labeling were set as follows: G_{max} of 6.0 mT/m, G_{mean} of 0.8 mT/m, pCASL labeling RF pulse duration of 0.6ms, interval of 1.0 ms and flip angle of 20° (similar to Okell et al. (13)), and this set of parameters will be referred to as the *default settings*. Subsequently, G_{max} was varied from 7.0 mT/m to 2.0 mT/m in steps of 1.0 mT/m and G_{mean} was varied from 0.9 mT/m to 0.2 mT/m with 0.1 mT/m intervals. A longer RF

pulse interval of 1.2 ms, and different flip angles of 17° and 23° were also simulated. T_2 of blood was assumed to be 200 ms and T_1 recovery was neglected (6,14).

In vivo healthy volunteer study

Following the simulation study, two in vivo volunteer studies were conducted (i) to validate the spatial modulation of the inversion as observed in the simulation study, and (ii) to demonstrate the potential improvement of ve-pCASL 4D-MRA when using the selected optimal settings. All scans were performed on a Siemens 3T TIM Verio (Siemens Healthineers, Erlangen, Germany) under a technical development protocol agreed by local ethics and institutional committees. A total of six volunteers (female = 3, mean age = 36 years [range 27 – 46 years]) without known cerebrovascular disease participated in the studies, in which one participated only in study-(i), one participated in both studies, and the other four volunteers participated only in study-(ii).

(i) Validation of the inversion spatial modulation

To validate the inversion profile vessel selective labeling was performed within a labeling plane approximately 8cm below the circle of Willis, through the proximal V3 segment of the vertebral arteries (VAs), where the internal carotid arteries (ICAs) and VAs form an approximately rectangular arrangement. The transverse gradient (G_{xy}) was applied in the right-left (RL) direction with the amplitude corresponding to a π phase difference between the right ICA (RICA) and left ICA (LICA). The center of the selective labeling was first located at the RICA (i.e. the center of the control condition at the LICA) and was subsequently shifted toward the LICA in steps of 2 mm until the center of labeling condition reached the LICA (at the same time, the RICA will experience the center of the control condition). At each offset, two acquisitions were performed with an alternating π-phase difference of the labeling RF pulse train for the second acquisition, which effectively swaps the location of the control and labeling condition. Additionally, a pair of non-selective labeling and control conditions was acquired.

To simplify the post-processing and to keep the total examination time reasonably short, a low spatial resolution perfusion readout sequence (multi-slice single-shot echo planar imaging) was used, instead of a high-resolution 3D-MRA acquisition. The labeling duration and post-labeling delay (PLD) were set to shorter values than typical for perfusion imaging (1400 and 1000 ms respectively) to boost the SNR and keep the examination time short, thereby reducing the risk of subject motion.

Following the results of the Bloch equation simulations (see Results section), the unipolar approach was adopted and two combinations of G_{max} and G_{mean} were compared with the default settings (as defined in the simulation study) new setting-(A): G_{max} of 6.0 mT/m and G_{mean} of 0.4 mT/m, and new setting-(B): G_{max} of 3.0 mT/m and G_{mean} of 0.2 mT/m. All other parameters were kept equal to the default settings. Other perfusion imaging parameters were as follows: FOV 220 × 220mm, scan matrix 64×64, 4.5 mm slice thickness, 22 slices, echo time (TE)/repetition time (TR) of 14/3440 ms. A WET pre-saturation scheme was inserted before labeling (3,15), and two non-selective hyperbolic secant inversion pulses were applied during the PLD for background suppression. The number of offset steps from RICA to LICA varied depending on the distance between them: 27 and 24 steps for volunteer 1 and 2, respectively, which resulted in an average scan time of approximately 3 min for each setting of labeling parameters.

To measure the perfusion signal arising from the RICA and LICA separately, masks for the vascular territories were generated from a separate ve-pCASL scan acquired with eight Hadamard-encodings, as previously described (16). Using these masks, the mean signal intensity of each perfusion territory was measured for each offset, and they were normalized to values using non-selective labeling and control images as follows:

$$Normalised\ signal = -\left(\frac{nonselective\ control - selective\ labeling}{nonselective\ control - nonselective\ labeling}\right) \quad [1]$$

This suggests that perfect control or inversion will yield a values of 0 or -1, respectively. Finally, the normalized inversion profile curves were plotted as a function of the offset.

(ii) ve-pCASL 4D-MRA

To demonstrate the potential improvements achievable with the two newly proposed settings (A and B) compared with the default settings, 4D-MRA images were acquired in five subjects by means of a three-vessel encoding scheme with four Hadamard-encodings (previously proposed by Günther using a PASL labelling module (12)). Although labeling is performed at the level in the neck where the two VAs are widely separated (Figure 3a), the newly proposed parameter settings with the benefit of broader, flatter control regions allows us to treat both VAs as a single artery. On the time-of-flight image acquired before the 4D-MRA scan, the coordinate of the center of each artery was obtained, which was used to determine the distance between the center of the labeling and control conditions, as well as the direction of the G_{xy}

gradient. The labelling was performed as follows: 1st cycle: label condition at RICA, 2nd cycle: label condition at LICA, 3rd cycle: label condition at both VAs (see Figure 3b), and 4th cycle: label condition for all arteries (non-selective). The measured signal y can subsequently be written as follows:

$$\boldsymbol{y} = \begin{pmatrix} -1 & 1 & 1 & 1 \\ 1 & -1 & 1 & 1 \\ 1 & 1 & -1 & 1 \\ -1 & -1 & -1 & 1 \end{pmatrix} \begin{pmatrix} RICA \\ LICA \\ VAs \\ S \end{pmatrix} \quad [2]$$

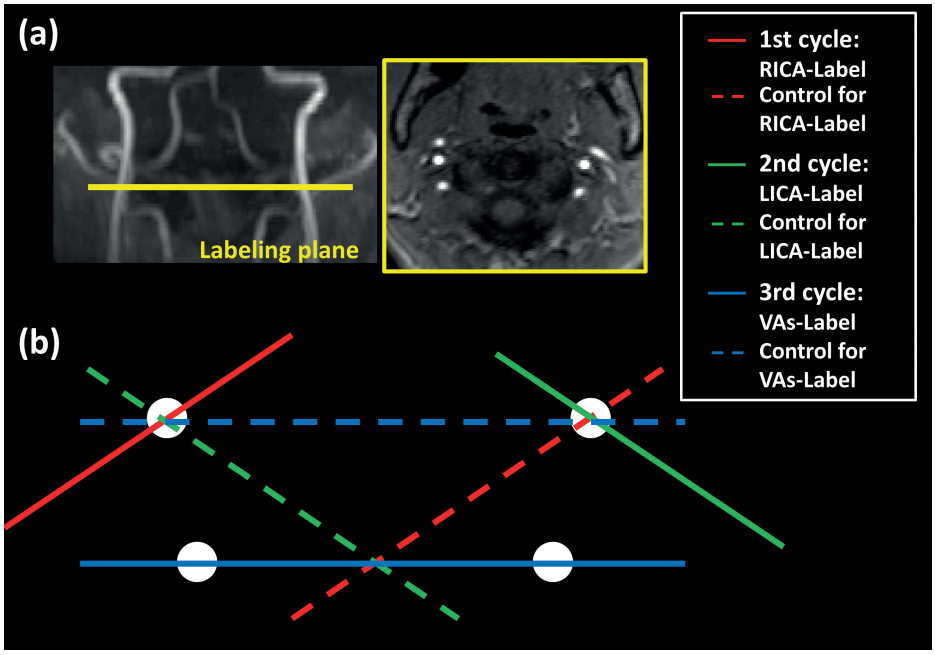


Figure 3: (a) Illustration of the planning of the pCASL labeling plane on the coronal and transverse angiography surveys. (b) Schematic figure illustrating the planning for the vessel-selective labeling of 1st (RICA-label), 2nd (LICA-label) and 3rd cycle (VAs-label). Red, green and blue colors indicate the 1st, 2nd and 3rd cycle. The dashed lines indicate the center of control condition of each cycle.

where *S* is static tissue. By applying the pseudo-inverse matrix of equation [2], vessels supplied by each feeding artery are visualized separately. For an optimal encoding function both VAs need to be placed equally well in the label or control conditions across all encoding cycles, allowing them to be treated as a single artery

for the analysis. This will optimise SNR-efficiency and allowing the simple form of the Hadamard-matrix (equation [2] above) to be used to decode the data without having to account for partial labelling of arteries in one or more encoding cycle. In this study, a 5th cycle consisting of a non-selective control condition was also added to allow the calculation of a non-selective 4D-MRA subtracted image for comparison, as described below.

The same three parameter settings using the unipolar approach were used as in study (i), i.e. the default settings, new setting-(A) and (B). The pCASL labeling duration was set to 500 ms, and a 4D SPGR Look-Locker (13,17) readout module was performed immediately after the end of labeling, in which 5 phases were acquired with a temporal resolution of 166.7ms. Acquisition parameters for the 4D SPGR were as follows: FOV 200 × 200mm, scan matrix 192 × 192, in-plane GRAPPA factor 4, 30 slices with a thickness 2.0 mm, readout excitation flip angle 7°, TR 9.3 ms, TE 4.9 ms. The scan time was 7:12 min for four encoding cycles (9 min including the non-selective control acquired for comparison).

From the decoded vessel-selective datasets (generated by applying the pseudo-inverse matrix of equation [2] to the images from the first four encoding cycles) and non-selective datasets (from the subtraction of non-selective label and control cycles only), maximum intensity projection (MIP) images were generated in the sagittal, transverse and coronal directions. A qualitative comparison among the three different parameter settings based upon the overall image quality and the degree of partial labelling of untargeted arteries was performed by a neuroradiologist with 13 years of experience (N.F.). The visual scoring system was as follows:

- For non-selective 4D-MRA
  (a) Clear visibility of posterior communicating (p-com) arteries (yes/no)
  (b) Visualization of arteries (3: good, 2: moderate, 1: very poor)
- For ve-4D-MRA
  (c) Presence of partial labelling of untargeted arteries (3: not observed, 2: slightly present, 1: very obviously present)
  (d) Visualization of arteries (3: good, 2: moderate, 1: very poor)

Results

Bloch equation simulations

Figure 4 shows color-coded 2D-maps of M_z in the flow-direction (from the bottom to the top of the images) and in the direction of G_{xy} (left-right in the images) for the unipolar approach (4a) and bipolar approach (4b), respectively. As a representative example, only data simulated with a flow velocity of 30 cm/s is shown. The predicted tilted inversion line for the unipolar approach (see Figure 2b) was confirmed, as can be concluded from Figure 4a by looking at the tilted transition line between before (in red) and after inversion (in blue). As hypothesized, a smaller G_{max} indeed led to a wider w_{flow}, whereas a smaller G_{mean} produced steeper $\theta_{inversion}$. For bipolar gradients, in contrast, the inversion line was parallel to the pCASL labeling plane as also hypothesized by the averaging effect of the alternating G_{xy}, as illustrated in Figure 2c.

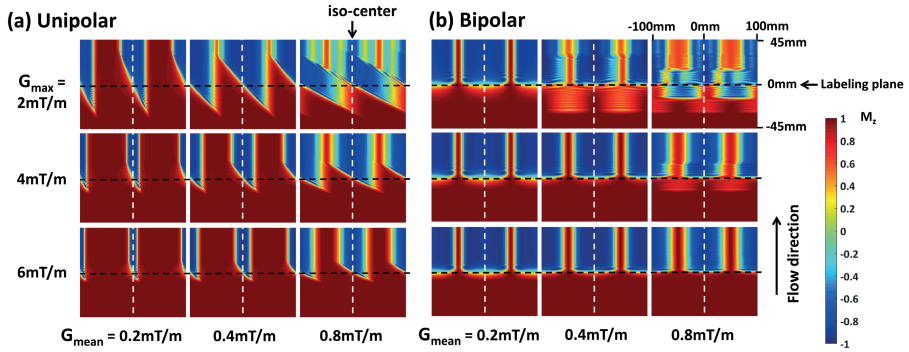


Figure 4: Color-coded 2D-maps of the simulated M_z as a function of distance in the direction of G_{xy} (left-right in these images) and in the flow-direction (bottom to top), using (a) the unipolar approach and (b) the bipolar approach for a range of G_{max} and G_{mean} values. Red and blue colors show the uninverted and inverted magnetization, respectively. Only data simulated with a flow velocity of 30 cm/s is shown.

In Figure 5, color-coded 2D-maps obtained by the unipolar approach with flow velocities of 10 cm/s (5a) and 50 cm/s (5b) are shown. As shown in the original ve-pCASL article by Wong (Fig. 2b in (6)), the spatial modulation of the inversion (i.e. M_z in the x-direction) is influenced by flow velocity. In 2D-maps with different flow velocities of 10 cm/s (5a), 30 cm/s (4a) and 50 cm/s (5b), a difference of the transition between the labeling to the control conditions in the direction of G_{xy} was notable. However, the same trends as for 30 cm/s were observed between G_{max} and w_{flow}, as well as between G_{mean} and $\theta_{inversion}$. Additionally, color-coded 2D-maps obtained with stronger G_{xy} to achieve a distance of 15 mm between the center of labeling and

control conditions, which is approximately the anterior-posterior distance between the ICAs and VAs, are shown in Figure 6. This figure suggests that the narrower setting to achieve anterior-posterior discrimination between the ICAs and VAs results in a very narrow labeling condition, which could cause suboptimal labeling as also seen in the in vivo study (see Discussion section), although the modulation patterns are proportionally identical to the ones with 50 mm distance.

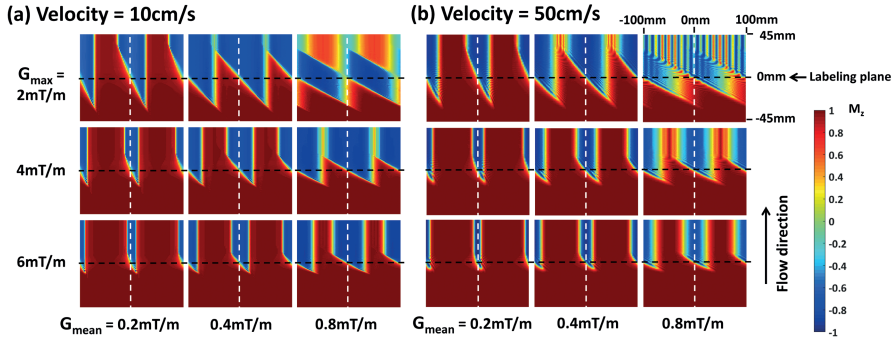


Figure 5: Color-coded 2D-maps of the simulated M_z as a function of distance in the direction of G_{xy} (left-right in these images) and in the flow-direction (bottom to top), with flow velocities of (a) 10 cm/s and (b) 50 cm/s. Red and blue colors show the uninverted and inverted magnetization, respectively. Only data simulated by unipolar approach is shown.

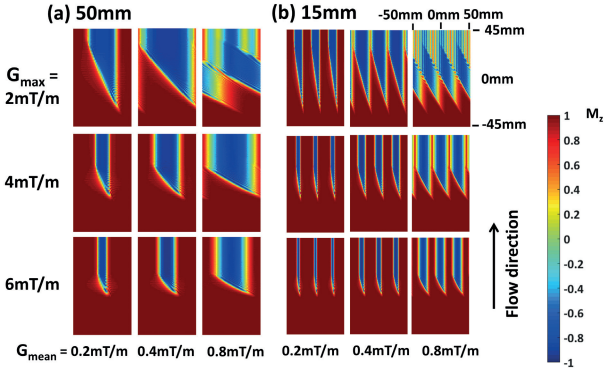


Figure 6: Color-coded 2D-maps of the simulated M_z as a function of distance in the direction of G_{xy} (left-right in these images) and in the flow-direction (bottom to top), with G_{xy} to achieve a distance of (a) 50 mm which is approximate distance between right and left ICAs, and (b) 15 mm which is approximate anterior-posterior distance between ICAs and VAs, between the center of labeling and control conditions. Red and blue colors show the uninverted and inverted magnetization, respectively. Only data simulated by unipolar approach is shown.

At the center of the label condition in the x-direction (i.e. at the center of the targeted artery), flow-driven adiabatic inversion showed slightly different evolution for different G_{max} and G_{mean} settings: with fixed G_{mean} (Figure 7a), inversion started and ended further from the labeling plane when G_{max} was lower, which reflects the thickness of the pCASL labeling plane. Note that the trajectory of M_z close to the middle of the labeling plane (i.e. when M_z is crossing 0) was very similar for all G_{max} values (indicated by an arrow in Figure 7a). In contrast, higher G_{mean} resulted in faster inversion when G_{max} was kept constant (Figure 7b).

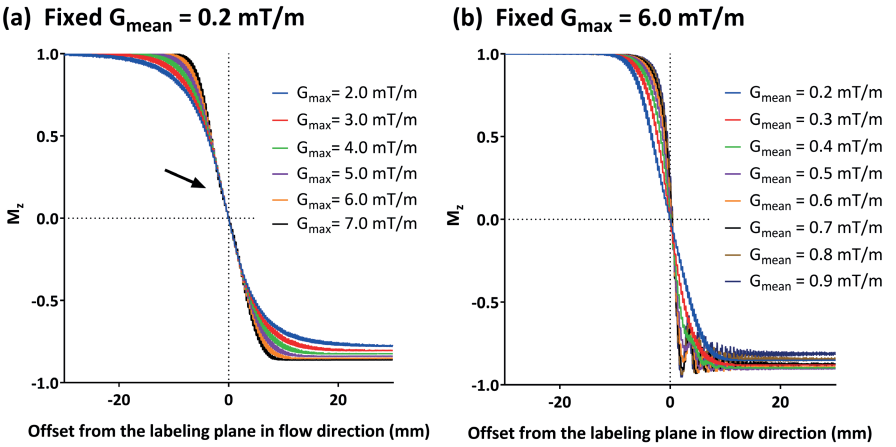


Figure 7: Simulated M_z showing the evolution of the flow-driven pseudo-adiabatic inversion at the location of the targeted artery (iso-center), with (a) fixed G_{mean} and variable G_{max}, and (b) fixed G_{max} and variable G_{mean}. Only data simulated with a flow velocity of 30 cm/s is shown.

Figure 8 shows representative spatial modulation of the inversion as obtained with the bipolar (8a and 8b) and unipolar approach (8c and 8d). For the bipolar approach, the control condition (indicated by arrows) was very narrow for all studied combinations of G_{max} and G_{mean}, which was considered suboptimal for the purpose of this study. Therefore, further in vivo studies were only performed using the unipolar approach, which does allow tuning the width of the control condition. When using the unipolar approach, flat control regions were obtained over a wide distance for many combinations of G_{max} and G_{mean} (Figure 8c and 8d). As Figure 8c shows, the steepness of the inversion profile was similar for all G_{max} when G_{mean} was kept constant (at 0.2 mT/m in Figure 8c), whereas larger G_{max} resulted in a narrower labeling condition and wider control condition. In contrast, with fixed G_{max} (at 6.0 mT/m in Figure 8d) lower G_{mean} resulted in a steeper inversion profile.

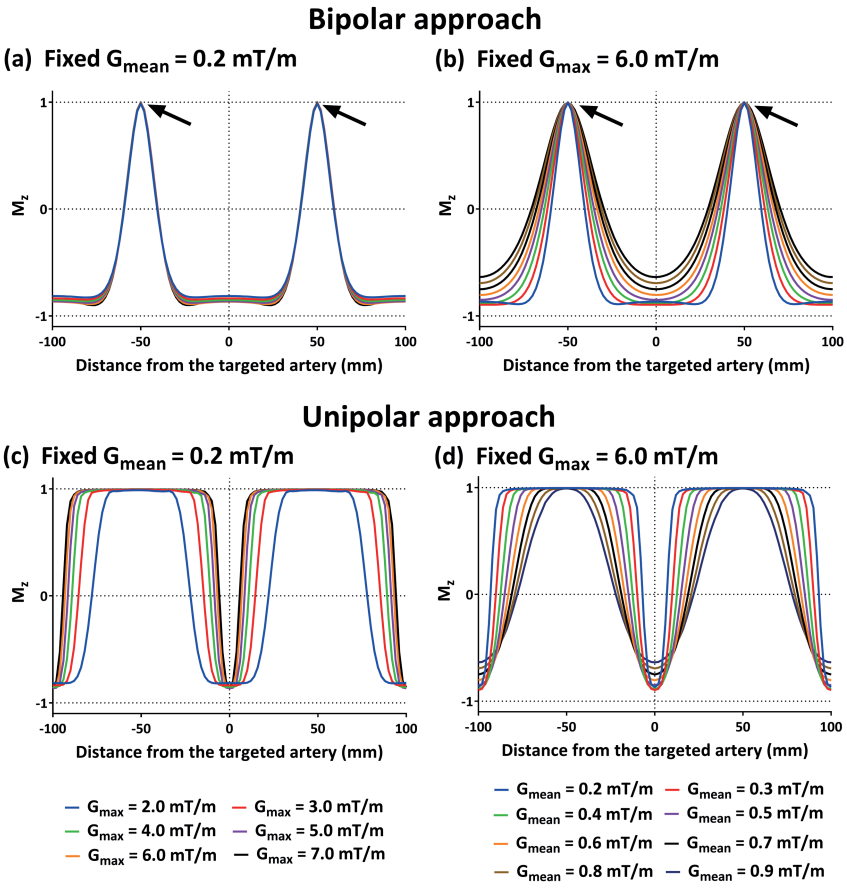


Figure 8: Simulated inversion profile curves (M_z as a function of distance along x), which were obtained downstream from the center of inversion (z=0) at a distance approximately equivalent or greater than half of w_{flow}. (a) Bipolar approach, variable G_{max} and fixed G_{mean} at 0.2 mT/m (b) Bipolar approach, fixed G_{max} at 6.0 mT/m and variable G_{mean}, (c) Unipolar approach, variable G_{max} and fixed G_{mean} at 0.2 mT/m (d) Unipolar approach, fixed G_{max} at 6.0 mT/m and variable G_{mean}. Black arrows indicate the very narrow control condition obtained with the bipolar approach across all gradient settings.

As Figure 9a indicates, when G_{max} is small and/or G_{mean} is large (i.e. a small ratio of G_{max}/G_{mean}), the control condition becomes very narrow and with an even smaller ratio of G_{max}/G_{mean} the shape of inversion profile starts to become irregular. In such settings, disturbances were also observed during the flow-driven adiabatic inversion (Figure 9b, G_{max} = 2.0 mT/m and G_{mean} = 0.8 mT/m at flow velocity of 30 cm/s). With the same combination of G_{max} and G_{mean}, Figure 4a (upper right) shows overlapping of tilted inversion lines, from which it can be deduced that the magnetization experiences

multiple inversion planes, leading to highly irregular behavior.

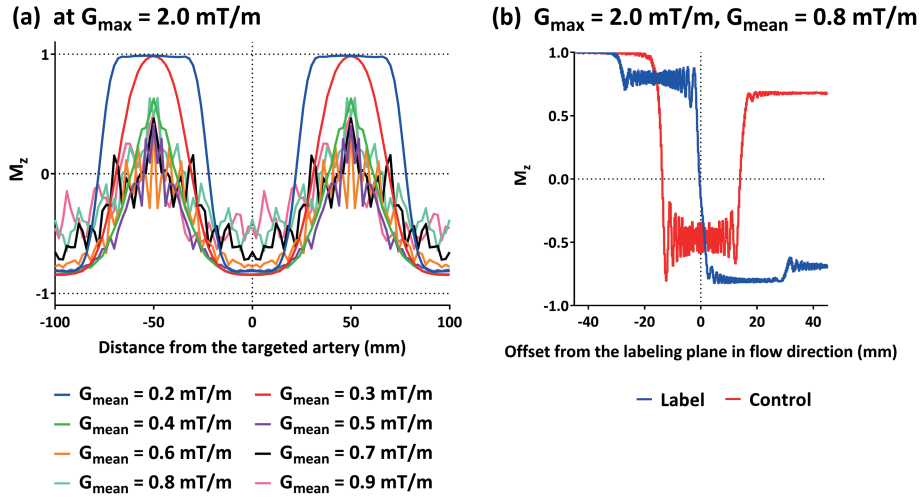


Figure 9: (a) The inversion profile curves (M_z as a function of location along x) simulated with small G_{max} and large G_{mean} (i.e. small ratio of G_{max}/G_{mean}), generating irregular shapes of the inversion profile. (b) The evolution of flow-driven pseudo-adiabatic inversion simulated with G_{max} = 2.0 mT/m and G_{mean} = 0.8 mT/m at flow velocity of 30 cm/s, showing the disturbance of inversion.

Spatial modulations produced with different pCASL flip angles of 17° (Figure 10b and 11b) and 23° (10c and 11c) resulted in slightly lower and higher inversion efficiencies for some combinations of G_{max} and G_{mean}, but in general the results are very similar. Also, a longer RF interval of 1.2 ms (10d and 11d) caused only slightly reduced inversion efficiency for some combinations of G_{max} and G_{mean}. However, none of these changes in RF pulse parameter settings caused important changes to the inversion profiles. Based on the results from the simulation studies, for the in vivo studies two combinations of G_{max} and G_{mean} were selected: (A) G_{max} = 6.0 mT/m, G_{mean} = 0.4 mT/m and (B) G_{max} = 3.0 mT/m, G_{mean} = 0.2 mT/m using the unipolar approach. The setting-(B) was chosen because (i) the lowest G_{mean} = 0.2 mT/m resulted in the sharpest transition between the labeling and the control conditions, and (ii) a G_{max} higher than 3.0 mT/m resulted in too narrow labeling conditions as compared to the control condition. The setting-(A) was chosen because the combination of G_{max} = 6.0 mT/m and G_{mean} = 0.4 mT/m generates a similar shape of the inversion profile to the setting-(B) (see Figure 12a) while using the same G_{max} as the default setting. This allowed the investigation of whether a lower G_{max} in the setting-(B) (which generates the wider "w_{flow}") might introduce adverse effects on the inversion profile in in vivo studies, due to the greater likelihood of non-straight vessels within a

broader labeling region. RF pulse duration and interval, as well as the flip angle were kept equal to the default setting (respectively 0.6 ms, 1.0 ms and 20º, see Figure 12a).

In vivo healthy volunteer study

(i) Validation of the inversion spatial modulation

Figure 12b shows the inversion profile curves measured from both volunteers. These plots show the normalized inversion of the mean signal from the RICA and LICA perfusion territories as a function of the vessel selective labeling offset from the target artery. Although some small signal offsets, due to scanner drift across the experiments, and minor shifts in the curves, due to possible off-resonance effects, were evident, sharper inversion profiles were clearly observed in both volunteers for the new settings as compared to the default settings.

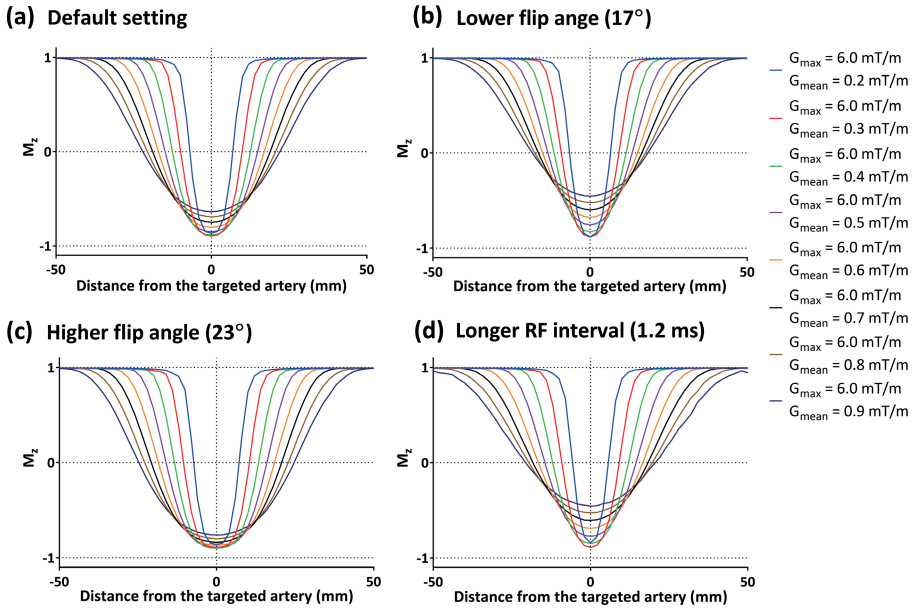


Figure 10: Comparison of the simulated inversion profile curves (fixed G_{max} at 6.0 mT/m and variable G_{mean}) when using different pCASL flip angles and RF intervals: (a) the default setting with RF duration = 0.6 ms, RF interval = 1.0 ms, flip angle = 20º, (b) lower flip angle of 17º, (c) higher flip angle of 23º, and (d) longer RF interval of 1.2 ms.

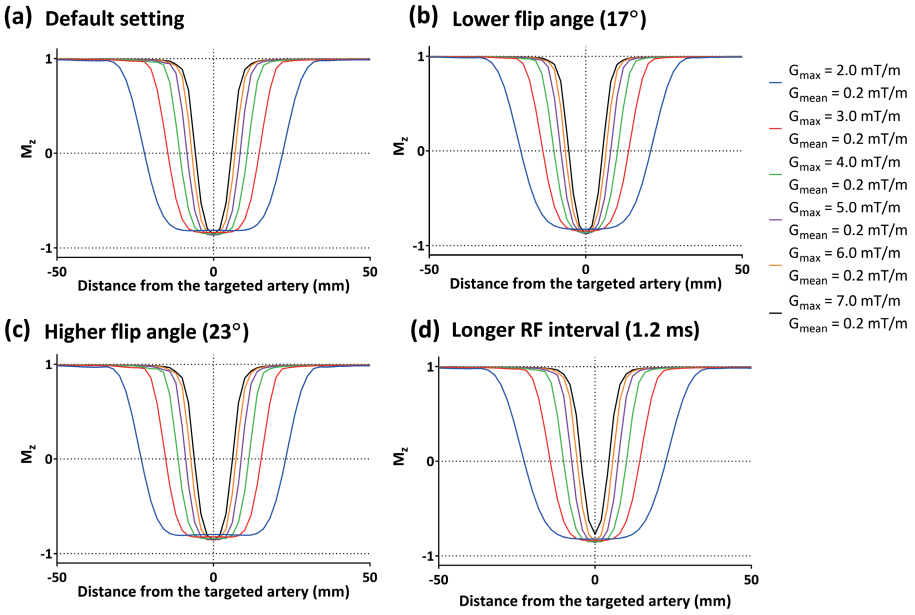


Figure 11: Comparison of the simulated inversion profile curves (variable G_{max} and fixed G_{mean} at 0.2 mT/m) when using the different pCASL flip angles and RF interval: (a) the default setting with RF duration = 0.6 ms, RF interval = 1.0 ms, flip angle = 20°, (b) lower flip angle of 17°, (c) higher flip angle of 23°, and (d) longer RF interval of 1.2 ms.

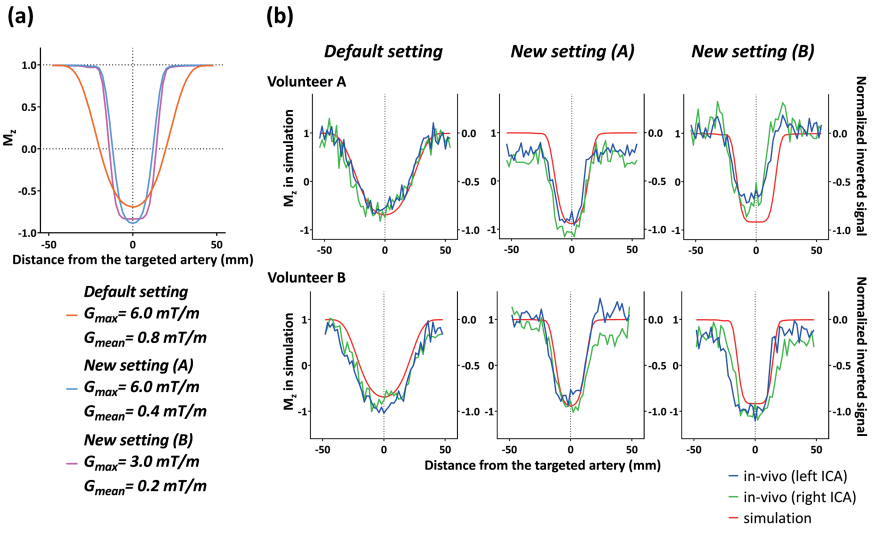


Figure 12: (a) The inversion profile curves simulated with the default setting G_{max} = 6.0 mT/m, G_{mean} = 0.8 mT/m and two new settings (A) G_{max} = 6.0 mT/m, G_{mean} = 0.4 mT/m and (B) G_{max} = 3.0 mT/m, G_{mean} = 0.2 mT/m, which were used for further in vivo studies, and (b) the inversion profile curves measured from two volunteers.

(ii) ve-pCASL 4D-MRA

Representative ve-4D-MRA images from one of the healthy volunteers are shown in Figure 13. (In Figure 13, only representative single phase is shown. For all five phases from this volunteer, and representative single phase from all five volunteers, see Supporting Information Figure S1 and S2, respectively.) The mean distance between RICA and LICA and between ICAs and VAs (which was represented as the distance between each central location of ICAs and VAs) were 53.6 and 12.3 mm, respectively. When using the default settings, partial labeling of VAs was observed as indicated by arrows. With both of the proposed new settings, however, no partial labeling could be observed and a clear separation was achieved for all targeted arteries, despite the separation of the VAs within the labeling plane.

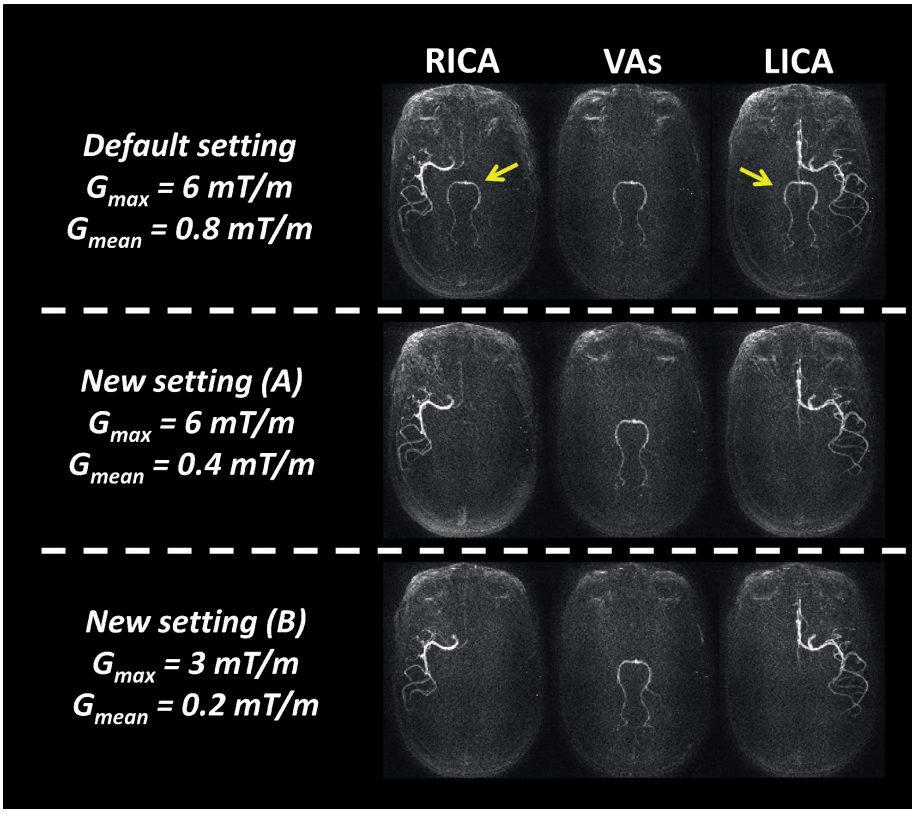


Figure 13: Representative ve-pCASL 4D-MRA images from one healthy volunteer acquired using the default settings (G_{max} = 6.0 mT/m, G_{mean} = 0.8 mT/m), the new setting (A) (G_{max} = 6.0 mT/m, G_{mean} = 0.4 mT/m) and (B) (G_{max} = 3.0 mT/m, G_{mean} = 0.2 mT/m). Only representative single phase is shown. Yellow arrows indicate the partial labeling of untargeted arteries observed with the default setting which were not evident with both optimized settings.

The summary of the observer study is shown in Table 1. Although the flow through the p-com was visualized in two out of the five volunteers, the visualization of untargeted arteries due to the partial labeling could be distinguished from it. In RICA and LICA labeling, the default settings resulted in more frequent and severe partial labeling than when using the new settings. Statistical comparison by means of a paired t-test between the default (mean value of 2.13) and both new settings combined (mean value of 2.67) showed that this difference was statistically significant ($p<0.005$). These results suggest that the sharper inversion profile indeed reduced the occurrence of partial labeling of untargeted arteries.

In ve-4D-MRA, slightly lower signal intensity was observed in the posterior cerebral arteries (PCAs) when using the new settings in some of the volunteers, although statistical comparisons of the mean visual scores via paired t-tests between the default and both new settings combined did not result in statistical significance for any arterial territory: 3.0 v.s. 3.0 ($p = N/A$) for RICA, 2.8 v.s. 3.0 ($p = 0.168$) for LICA, and 2.6 v.s. 2.2 ($p = 0.104$) for VAs. For the non-selective 4D-MRA, however, such a lower intensity as compared to the default setting was not observed, which suggests that this observation cannot be attributed to a decrease in the labeling efficiency due to the new settings. We refer to the discussion section for possible explanations.

Table 1: Summary of the qualitative scoring of ve-pCASL 4D-MRA, using the default setting (G_{max} = 6.0 mT/m, G_{mean} = 0.8 mT/m), the new setting (A) (G_{max} = 6.0 mT/m, G_{mean} = 0.4 mT/m) and (B) (G_{max} = 3.0 mT/m, G_{mean} = 0.2 mT/m).

For non-selective 4D-MRA

	Number of subjects
(a) Clear visibility of p-com arteries	2

	Parameter setting	Mean score
(b) Visualization of arteries	Default	3.0
	New (A)	3.0
	New (B)	3.0

For ve-pCASL 4D-MRA

	Parameter setting	RICA	LICA	VAs
(c) Presence of partial labelling of untargeted arteries	Default	1.4	2.0	3.0
	New (A)	2.4	2.8	3.0
	New (B)	2.4	2.8	2.6
(d) Visualization of arteries	Default	3.0	2.8	2.6
	New (A)	3.0	3.0	2.4
	New (B)	3.0	3.0	2.0

Discussion

In this study, we have presented how the in-plane spatial modulation of ve-pCASL can be controlled by changing the labeling parameters, G_{max} and G_{mean}. By optimization, a sharper spatial modulation and broad, flat control regions were achieved, which allowed us to treat spatially distinct vessels, like the two VAs, as one single artery. This allowed us to use a three-vessel four-cycle Hadamard-encoding for 4D-MRA acquisition, which halved the scan time from our previous four-vessel eight-cycle Hadamard-encoding 4D-MRA.

From the Bloch equation simulation studies, three major observations can be made. Firstly, for the unipolar approach, a flat control condition was obtained over a wide distance, whereas the bipolar approach produced a narrow control condition, which was considered suboptimal for the purpose of this study. The difference between these two approaches can be attributed to the angulation of the inversion line: for the bipolar gradients the inversion line is flipped every other G_{xy}, which prevents additional cumulative phase accruals due to G_{xy} at off-center locations. This appears to result in the inversion being achieved over relatively wide region until the alternation of G_{xy} starts to behave as an alternating π phase shift, thereby generating the control condition. It also explains why settings with different G_{max} in combination with fixed G_{mean} generate very similar spatial inversion modulations, while keeping the pointed narrow control condition. Secondly, in unipolar approach a higher G_{max} produced a narrower region for the labeling condition with a wider control condition, while keeping the spatial transition between the labeling and control conditions similar for all G_{max}. From the schematic depiction of Figure 2, a lower G_{max} and thus a larger thickness of the pCASL labeling pulse will result in a wider w_{flow}, which was indeed observed as the wider inversion range for the M_z in the flow direction (see Figure 4a), whereas the angle of the tilted inversion line ("$\theta_{inversion}$" in Figure 2a) was constant for all G_{max}. It is therefore to be expected that a smaller G_{max} with wider w_{flow} result in a wider label condition ("W_{label}" in Figure 2a). Thirdly and finally, a smaller G_{mean} results in a steeper transition between labeling and control conditions, which can be explained by the following fact: the tilted inversion line indicates the center of the pseudo-adiabatic inversion in the flow-direction (i.e. where M_z crosses 0). When this line is not parallel to the labeling plane, this inversion center will shift from the center of the labeling plane along the flow-direction as a function of the offset from the target artery in the x-direction. When the center of adiabatic inversion occurs too close to the edge of w_{flow}, the adiabatic inversion starts to fail because the spins are no longer effectively tipped by the slice-selective pCASL pulse. In other words, the spins have left the labeling slab before full inversion has been achieved. A lower G_{mean} increases

the angle of the inversion line, thereby resulting in a failure to achieve full inversion closer to the targeted artery, i.e. resulting in a steeper spatial transition.

For vessel-selective ASL imaging, the simplest approach is to perform a pair-wise labeling and control acquisition for a single targeted artery (1,2,4). When all major arteries (RICA, LICA and VAs) would be acquired in such a manner, however, the paired acquisitions of labeling and control conditions would require six acquisitions and therefore take considerable scan time. Therefore, several more time-efficient approaches have been proposed: for example, the dual-vessel labeling scheme of Zimine et. al. (5) in which each of the ICA and both of VAs are labeled simultaneously and, after subtraction from each control image, arterial signal from each ICA is isolated by assigning ASL signal present in both images as arterial blood originating from the VAs. Therefore, the total scan time for all major arteries will only be two-thirds of the one-by-one acquisition, although special care is needed to judge whether signal is from the VAs or could also be due to actual mixing of blood from both ICAs. Such a risk of misinterpretation can be avoided by using a Hadamard-encoded ve-ASL scheme as proposed by Günther for PASL (12) and Wong for pCASL (6). This is a highly efficient approach for perfusion imaging in which repeated measurements for signal averaging can be replaced by multiple Hadamard-encodings without loss in SNR, i.e. vessel-encoding is done without a time penalty because an equal number of raw images are used to generate the perfusion images. However, such a free-lunch benefit is not possible for a 4D-MRA acquisition, because ASL-based MRA usually relies on a 3D multi-shot readout with a high spatial resolution, and the entire scan time is spent for spatial encoding, rather than averaging. Therefore, scan time for ve-4D-MRA would increase proportionally to the number of applied vessel-encodings as compared to a non-selective 4D-MRA scan. In this study, we use a three-vessel encoding scheme, which only requires four Hadamard-encodings. However, such a scheme requires both VAs to behave as a single artery, necessitating stricter planning of labeling and especially a broad, flat control region to avoid partial labeling of one of the two spatially separated VAs. By using the sharper ve-pCASL inversion profile with the broader control regions as found in our simulation study, partial labeling of untargeted arteries could be minimized, thereby allowing the Hadamard-four scheme without having to account for partial labeling in post-processing. This halved the scan time compared to our previous study using eight Hadamard-encodings of four arteries (10). An alternative approach would be to account for the occurrence of partial labeling, by including the non-ideal inversion efficiency for each artery at each vessel-encoding cycle into the post-processing, for example by applying a Bayesian analysis approach (11). It should be noted, however, that presence of partial labeling reduces SNR-efficiency even though such a sophisticated analysis might enable proper vessel differentiation.

There are several limitations in this study. First, as the observer study shows, slightly lowered signal intensity was observed in the PCAs of some of volunteers, more frequently when employing the new settings. Because the accompanying non-selective 4D-MRA image acquired with the same settings for pCASL-labeling did not show decreased signal intensity compared to the default settings, the possibility of a globally lowered labeling efficiency can be ruled out. The lower intensity is presumed to be caused by suboptimal labeling of the targeted arteries (VAs), possibly due to the narrower labeling condition as present with the optimized settings. In this study, the center of each artery was measured on the time-of-flight image prior to the 4D-MRA scan, and the distance between those arteries was used to determine the distance between the center of the labeling and control conditions. This last distance also determines the width of the label and control regions. Because the distance between ICAs and VAs was often quite small, this also might have caused the labeling condition to become too narrow to effectively cover both VAs. However, this study has shown that the control condition can be much wider and flatter by using the newly proposed settings of G_{max} and G_{mean}, which does offer more freedom in choosing the distance between the center of labeling and control conditions, i.e. it is not necessary to locate the untargeted arteries exactly at the center of the control condition, and the lowered visualization of PCA could be avoided by optimizing the width of the labeling condition. Another explanation could be that B_0 inhomogeneity could have caused a shift of the spatial distribution of the labeling/control pattern, which could also explain some of the asymmetry as observed in the in vivo plots of the spatial inversion profile (see Figure 12b).

The second limitation is that only a straight artery was modelled in the simulation study and that performance of the newly proposed settings could be different for a tortuous artery. Although in the results of in vivo studies there was not any evident differences between the two newly proposed settings of G_{max} of 3.0 mT/m and 6.0 mT/m, a wider "w_{flow}" as produced by a low G_{max} (such as 2.0 or 3.0 mT/m) could result in a poorer inversion profile in a tortuous artery. This is similar for non-selective pCASL imaging and was therefore not considered the main goal of the current study, which focuses on the underlying mechanisms of how the shape of inversion profile is altered by the gradient parameters, which may help further protocol optimizations.

The third one is that, as also mentioned in the results section, some signal offsets and shifts in the inversion profile curves were observed in the in vivo study (Figure 12b), which could be attributed to the scanner drift across the scans and possible off-resonance effects. However, there were some more limitations when considering the experimental design: because of scan time restrictions, the inversion profile was

obtained with a single average and at a short PLD, which means that the measured signal came from relatively large arteries rather than tissue, which caused some unwanted signal fluctuations. Moreover, the inversion profile curves obtained from two volunteers were not averaged to generate the mean inversion profile curve, because the distance between the right and left ICAs was not identical for these two volunteers. These limitations resulted in the rather noisy inversion profile curves, albeit confirming the general findings of the simulations.

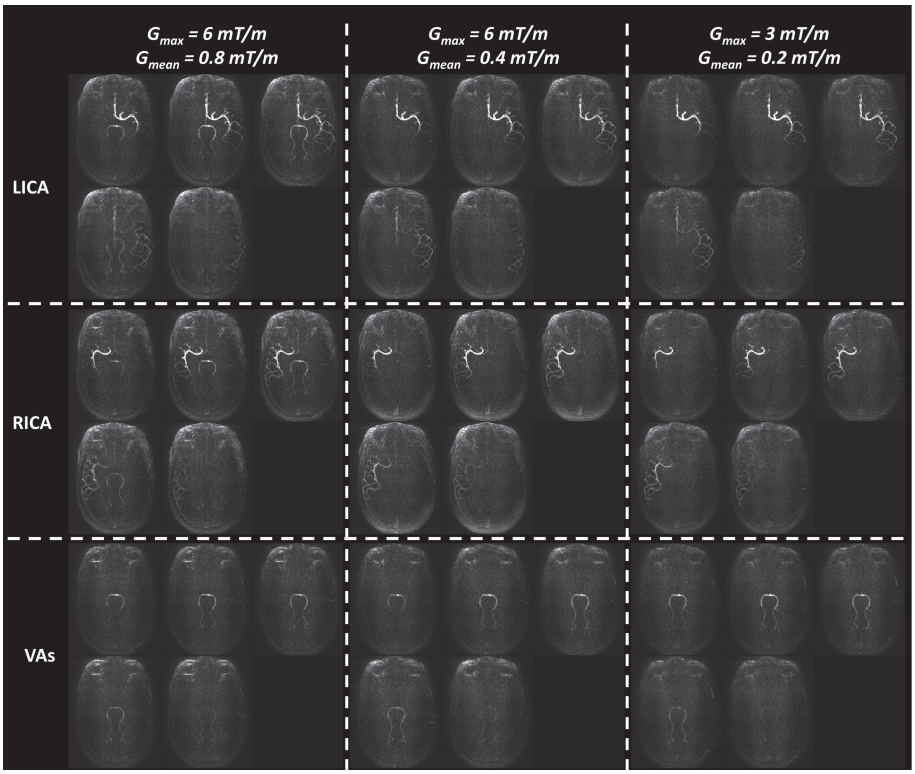
Lastly, we only tested our optimized settings for ve-pCASL 4D-MRA in five healthy volunteers. In patient examinations, the occurrence of motion could be more frequent than in volunteer studies. Although the shorter scan time achieved by using our optimized settings could reduce the risk of motion occurrence, too narrow a labeling condition could reduce the labeling efficiency when motion occurs. Therefore, further optimization might be required for patient examinations.

Conclusion

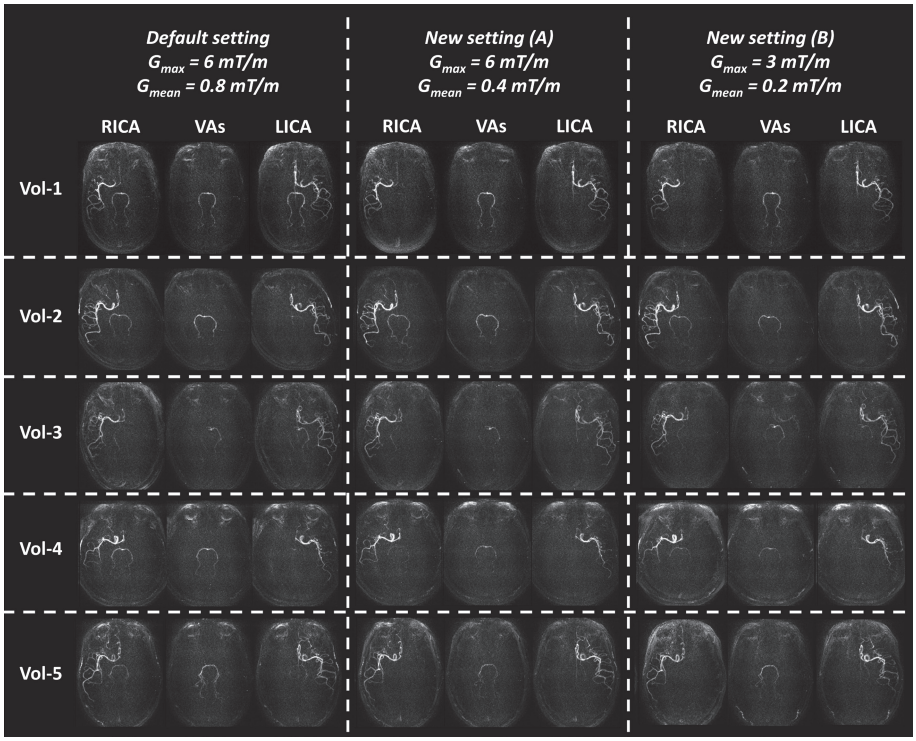
In summary, we have determined how changes in G_{max} and G_{mean} influence the spatial modulation of the inversion profile for vessel-encoded pCASL, with the specific goal in mind of allowing a faster acquisition for ve-pCASL 4D-MRA. A narrower labeling condition, larger and flatter control condition and sharper transition for the newly proposed settings were subsequently proven to allow 4D-MRA images of high quality in shorter scan time in the in vivo healthy volunteer study, and it was shown that the use of new settings lowered the risk of partial labeling of untargeted arteries.

Acknowledgements

This research was supported by the EU under the Horizon2020 program (project: CDS-QUAMRI). TO is funded by the UK Royal Academy of Engineering. The Wellcome Centre for Integrative Neuroimaging is supported by core funding from the Wellcome Trust (203139/Z/16/Z).



Supporting Information Figure S1: Representative ve-pCASL 4D-MRA images from one of the healthy volunteers.



Supporting Information Figure S2: ve-pCASL 4D-MRA images from all volunteers obtained from this study. Only representative single phase is shown.

References

1. Jensen-Kondering U, Lindner T, van Osch MJ, Rohr A, Jansen O, Helle M. Superselective pseudo-continuous arterial spin labeling angiography. Eur J Radiol 2015;84(9):1758-1767.
2. Fujima N, Osanai T, Shimizu Y, Yoshida A, Harada T, Nakayama N, Kudo K, Houkin K, Shirato H. Utility of noncontrast-enhanced time-resolved four-dimensional MR angiography with a vessel-selective technique for intracranial arteriovenous malformations. J Magn Reson Imaging 2016;44(4):834-845.
3. Golay X, Petersen ET, Hui F. Pulsed star labeling of arterial regions (PULSAR): a robust regional perfusion technique for high field imaging. Magn Reson Med 2005;53(1):15-21.
4. Hendrikse J, van der Grond J, Lu H, van Zijl PC, Golay X. Flow territory mapping of the cerebral arteries with regional perfusion MRI. Stroke 2004;35(4):882-887.
5. Zimine I, Petersen ET, Golay X. Dual vessel arterial spin labeling scheme for regional perfusion imaging. Magnetic Resonance in Medicine 2006;56(5):1140-1144.
6. Wong EC. Vessel-encoded arterial spin-labeling using pseudocontinuous tagging. Magnetic Resonance in Medicine 2007;58(6):1086-1091.
7. Suzuki Y, Fujima N, Ogino T, Meakin JA, Suwa A, Sugimori H, Van Cauteren M, van Osch MJ. Acceleration of ASL-based time-resolved MR angiography by acquisition of control and labeled images in the same shot (ACTRESS). Magn Reson Med 2017.
8. Berry ES, Jezzard P, Okell TW. An Optimized Encoding Scheme for Planning Vessel-Encoded Pseudocontinuous Arterial Spin Labeling. Magn Reson Med 2015;74(5):1248-1256.
9. Wong EC, Guo J. Blind detection of vascular sources and territories using random vessel encoded arterial spin labeling. MAGMA 2012;25(2):95-101.
10. Okell TW, Schmitt P, Bi X, Chappell MA, Tijssen RH, Sheerin F, Miller KL, Jezzard P. Optimization of 4D vessel-selective arterial spin labeling angiography using balanced steady-state free precession and vessel-encoding. NMR Biomed 2016;29(6):776-786.
11. Chappell MA, Okell TW, Payne SJ, Jezzard P, Woolrich MW. A fast analysis method for non-invasive imaging of blood flow in individual cerebral arteries using vessel-encoded arterial spin labelling angiography. Med Image Anal 2012;16(4):831-839.
12. Gunther M. Efficient visualization of vascular territories in the human brain by cycled arterial spin labeling MRI. Magnetic Resonance in Medicine 2006;56(3):671-675.
13. Okell TW, Chappell MA, Woolrich MW, Gunther M, Feinberg DA, Jezzard P. Vessel-encoded dynamic magnetic resonance angiography using arterial spin labeling. Magn Reson Med 2010;64(2):430-438.
14. Chen JJ, Pike GB. Human whole blood T2 relaxometry at 3 Tesla. Magn Reson Med 2009;61(2):249-254.
15. Ogg RJ, Kingsley PB, Taylor JS. WET, a T1- and B1-insensitive water-suppression method for in vivo localized 1H NMR spectroscopy. J Magn Reson B 1994;104(1):1-10.
16. Okell TW, Chappell MA, Kelly ME, Jezzard P. Cerebral blood flow quantification using vessel-encoded arterial spin labeling. J Cereb Blood Flow Metab 2013;33(11):1716-1724.
17. Sallustio F, Kern R, Gunther M, Szabo K, Griebe M, Meairs S, Hennerici M, Gass A. Assessment of intracranial collateral flow by using dynamic arterial spin labeling MRA and transcranial color-coded duplex ultrasound. Stroke 2008;39(6):1894-1897.

Chapter 4

Acceleration of Vessel-Selective Dynamic MR Angiography by pCASL in Combination with Acquisition of Control and Labeled Images in the Same Shot (ACTRESS)

submitted to Magn Reson Med, in revision

Yuriko Suzuki
Thomas W. Okell
Noriyuki Fujima
Matthias J. P. van Osch

Abstract

Purpose: The recently introduced "Acquisition of ConTRol and labEled imaging in the Same Shot (ACTRESS)" approach was designed to halve the scan time of ASL-based 4D-MRA by obtaining both labeled and control images in a single Look-Locker readout. However, application for vessel-selective labeling remains difficult. The aim of this study was to achieve a combination of ACTRESS and vessel-selective labeling to halve the scan time of vessel-selective 4D-MRA.

Methods: By Bloch equation simulations, Look-Locker pseudocontinuous-ASL (pCASL) was optimized to achieve constant static tissue signal across the multi-delay readout, which is essential for the ACTRESS approach. Additionally, a new subtraction scheme was proposed to achieve visualization of the inflow phase even when labeled blood will have already arrived in the distal arteries during the first phase acquisition due to the long duration of the pCASL labeling module. In vivo studies were performed to investigate the signal variation of the static tissue, as well as to assess image-quality of vessel-selective 4D-MRA with ACTRESS.

Results: In in vivo study, the mean signal variation of the static tissue was 8.98 % over the Look-Locker phases, thereby minimizing the elevation of background signal. This allowed visualization of peripheral arteries and slowly arriving arterial blood with image quality as good as conventional pCASL within half the acquisition time. Vessel-selective pCASL-ACTRESS enabled the separated visualization of vessels arising from internal and external carotid arteries within this shortened acquisition time.

Conclusion: By combining vessel-selective pCASL and ACTRESS approach, 4D-MRA of a single targeted arterial tree was achieved in a few minutes.

Introduction

Dynamic MRA (4D-MRA) using arterial spin labeling (ASL) provides several advantages over contrast-enhanced (CE) 4D-MRA in the brain. For example, vessel-selective imaging that exclusively visualizes the downstream arterial tree of an individually targeted artery, can be achieved by applying spatially-selective labeling pulses. Several previous studies report the usefulness of such vessel-selective MRA, e.g. for detecting the feeding arteries of an AVM (1,2). Also, ASL has a higher flexibility to achieve both high temporal and spatial resolution, because it is not limited to capture all necessary information during the first passage of a bolus of contrast agent. Therefore, ASL data acquisition can be repeated until sufficient information is acquired to achieve the desired spatial and temporal resolution. The scan time of ASL-based 4D-MRA will, however, be generally much longer than CE-4D-MRA, especially because ASL techniques require the acquisition of two image types, i.e. labeling and control conditions, which are generally acquired as separate acquisitions to subtract out the static tissue signal and isolate the ASL signal.

The recently proposed approach "Acquisition of ConTRol and labEled imaging in the Same Shot (ACTRESS)" was designed to shorten the scan time of non-vessel-selective ASL-based 4D-MRA by nearly a factor of two (3). In this approach, a single control image is acquired before applying the labeling pulse, which is followed by Look-Locker readouts (4) at multiple inversion-times (TI) after the labeling pulse (Figure 1 in (3)), which provide the labeled images. The subtraction is performed between all labeled images (2nd – Nth phase) and the single control image i.e. the first phase acquired before the labeling pulse. For this ACTRESS approach, one of the most important requirements to obtain similar image quality to conventional ASL-based 4D-MRA is to keep the signal intensity of the static tissue constant over all multi-TI readouts. This ensures that the signal from the static tissue will be effectively eliminated by subtraction. Variation of the static tissue signal over different TIs would result in elevated background signal after subtraction, which would weaken the contrast of the smaller peripheral arteries, especially in later phases. In the ACTRESS approach, constant signal over all different TIs is achieved by two essential elements of the sequence design: (i) the readout interval is kept constant to establish a steady-state of static tissue, and (ii) the effect of the labeling pulse (and any other pre-pulses) on the magnetization of the imaging volume is minimized, which would otherwise introduce unwanted signal changes over the Look-Locker readout.

The ACTRESS approach was optimized based on the pulsed ASL (PASL) technique. When considering this approach for vessel-selective imaging, however, some

difficulties are encountered. Firstly, for vessel-selective labeling by PASL a spatially-selective labeling slab is applied parallel to the target artery in the inferior-superior direction, i.e. as an approximately coronal or sagittal slab so that a large volume of the targeted arterial blood is labeled (5). Such a coronal/sagittal labeling slab will be perpendicular to the transverse imaging slices and the intersection of the labeling slab and the imaging volume will directly violate the above-mentioned second design element of the ACTRESS sequence. Pseudo-continuous ASL (pCASL) could therefore be an attractive option for the labeling module, because in pCASL the labeling of arterial blood is achieved by flow-driven pseudo-adiabatic inversion within a thin labeling plane perpendicular to the flow direction, i.e. parallel to the imaging volume. A spatially-varying pattern as needed for vessel-selective ASL can be achieved by applying additional in-plane gradients (6), while keeping the same parallel geometry of the labeling plane to the imaging volume. The use of pCASL labeling does therefore adhere to the second design-element. However, it violates the first design element of the ACTRESS approach: in pCASL a long train of labeling pulses is needed to generate enough labeled arterial blood. For the magnetization in the imaging volume, however, such a long period of labeling will act like a long recovery period, free from disturbances by RF pulses, thereby destroying the steady-state condition and introducing large signal changes of the static tissue during the Look-Locker readout.

In this article, we present how the ACTRESS approach can be combined with vessel-selective pCASL to achieve a fast acquisition sequence for vessel-selective 4D-MRA.

Methods

Optimization of the Static Tissue Signal

The concept for pCASL-ACTRESS is as follows. In pCASL large signal variations of the static tissue will occur over the Look-Locker readout due to longitudinal relaxation during the long pCASL labeling period, which will destroy the steady-state condition of the static tissue (Figure 1a). In order to minimize this signal variation, a pre-saturation pulse is applied before the labeling module (Figure 1b). The transition to the steady-state of the static tissue signal will subsequently be influenced by several parameters, such as the duration of the labeling train, the post-labeling delay (PLD), the number of excitation pulses per shot, their flip angle (FA), and repetition time (TR). Optimal behavior can be designed by means of Bloch equation simulation, although other criteria, such as the desired spatial and/or temporal resolution and the labeling duration, put additional constraints on these parameters. Bloch equation

simulation was performed, and a parameter setting that produces stable longitudinal magnetization behavior over Look-Locker readout was determined, (see section "In vivo healthy volunteer study" below). The T_1 of gray matter (GM), white matter (WM) and cerebrospinal fluid (CSF) were assumed to be 1200, 800 and 4300ms, respectively (7-9).

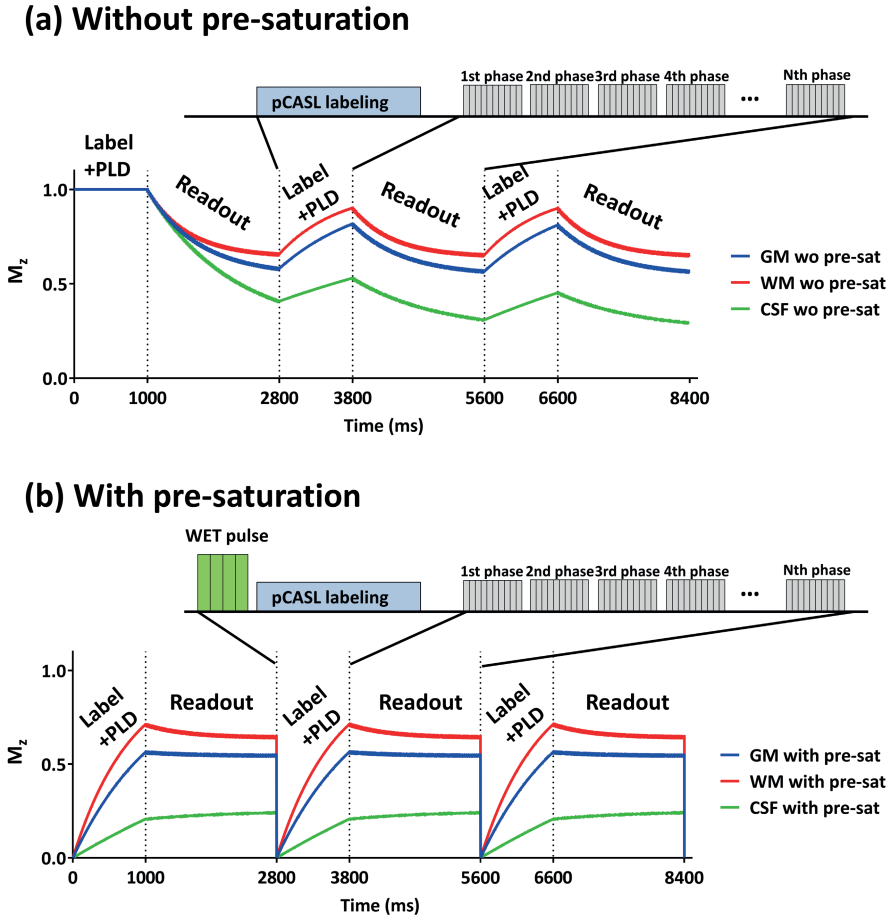


Figure 1: Simulated longitudinal magnetization (M_z) of the background static tissue as obtained by Bloch equation simulations. (a) Without a pre-saturation pulse before the pCASL labeling train, M_z varies considerably during Look-Locker multi-PLD readout. (b) By applying a pre-saturation pulse before the pCASL labeling train, variation of M_z during the readout becomes much smaller.

As input for the simulations, the readout-module should be defined. For this study, 3D turbo field echo planar imaging (TFEPI) was chosen as the readout-module, in which a segmented EPI readout is performed in between the excitation pulses of the TFE sequence. The number of k-lines acquired per EPI-train is referred to as "EPI-factor". The use of EPI helps to achieve fast acquisition as needed for the desired high temporal resolution, as well as to reduce the number of RF excitation pulses, which reduces the saturation of ASL signal and helps therefore to sustain sufficient SNR of the later Look-Locker phases.

In Vivo Healthy Volunteer Study

The in vivo study was approved by the local institutional review board and all volunteers provided written informed consent before inclusion into this study. A total of seven volunteers (male = 3, female = 4, mean age = 31.0 years [range, 19-45 years]) without known cerebrovascular disease participated in this study.

All MR scans were performed on a Philips 3.0T Ingenia scanner (Philips, Best, The Netherlands) using a 32-channel head coil. For pre-saturation of the static tissue, a WET module was employed (10). Following the results of the Bloch equation simulations, the pCASL labeling duration and PLD were set to 800 ms and 200 ms, respectively. A multi-phase Look-Locker readout with a multi-shot 3D-TFEPI sequence was used, in which 12 excitation pulses (including 2 start-up dummy echoes) were applied per phase after each ASL preparation, which were filled in the feet-head slice-encoding direction of the k-space. After each excitation pulse, 7 k-lines were filled by EPI-train (EPI-factor of 7) in the right-left phase-encoding direction, and TR was set to 15 ms. FA of 8° was used for the constant FA. Other imaging parameters were as follows: FOV = 220×176 mm, scan matrix = 176×176 reconstructed as 256×256 by zero-filling, 70 slices with thickness of 1.3 mm were acquired and reconstructed as 140 slices of 0.65 mm, Sensitivity-encoding (SENSE) factor = 2.3 in right-left direction and 1.2 in feet-head direction. A total of 10 Look-Locker phases were acquired with an interval of 180ms, which resulted in the duration of a single Look-Locker cycle (the interval between two WET pre-saturation modules) of 2800 ms. For all studies (described in the next paragraph), a conventional pCASL 4D-MRA protocol was used, which allowed the generation of pCASL-ACTRESS images as well as conventional pCASL 4D-MRA images from the same data set, providing a reference for comparison. The total scan time was 5:19 min. The conventional pCASL 4D-MRA was generated by a subtraction using both control and labeled images with the same PLD, which were acquired as separate Look-Locker readout cycles. To generate the pCASL-ACTRESS 4D-MRA, only the labeled images were used and a new subtraction scheme was proposed to generate 4D-MRA images

(see Figure 2 and the later section "Extended inflow-subtraction"), thereby representing an effective scan time of 2:40 min.

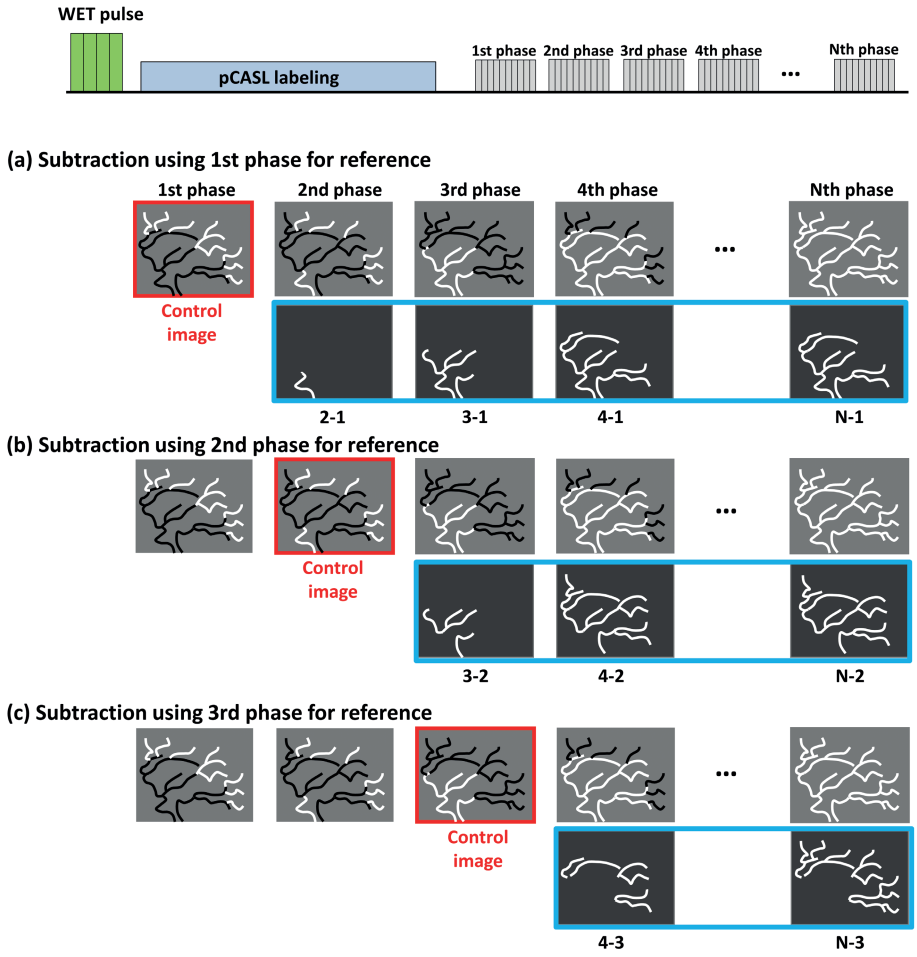


Figure 2: Basic sequence diagram of the pCASL-ACTRESS approach and proposed subtraction schemes. In subtraction (a), (b) and (c), respectively the 1st-phase, 2nd-phase and 3rd-phase are used as control image for subtraction. Using later phases for control image has two advantages: (i) slowly flowing labeled blood arriving later than the 1st-phase will still be visualized correctly by using a later phase as control image, and (ii) subtraction using neighboring phases will minimize differences in signal intensity of the background static tissue. The labeled and unlabeled blood are indicated in black and white, respectively.

The in vivo study consisted of three parts. Study-(i): to confirm the stability of the static tissue signal over the Look-Locker readout when using the above described parameters as optimized by Bloch equation simulations, non-selective pCASL 4D-MRA images were acquired from four volunteers, and the signal intensity of the static tissue was measured by ROI analysis (see section "ROI analysis"). Also, the pCASL-ACTRESS images were generated from these data, and qualitative comparisons of the image quality were performed between pCASL-ACTRESS and the conventional pCASL 4D-MRA (see section "Extended Inflow-Subtraction" and "Qualitative Comparison"). Study-(ii): vessel-selective labeling of the right and left internal carotid artery (ICA) was performed in four volunteers (three of these four volunteers were also part of Study-(i)). Study-(iii): separate visualization of arteries arising from the ICA and external carotid artery (ECA) was performed in two volunteers to demonstrate the clinical potential of this technique (e.g. visualization of bypass flow).

Vessel-Selective pCASL Labeling

Very recently we proposed an optimization of pCASL labeling parameters for vessel-selective labeling that modify the shape of the spatial modulation function of vessel-encoded pCASL to obtain (i) a sharp transition between the labeling and control conditions, and (ii) a broad and flat control region, to minimize the (partial) labeling of non-targeted arteries (16). In this study, one of the optimized settings in (16) with a maximum pCASL gradient strength (G_{max}) of 6.0 mT/m and mean gradient strength (G_{mean}) of 0.4 mT/m was used for selective labeling of the ICAs in Study-(ii). However, for separate labeling of ICA and ECA in Study-(iii), an even narrower labeling and a broader control condition was warranted and a G_{max} of 6.0 mT/m and G_{mean} of 0.2 mT/m were chosen. Other parameters for pCASL labeling were set as follows: pCASL labeling RF pulse duration of 0.5 ms, interval of 1.0 ms and flip angle of 21°. The shapes of the employed spatial modulation functions as obtained by Bloch equation simulations are shown in Figure 3.

Extended Inflow-Subtraction

Unlike for PASL labeling which employs a very short duration of the labeling module (approximately 10-20 ms), pCASL labeling relies on a much longer labeling module (800 ms in this study) and then labeled arterial blood will already have arrived in most of the arteries even when the first phase is acquired immediately after labeling has stopped. With a conventional subtraction approach between control and labeled images with identical PLD, only the outflow of labeled blood can be depicted, except for very slowly arriving arteries. To visualize the early inflow phase, "inflow-subtraction" was proposed previously (11,12), in which the 1st phase of the subtracted images is again subtracted by the subsequent phases. In ACTRESS approach, a similar inflow

visualization is obtained by subtracting the 1st phase of the labeled images from the subsequent phases (Figure 2a, in which the labeled and unlabeled blood are illustrated in black and white, respectively). With this method, however, only the labeled blood that is already present in the 1st phase (illustrated in black in Figure 2a) can be visualized. This means that slowly flowing peripheral arteries in which labeled blood has not arrived yet in the 1st phase (illustrated in white in Figure 2a) will not be visualized even though labeled blood would have reached these distal segments in the 2nd or later phases. To avoid this problem, additional inflow-subtractions were performed using the 2nd, 3rd and even later phases as reference (control) images (Figure 2b and 2c). It should be noted that the labeled images exhibit inflow of non-labeled blood (illustrated in white in Figure 2), whereas labeled blood exists in the control images (illustrated in black in Figure 2), which makes the subtraction order "labeled image – control image".

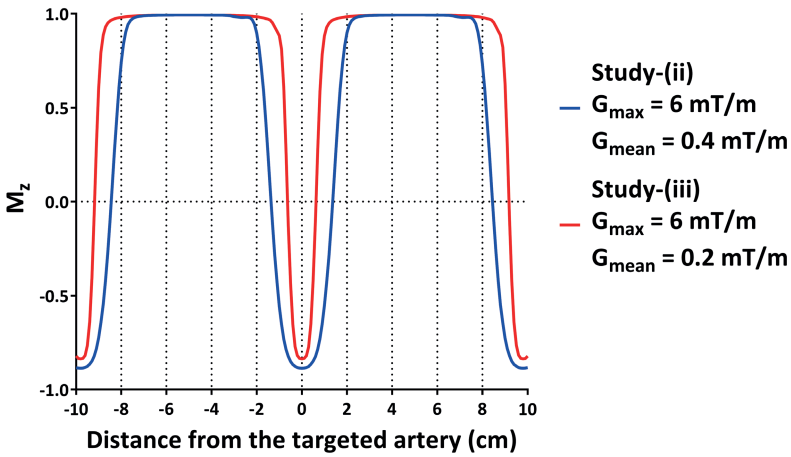


Figure 3: The shape of the spatial modulation employed in Study-(ii) and Study-(iii) as obtained by Bloch equation simulations. For Study-(ii), maximum pCASL gradient strength (G_{max}) of 6.0 mT/m and mean gradient strength (G_{mean}) of 0.4 mT/m were used. For Study-(iii), G_{max} of 6.0 mT/m and G_{mean} of 0.2 mT/m were used to obtain an even narrower labeling condition (and therefore a broader control condition). Other parameters for pCASL labeling were set as follows: pCASL labeling RF pulse duration of 0.5 ms, interval of 1.0 ms and flip angle of 21°.

ROI Analysis

In order to assess the stability of the static tissue signal, the conventional subtraction (control minus labeled images with identical PLD) was performed using the pCASL 4D-MRA data acquired in Study-(i), and a temporal maximum intensity projection (MIP) across all phases (i.e. not the spatial direction) was produced for each slice. An

ROI was manually drawn within the background static tissue on the 20th, 40th, 60th, 80th, 100th and 120th slices avoiding obvious arteries and artefacts. These six ROIs were copied to the original non-subtracted, non-MIP images and the mean signal intensity was obtained as a function of PLD.

Qualitative Comparisons

Spatial MIP images were generated in sagittal and transverse directions using the conventionally subtracted non-selective pCASL 4D-MRA images as well as using the pCASL-ACTRESS images as obtained by the extended inflow-subtraction scheme described above. With these MIP images, qualitative comparisons between the conventional pCASL and pCASL-ACTRESS were performed by a board-certified neuroradiologist with 13 years of experience (N. F.) with respect to the existence of artifacts and/or major differences of vessel visualization as compared to the reference (conventional pCASL) images. Moreover, the depiction of the peripheral arteries was scored by means of a relative scoring system: 3 = same or very similar depiction as the reference, 2 = slightly poorer depiction, 1 = obviously poorer depiction.

Additionally, the maximum length of the occipital artery that was depicted on both pCASL-ACTRESS and the conventional pCASL was measured. The occipital artery was chosen as a representative artery with slow flow. For this measurement MIPs with limited thickness of 50 mm (partial MIP) were generated in the coronal direction by centering on either the left or the right occipital artery to avoid over-projection of other arteries.

Results

Figure 1 shows the simulated longitudinal magnetization (M_z) of GM, WM and CSF over the labeling, PLD and Look-Locker readout as obtained by Bloch equation simulations. With the parameters stated in the methods section for the in vivo study, the M_z variation (defined as the difference between the maximum and minimum M_z over the Look-Locker readout: ΔM_z) of GM, WM and CSF were 0.023, 0.073 and 0.036 with a pre-saturation pulse (Figure 1a), which were remarkably lower than ΔM_z of 0.250, 0.253 and 0.152 obtained without applying a pre-saturation pulse (Figure 1b). Additionally, Figure 4 shows ΔM_z obtained over a range of T_1 values from 100 ms to 4300 ms in steps of 100 ms, with and without a pre-saturation puse. By applying a pre-saturation pulse, ΔM_z was kept lower than 0.1 for T_1 value of 700 ms and longer. Also from the ROI analysis performed on the in vivo images, it was confirmed that the normalized variation of the mean signal intensity of static tissue was 8.98 %.

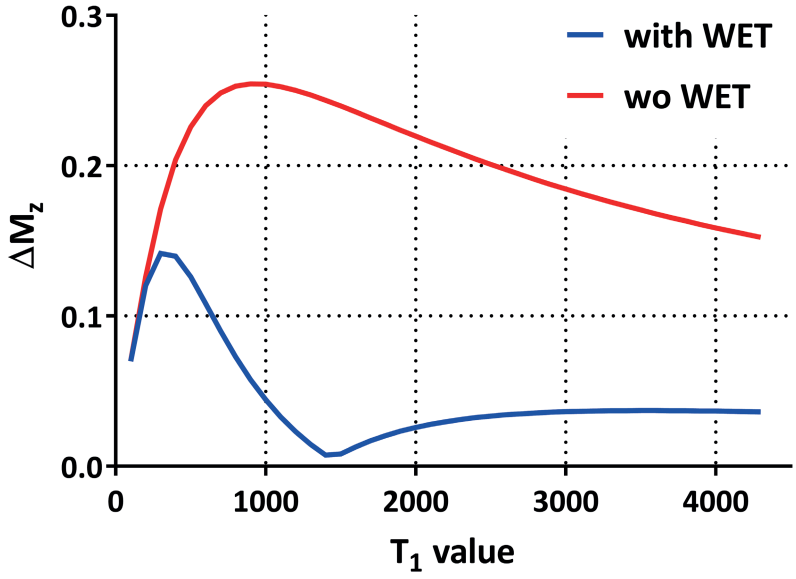


Figure 4: ΔM_z (the M_z variation defined as the difference between the maximum and minimum M_z over the Look-Locker readout) obtained over a range of T_1 values from 100 ms to 4300 ms in steps of 100 ms.

The representative images of the early inflow-phases and the last peripheral-phase as obtained by the extended inflow-subtraction scheme are shown in Figure 5 and 6, respectively. By using a later phase as control image for subtraction, slowly arriving arterial blood such as those in the occipital artery were better visualized (as indicated by arrows in Figure 6). A slight elevation of background signal was observed in pCASL-ACTRESS as compared with the conventional approach, including signal within the superior sagittal sinus as indicated in the observer study (see next paragraph and also Figure 7 and 8). However, visualization of distal arteries was not hindered for any case. Figure 9 shows representative images of vessel-selective pCASL-ACTRESS 4D-MRA from study-(ii), in which the spatially selective labeling was performed targeting either the right or left ICA aiming at differentiating between these two vessels and the posterior circulation. However, this study-(ii) resulted in ambiguous labeling for the ECA. Therefore, separate labeling between the ECA and ICA of the same hemisphere was attempted in two additional volunteers, from which one example is shown in Figure 10. These results show the potential of this approach for visualization of e.g. a bypass artery.

In the observer study, it was found that the venous blood in the superior sagittal sinus was erroneously visualized in all pCASL-ACTRESS 4D-MRA, whereas none of the conventional pCASL depicted the superior sagittal sinus. We refer to the discussion for possible causes of this artefact. No other artefacts or major differences of vessel visualization were observed as compared to conventional pCASL 4D-MRA. With regard to the depiction of peripheral arteries, all four images resulted in score = 3 (i.e. "same or very similar depiction as the reference"). As shown in Table 1, however, a 23.2% shorter depiction-length of the occipital artery was found by pCASL-ACTRESS as compared to the conventional pCASL 4D-MRA. The PLD of images with the maximum depiction of occipital artery (which were used to measure the maximum length) ranged from 1100 to 1820 ms (mean value of 1302.5 ms).

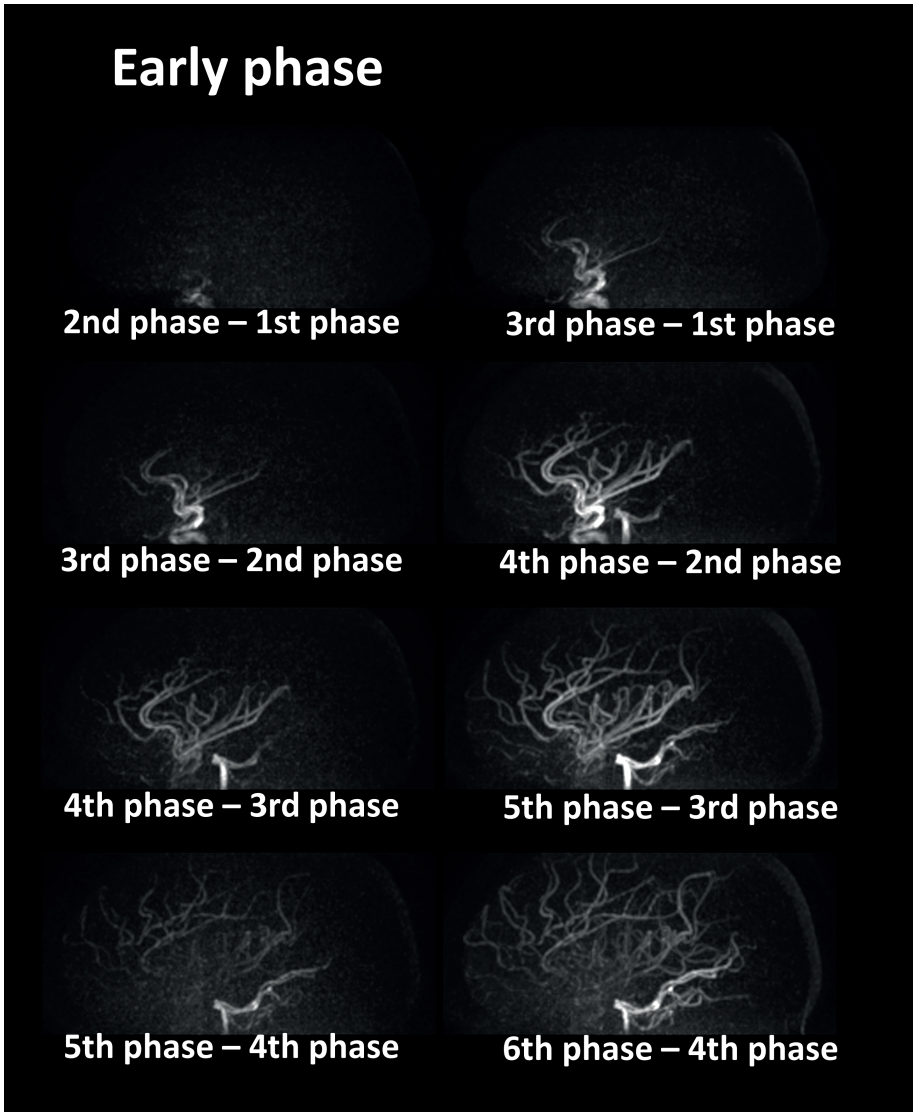


Figure 5: Representative images of the early inflow-phases as obtained by the proposed subtraction schemes illustrated in Figure 2.

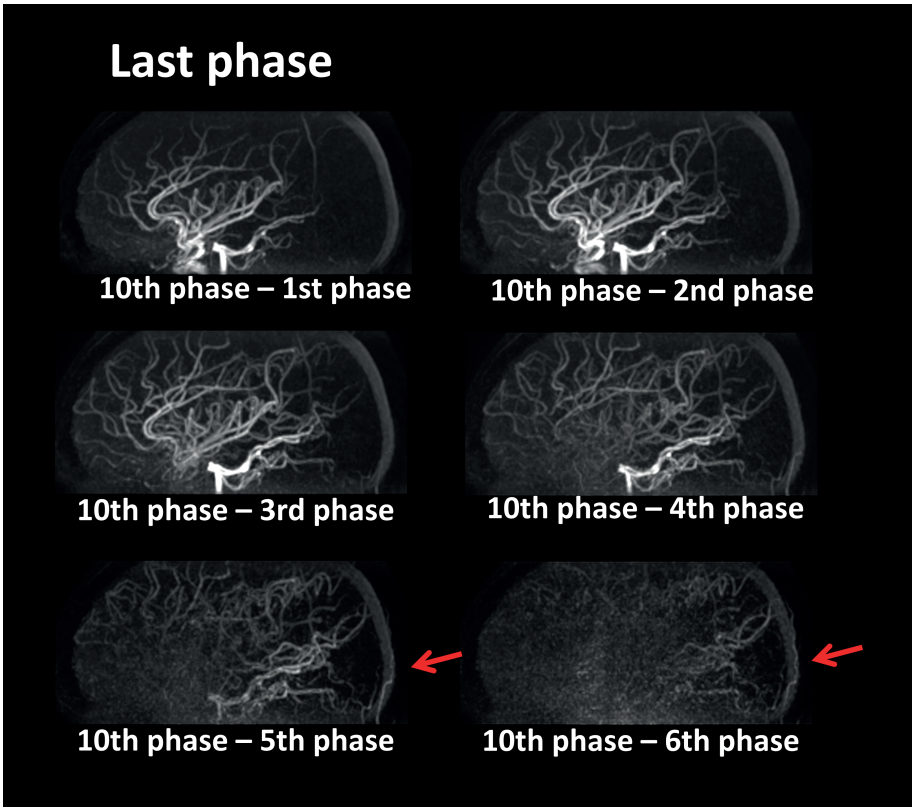


Figure-6: Representative images of the last peripheral-phases as obtained by the proposed subtraction schemes illustrated in Figure 2. Slow blood flow in arteries such as the occipital artery are also well visualized (indicated by arrows)

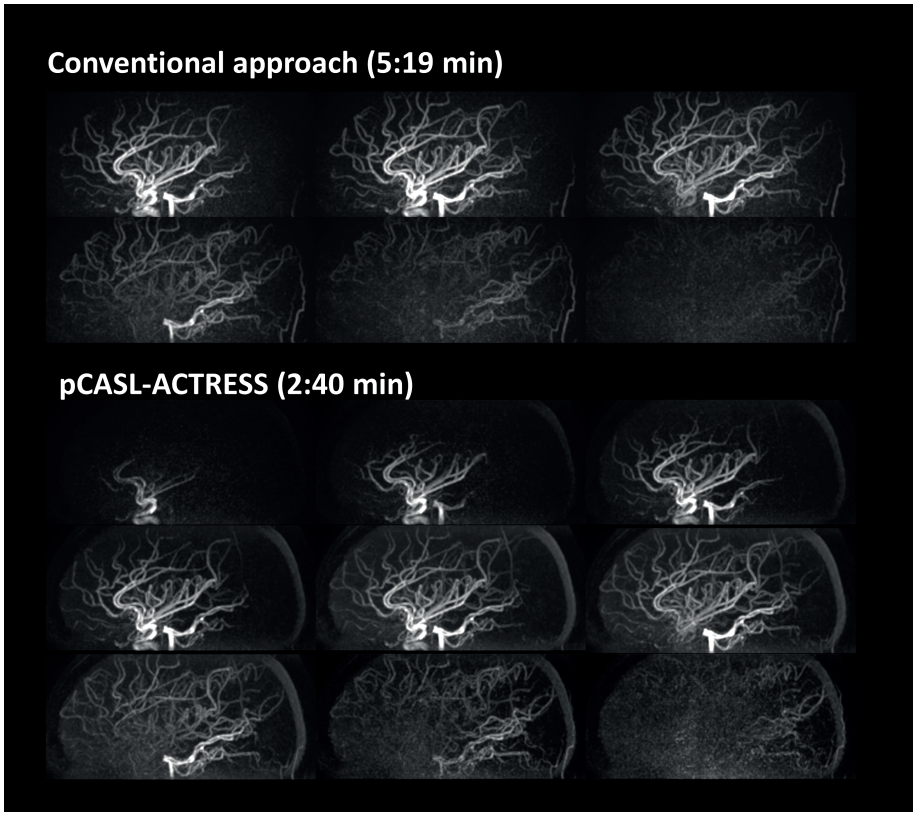


Figure 7: Comparison of images acquired by the pCASL-ACTRESS approach (scan time of 2:40 min) and conventional approach (5:19 min).

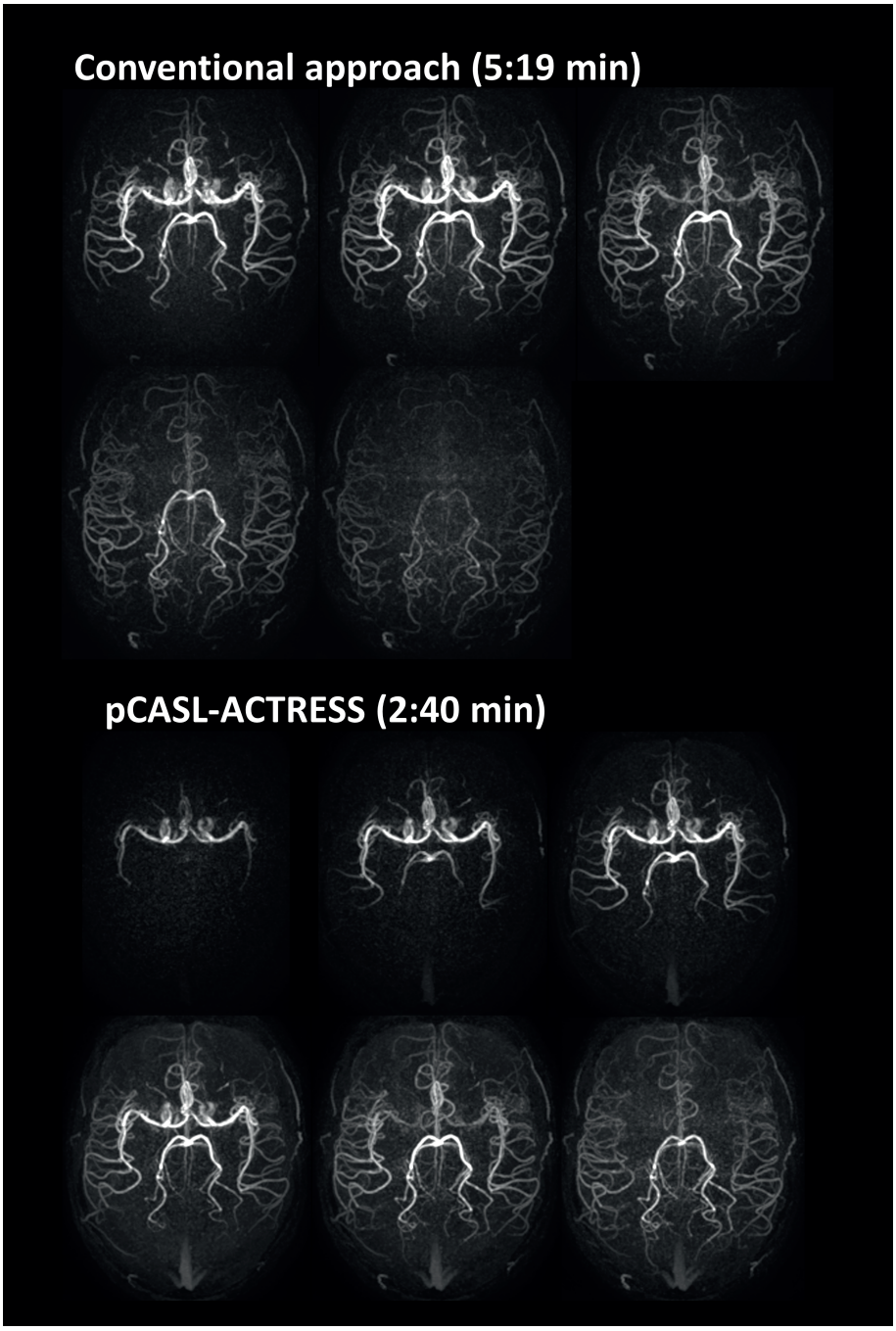


Figure 8: Comparison of images acquired by the pCASL-ACTRESS approach (scan time of 2:40 min) and conventional approach (5:19 min).

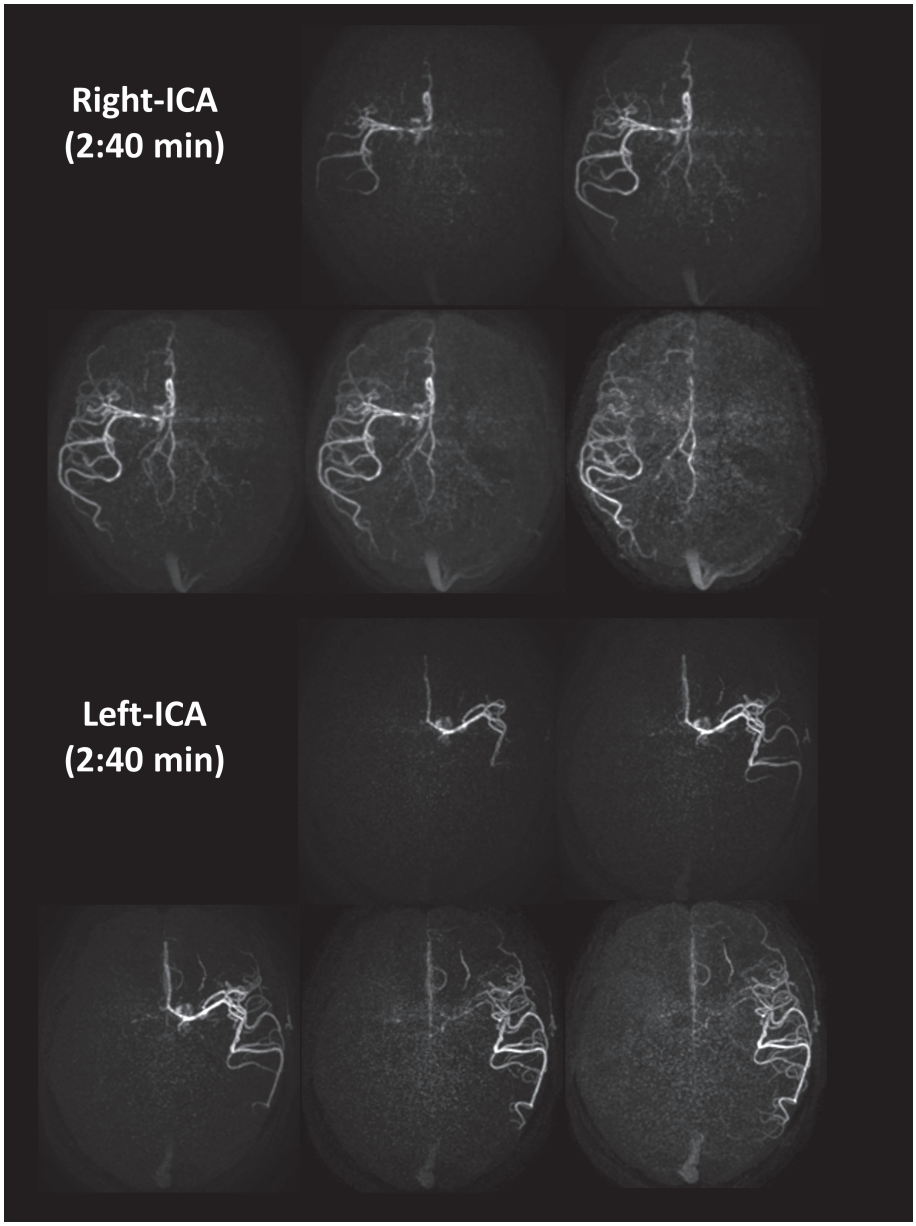


Figure 9: Representative images of vessel-selective 4D-MRA obtained by pCASL-ACTRESS approach (scan time of 2:40 min per artery), in which either the right or left internal carotid artery (ICA) was labeled.

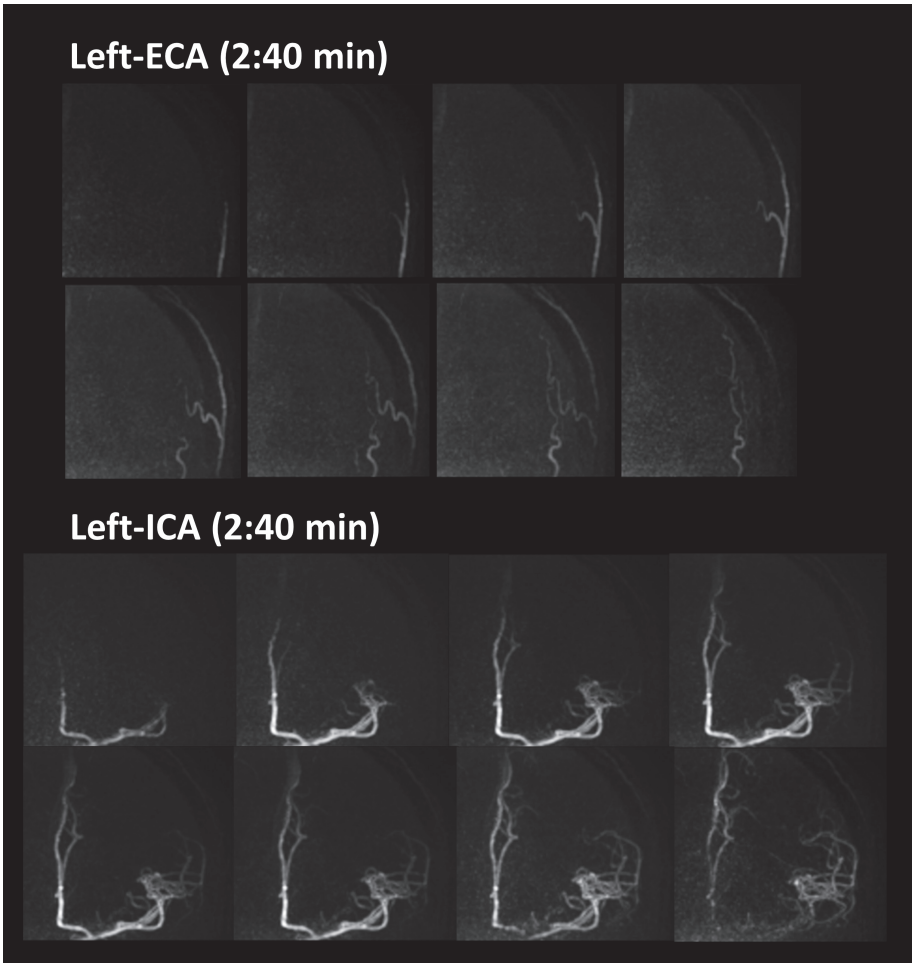


Figure 10: An example that illustrates the selective visualization of the external carotid artery (ECA) and internal carotid artery (ICA) as obtained by the pCASL-ACTRESS approach (scan time of 2:40 min per artery).

Table 1: Maximum length of occipital artery measured on pCASL-ACTRESS and the conventional pCASL

Subject	Target artery	ACTRESS (mm)	pCASL (mm)	Percentage (ACTRESS/pCASL)	PLD for maximum depiction (ms)
1	Right OA	41.82	50.20	83.3%	1100
	Left OA	26.49	38.16	69.4%	
2	Right OA	64.54	72.13	89.5%	1280
	Left OA	40.47	46.21	87.6%	
3	Right OA	28.11	39.50	71.2%	1280
	Left OA	53.2	74.22	71.7%	
4	Right OA	35.88	50.65	70.8%	1280
	Left OA	73.87	104.54	70.7%	1820

Discussion

In this manuscript we have presented a novel vessel-selective 4D-MRA acquisition which combines vessel-selective pCASL with the ACTRESS acceleration approach (3). In the original ACTRESS approach based upon PASL for labeling, the application of vessel-selective labeling was hampered by elevated background signal as a result of the disturbance of the equilibrium magnetization of the static tissue arising from the intersection of the labeling slab with the imaging slices. By using pCASL for labeling, in which the labeling pulses are applied approximately parallel to the imaging slices and therefore do not interfere with the magnetization in the imaging slices, the combination of vessel-selective labeling and ACTRESS acceleration became possible. Although the long labeling module as used in pCASL sequence destroys the steady-state of the magnetization by interrupting the continuous series of excitation pulses of the Look-Locker TFEPI readout, thereby causing elevated background signal in the subtracted images, this could successfully be minimized by optimization of the relevant parameters, especially by inserting a pre-saturation pulse before the labeling module. The in vivo study proved that this approach allowed vessel specific 4D-MRA in half of the scan time required for conventional ASL-based acquisitions.

In this study we also proposed the use of vessel-selective pCASL with an optimized spatial labeling profile (16). Although it is a rectangular-like inversion band, which has the spatial selectivity only in a single in-plane direction, it enables a sharp transition between the labeling and control conditions as well as the optimized thin labeling band, thereby allowing enough freedom to label only a targeted artery. Moreover, broad and flat control condition is achieved without affecting the magnetization, which is essential to the ACTRESS approach. Super-selective pCASL labeling based upon rotating in-plane gradients achieves a circular labeling spot (13,14), which would enable more focused labeling than the inversion band used in this study. However, residual influence on the magnetization outside of the target region was observed (15). This could produce partial saturation of the magnetization in untargeted arteries, which would in traditional pCASL 4D-MRA not be a problem, because such an unwanted influence to the magnetization would be canceled out by means of the paired subtraction from the control image acquired with the same rotating gradients. When using the ACTRESS approach, however, such partial saturation will result in inclusion of the downstream vasculature in the generated 4D-MRA, because the subtraction is performed between labeled images with a different PLD. Therefore, it is important to optimize the spatial modulation function of the longitudinal magnetization itself, and it is no longer sufficient to optimize the relative labeling efficiency, i.e the difference between the labeling and control condition. A downside of this approach is that

effective labeling is achieved in a rectangular region, which requires more careful planning to avoid inclusion of other arteries within the labeling plane.

In vessel-encoded pCASL (ve-pCASL) as proposed by Wong (6), vessel-selective labeling is performed by a Hadamard-encoding scheme, enabling the selective depiction of several arteries. For perfusion imaging, this Hadamard-encoding can be performed as a replacement for averaging, and the territorial perfusion images can be obtained without time penalty. For 4D-MRA acquisitions, however, all the scan time needs to be invested in the acquisition of the k-lines needed for high spatial resolution, which leaves no scan time available to acquire multiple averages. Therefore, acquiring more Hadamard-encodings for ve-pCASL would directly result in a longer scan time for the complete 4D-MRA acquisition. Time-efficient acquisition of ve-pCASL 4D-MRA has been proposed previously (16), based upon four Hadamard-encodings thereby separating three arteries (right ICA, left ICA and both vertebral arteries together), but this still results in a twice as long acquisition time as compared to a non-selective acquisition. Moreover, if separate visualization of the ECA or a bypass artery would be of interest, the number of Hadamard-encodings would need to be increased even more, which again would result in an increase in scan time. By using the pCASL-ACTRESS approach, selective visualization of a single target artery can be obtained in 2 – 3 minutes at a resolution of 1.25×1.25×1.3 mm, which can be, furthermore, flexibly applied only for a single or few arteries of interest, i.e. in a one-by-one fashion.

With the original inflow-subtraction approach (11,12), peripheral arteries exhibiting slow flow in which the labeled blood will only arrive after the first readout would not be visualized. To avoid such missed visualization of peripheral arteries, one solution would be to increase the duration of the pCASL labeling ensuring that labeled blood has arrived in the complete arterial vasculature before the first phase is acquired. However, this would result in proportionally longer scan times and in a patient with slow flow, even longer label duration would need to be selected. In this study, subtraction was performed between all different combinations of PLDs (see Figure 2) to solve this issue. The proposed subtraction scheme was proven to also visualize arteries with late arrival, such as the occipital artery.

In the original ACTRESS approach using PASL, it is very important that the control image acquired in the first phase of the Look-Locker readout does not contain the residual labeled blood from the previous Look-Locker readout cycle (3). Although it is also true for pCASL-ACTRESS, such a carryover of the labeled blood to the next Look-Locker cycle is unlikely to happen in pCASL-ACTRESS because the WET pre-saturation

module applied before the pCASL labeling cancels the residual labeling remaining within the imaging volume. In this study, 4D-MRA using the true pCASL-ACTRESS approach was not acquired separately in *in-vivo* studies due to restricted examination time. Instead, as written in Methods section, pCASL-ACTRESS 4D-MRA was generated from the conventional pCASL data by using only the labeled Look-Locker cycle. Considering above-mentioned difference between the original ACTRESS using PASL and pCASL-ACTRESS, however, such a time-efficient way of comparison is presumed not to cause a biased estimation of the effect of the residual labeling.

There are several limitations that should be mentioned in this study. Firstly, the parameter optimization was performed for pCASL-ACTRESS approach to stabilize the static tissue signal. Therefore, the optimized parameters might not be the best parameters for the conventional pCASL (non-ACTRESS) images, e.g. FA of 10° could provide higher signal intensity of arteries than FA of 8° as used in this study. Secondly, the combination of parameters are not very flexible when using ACTRESS approach. For example, when a conventional gradient echo sequence is used for the readout instead of the proposed TFEPI sequence, the TR would be shorter and more excitations would be employed after each ASL preparation to compensate for the absence of EPI (e.g. TR of 4 ms with 44 excitations for the same phase interval of 180 ms). This would result in a different equilibrium-state, and lower FA and/or shorter pCASL labeling duration and PLD would be required to achieve the stability of the static tissue signal, which result in lower SNR. The third limitation is that we only tested our optimized settings in seven healthy volunteers. In patient examinations, there could be pathology with shortened T_1 value, such as a hemorrhage with presence of methemoglobin. As Figure 4 shows, M_z variation over the Look-Locker readout would be larger for certain range of short T_1 values, which could cause residual signal after subtraction. For clinical examination, therefore, further investigation and optimization are required, especially to study whether such signal from lesions would affect diagnosis. Lastly, an increase of the background signal was observed in pCASL-ACTRESS, of which especially venous signal in the sagittal sinus was most noticeable. A plausible explanation for the enhanced venous signal would be the presence of slowly inflowing venous blood from outside of the imaging volume during the Look-Locker readout. Such venous blood would experience longer time to recover from the pre-saturation pulse and fewer excitation pulses, and therefore the M_z would be less saturated than other spins that have been staying within the imaging volume throughout the entire Look-Locker readout. This difference introduces a gradual increase of M_z within the sagittal sinus over the Look-Locker readout, thereby causing the enhanced visualization. We also attribute the weaker depiction of the occipital artery as found in the observer study to the slightly elevated background signal from static tissue. However, as shown in the

example images, these limitations would not impede many clinical applications.

Conclusion

In summary, we have presented an accelerated acquisition of vessel-selective 4D-MRA by combining vessel-selective pCASL with the ACTRESS approach. By using vessel-selective pCASL labeling, signal elevation of the background signal caused by intersection of the labeling slab and the imaging volume could be avoided. Application of a pre-saturation pulse and the use of optimized parameter settings minimized static tissue signal variations over the Look-Locker readout, thereby minimizing subtraction errors. This approach allowed vessel specific visualization of the arterial vasculature in half of the scan-time required for a conventional ASL-based 4D-MRA acquisition.

Acknowledgements

This research was supported by the EU under the Horizon2020 program (project: CDS-QUAMRI, Project number 634541). TO is funded by the UK Royal Academy of Engineering. The Wellcome Centre for Integrative Neuroimaging is supported by core funding from the Wellcome Trust (203139/Z/16/Z).

References

1. Fujima N, Osanai T, Shimizu Y, Yoshida A, Harada T, Nakayama N, Kudo K, Houkin K, Shirato H. Utility of noncontrast-enhanced time-resolved four-dimensional MR angiography with a vessel-selective technique for intracranial arteriovenous malformations. J Magn Reson Imaging 2016;44(4):834-845.
2. Jensen-Kondering U, Lindner T, van Osch MJ, Rohr A, Jansen O, Helle M. Superselective pseudo-continuous arterial spin labeling angiography. Eur J Radiol 2015;84(9):1758-1767.
3. Suzuki Y, Fujima N, Ogino T, Meakin JA, Suwa A, Sugimori H, Van Cauteren M, van Osch MJP. Acceleration of ASL-based time-resolved MR angiography by acquisition of control and labeled images in the same shot (ACTRESS). Magn Reson Med 2018;79(1):224-233.
4. Gunther M, Bock M, Schad LR. Arterial spin labeling in combination with a look-locker sampling strategy: inflow turbo-sampling EPI-FAIR (ITS-FAIR). Magn Reson Med 2001;46(5):974-984.
5. Golay X, Petersen ET, Hui F. Pulsed star labeling of arterial regions (PULSAR): a robust regional perfusion technique for high field imaging. Magn Reson Med 2005;53(1):15-21.
6. Wong EC. Vessel-encoded arterial spin-labeling using pseudocontinuous tagging. Magnetic Resonance in Medicine 2007;58(6):1086-1091.
7. Rydhog AS, van Osch MJ, Lindgren E, Nilsson M, Latt J, Stahlberg F, Wirestam R, Knutsson L. Intravoxel incoherent motion (IVIM) imaging at different magnetic field strengths: what is feasible? Magn Reson Imaging 2014;32(10):1247-1258.
8. Lu H, Nagae-Poetscher LM, Golay X, Lin D, Pomper M, van Zijl PC. Routine clinical brain MRI sequences for use at 3.0 Tesla. J Magn Reson Imaging 2005;22(1):13-22.
9. Rooney WD, Johnson G, Li X, Cohen ER, Kim SG, Ugurbil K, Springer CS, Jr. Magnetic field and tissue dependencies of human brain longitudinal 1H2O relaxation in vivo. Magn Reson Med 2007;57(2):308-318.
10. Ogg RJ, Kingsley PB, Taylor JS. WET, a T1- and B1-insensitive water-suppression method for in vivo localized 1H NMR spectroscopy. J Magn Reson B 1994;104(1):1-10.
11. Okell TW, Schmitt P, Bi X, Chappell MA, Tijssen RH, Sheerin F, Miller KL, Jezzard P. Optimization of 4D vessel-selective arterial spin labeling angiography using balanced steady-state free precession and vessel-encoding. NMR Biomed 2016;29(6):776-786.
12. Kopeinigg D, Bammer R. Time-resolved angiography using inflow subtraction (TRAILS). Magn Reson Med 2014;72(3):669-678.
13. Helle M, Norris DG, Rufer S, Alfke K, Jansen O, van Osch MJ. Superselective pseudocontinuous arterial spin labeling. Magn Reson Med 2010;64(3):777-786.
14. Dai W, Robson PM, Shankaranarayanan A, Alsop DC. Modified pulsed continuous arterial spin labeling for labeling of a single artery. Magn Reson Med 2010;64(4):975-982.
15. Lindner T, Larsen N, Jansen O, Helle M. Accelerated visualization of selected intracranial arteries by cycled super-selective arterial spin labeling. MAGMA 2016;29(6):843-852.
16. Suzuki Y, van Osch MJP, Fujima N, Okell TW. Optimization of the Spatial Modulation Function of Vessel-Encoded Pseudo-Continuous ASL and its Application to Dynamic Angiography. Magn Reson Med 2018;00:1-13. https://doi.org/10.1002/mrm.27418

Chapter 5

Simultaneous Acquisition of Perfusion Image and Dynamic Angiography Using Time-Encoded Pseudo-Continuous ASL

Magn Reson Med 2018; 79 (5): 2676-2684

Yuriko Suzuki
Michael Helle
Peter Koken
Marc Van Cauteren
Matthias J. P. van Osch

Abstract

Purpose: Both dynamic MRA (4D-MRA) and perfusion imaging can be acquired by using arterial spin labeling (ASL). While 4D-MRA highlights large vessel pathology, such as stenosis or collateral blood flow patterns, perfusion imaging provides information on the microvascular status. Therefore, a complete picture of the cerebral hemodynamic condition could be obtained by combining the two techniques. Here, we propose a novel technique for simultaneous acquisition of 4D-MRA and perfusion imaging using time-encoded pseudo-continuous ASL (te-pCASL).

Methods: The te-pCASL labeling module consisted of a first subbolus that was optimized for perfusion imaging by using a labeling duration of 1800 ms, whereas the other six subboli of 130 ms were used for encoding the passage of the labeled spins through the arterial system for 4D-MRA acquisition. After the entire labeling module, a multi-shot 3D turbo field echo planar imaging (TFEPI) readout was executed for the 4D-MRA acquisition, immediately followed by a single-shot, multi-slice EPI readout for perfusion imaging. The optimal excitation flip angle for the 3D-TFEPI readout was investigated by evaluating the image quality of the 4D-MRA and perfusion images as well as the accuracy of the estimated cerebral blood flow (CBF) values.

Results: When using 36 excitation radiofrequency pulses with flip angles of 5 or 7.5°, saturation effects of the 3D-TFEPI readout on the perfusion images were relatively moderate and after correction, there were no statistically significant differences between the obtained CBF values and those from traditional pCASL.

Conclusion: This study demonstrated that simultaneous acquisition of 4D-MRA and perfusion images can be achieved by using te-pCASL.

Introduction

For assessment of the hemodynamic condition of the brain, both visualization of the arterial pathways as well as obtaining microvascular information are essential. The former can be achieved by MR angiography (MRA) and dynamic MRA, which depict blood flow patterns as well as macrovascular pathology, such as artery stenosis. The latter can be assessed by measuring the cerebral blood flow (CBF) with perfusion MRI, thereby providing information on the delivery of oxygen and nutrients to the brain tissue. Both imaging techniques provide complementary information, and their combination contributes to a full picture of the hemodynamic status of the brain.

Arterial spin labeling (ASL) techniques are used both for non-contrast 4D-MRA (1-4) as well as for perfusion imaging. Because both imaging modalities are based upon a similar ASL preparation module, a combined acquisition seems feasible. Conveniently, the timing of interest after the labeling of arterial blood is different for 4D-MRA and perfusion imaging. In perfusion imaging, a long post-labeling delay (PLD) of 1.6 – 2.0 seconds is required, so that all labeled blood has arrived in the brain tissue and no signal arises from within the arterial vessels (5,6). In contrast, in 4D-MRA, acquisition usually starts immediately after the labeling and is repeated multiple times to depict the passage of the labeled blood through the arterial tree. Therefore, acquisition of 4D-MRA could fit perfectly within the PLD of perfusion imaging. However, there are two main challenges standing in the way of such an implementation. First, the current recommended implementation of ASL for clinical perfusion imaging is pseudo-continuous ASL (pCASL) with a labeling duration of approximately 1.8 seconds, as a result of its ease of implementation and the high signal-to-noise ratio (SNR) (5). For 4D-MRA, however, such a long labeling duration would spoil the ability to depict the early phase of passage through the arterial system. Therefore, pCASL with a much shorter labeling duration, or pulsed ASL (PASL) techniques, are currently the preferred labeling options for 4D-MRA. The second challenge is that the long series of excitation pulses of the commonly used Look-Locker readout for multi-PLD acquisition (7) would consume too much of the longitudinal magnetization of labeled blood, thereby severely affecting the SNR of perfusion images acquired afterwards.

We propose the use of time-encoded pCASL (te-pCASL) as a solution to both of these mentioned challenges (8,9). Unlike the Look-Locker approach, te-pCASL enables acquisition of dynamic images with multiple PLDs without repeating the readout module. Instead, the long pCASL labeling is encoded according to, for example, the Hadamard matrix [Fig.1 in (8)], from which multiple images with different PLDs can be reconstructed by applying a decoding process. Previously, this technique has been

used for generating arterial transit time maps as well as perfusion images with high SNR from a single sequence (10,11).

In this article, we present a novel technique for simultaneous acquisition of 4D-MRA and perfusion images using te-pCASL. Part of this study was previously presented in abstract format (12).

Methods

Implementation of the Simultaneous Acquisition Scheme

In te-pCASL, image acquisition with multiple PLDs (e.g. N) is achieved by dividing a long pCASL labeling module into N segments and by changing the condition (label or control) of each segment over N+1 repeated acquisitions according to, for example, a Hadamard matrix of order N+1 [Fig.1 in (8)]. By using an appropriate decoding step, N ASL images can be reconstructed, in which only the labeling from a single segment, also known as subbolus, will contribute to the signal of each ASL image. Each ASL image will therefore have a unique combination of labeling duration and PLD.

The two challenges that were mentioned previously can be solved by use of te-pCASL. First, it is possible to assign different labeling duration to each subbolus, so that sufficiently long labeling duration is used for perfusion imaging, while using a short labeling duration at multiple PLDs for 4D-MRA. Second, because the temporal information is already encoded during labeling, only a single-phase readout module is needed to generate multi-phase images, unlike the commonly used Look-Locker readout that relies on multiple repetitions of the readout module. This means that only a single readout module is needed for 4D-MRA acquisition, thereby reducing the number of radiofrequency (RF) excitation pulses and thus preserving most of the encoded longitudinal magnetization for acquisition of the perfusion image.

Figure 1 shows the sequence design as used in this study. The encoding scheme of the pCASL labeling module was based on a Hadamard matrix of order eight. The first subbolus (subbolus 1) was optimized for perfusion imaging, and therefore the duration was set to 1800 ms. The other six subboli (subboli 2 – 7) were optimized for 4D-MRA acquisition, with their duration set to 130 ms. There is a pause of 100 ms between the 1st and 2nd subbolus to allow application of a background suppression pulse as well as to allow a sufficiently long PLD for perfusion imaging. After the entire labeling module, a multi-shot 3D turbo field echo planar imaging (TFEPI) readout (13,14) is executed with high spatial resolution for the 4D-MRA data acquisition,

which is directly followed by a single-shot, multi-slice EPI readout with low resolution for perfusion imaging by using the interleaved scanning approach as described previously (15). In the TFEPI sequence, an EPI readout is performed in between excitation pulses of TFE sequence, which helps to reduce the number of RF excitation pulses further, (i.e. by a factor of number of acquired k-lines after a single excitation pulse (EPI factor)), thereby further preserving longitudinal magnetization for perfusion imaging. Between the 4D-MRA and perfusion imaging readout, a second background suppression pulse was applied. For both background suppression pulses, Frequency Offset Corrected Inversion (FOCI) pulse (16) was used to achieve a sharper spatial inversion profile than conventional hyperbolic-secant pulses, thereby limiting the effect of the background suppression pulses on fresh blood approaching the labeling plane for subsequent subboli.

In Vivo Healthy Volunteer Study

The study was approved by the local institutional review board, and all volunteers provided written informed consent before inclusion into this study. A total of six volunteers (male = 4, female = 2, mean age = 39 years [range, 21-58 years]) without known cerebrovascular disease participated in the study.

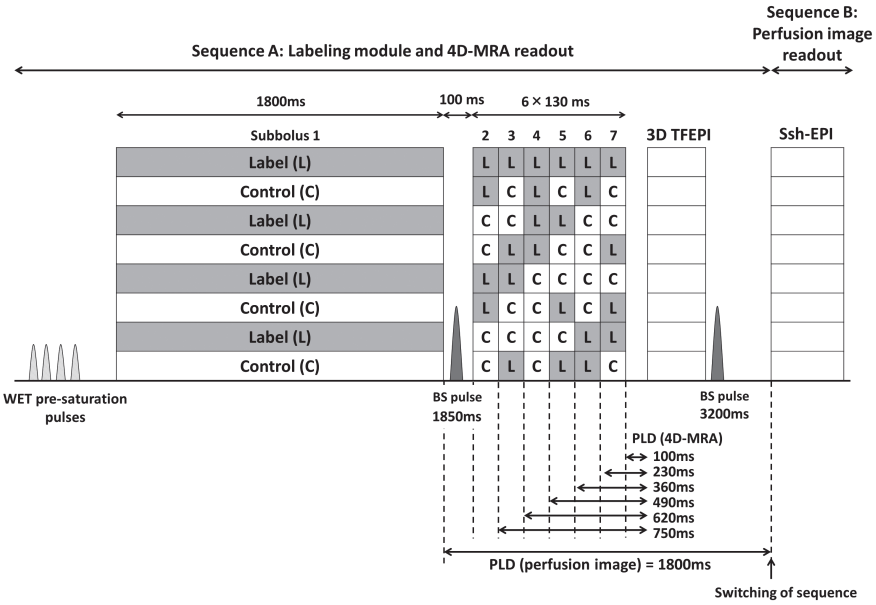


Figure 1: Sequence diagram of the simultaneous acquisition of 4D-MRA and perfusion imaging using time-encoded pCASL. Optimal timing of two background suppression pulses was obtained by simulations based upon the Bloch equation.

The reduction of the labeled magnetization caused by the readout of 4D-MRA will be referred to as *saturation effects* throughout this paper. To find the optimal excitation flip angle for 4D-MRA that provides a compromise between sufficient signal for the 4D-MRA and acceptable saturation effects to obtain perfusion images with sufficient quality, the flip angle of the 4D-MRA readout was varied (5, 7.5, 10, 12.5 and 15°), while keeping the parameters for perfusion imaging unchanged.

Optimal timing of background suppression pulses were obtained by Bloch equation simulations in MATLAB (Mathworks, Natick, MA, USA), taking into account the effects from both the prelabeling saturation pulse and the excitation pulses of the 4D-MRA acquisition, assuming that all transverse magnetization is spoiled before the next excitation pulse is applied. T_1 value for gray matter (GM), white matter (WM) and cerebrospinal fluid (CSF) were assumed to be 1200, 800 and 4300 ms, respectively (17-19). The same timings were used for all sequences independent of the used flip angle of the TFE readout, to keep sequences as comparable as possible. Criteria for optimal background suppression were that all longitudinal magnetization of GM, WM and CSF should be minimal (albeit above zero) for all flip angles at the moment of the acquisition of the first slice from the multi-slice 2D perfusion readout. Furthermore, the number of background suppression pulses was set to two, as a compromise between the level of background suppression and loss of label as a result of the inclusion of inversion pulses (5).

All MR scans were performed on a Philips 3.0T Achieva-TX scanner (Philips, Best, The Netherlands) using a 32-channel head coil. For 4D-MRA, a multi-shot 3D-TFEPI sequence (36 excitation pulses, of which the first two were startup pulses, with an EPI factor of 7) was used with an effective echo time of 5.3 ms. The field of view was 230 × 230 mm, and scan matrix was 128 × 128, which was reconstructed as 256 × 256 by zero-filling. 60 slices were acquired with a thickness of 1.8 mm and reconstructed as 120 slices with 0.9 mm thickness; however 10 slices at the top and bottom of the volume were discarded (20% oversampling). Sensitivity-encoding (SENSE) was applied in two directions with a factor of 2.4 in the anterior-posterior direction and 1.8 in feet-head direction. Directly after the 3D-TFEPI readout providing the 4D-MRA images, a multi-slice single-shot EPI sequence was performed for perfusion imaging with field of view = 240 × 240 mm, scan matrix = 80 × 80, 17 slices with thickness of 6.0 mm, echo time of 16 ms, and SENSE factor of 2.1 in anterior-posterior direction, excitation flip angle of 90°. The repetition time and total acquisition time of the combined sequence for 4D-MRA and perfusion imaging were 4322 ms and 4:46 min, respectively. With these imaging parameters, the number of shots needed to fill the complete k-space for 3D-TFEPI was 8, which implies that the complete Hadamard

matrix was repeated 8 times. This resulted in a total of 64 acquisitions for perfusion imaging, which should provide an SNR comparable to a traditional pCASL perfusion scan with 32 averages. For quantification of CBF, an M_0 image was acquired using identical acquisition parameters as the perfusion image, but without labeling, pre-saturation and background suppression pulses, and with the repetition time set to 2000 ms and 4 averages. Before the quantification process, the M_0 image was multiplied by the factor $1/(1-\exp(-TR/T_{1_gm}))$, where T_{1_gm} was assumed to be 1200 ms, to correct for incomplete T_1 recovery (5,18). For a quantitative comparison of the obtained CBF values, a traditional perfusion-only pCASL scan with identical geometric parameters was acquired with labeling duration as well as PLD set to 1800 ms. Background suppression pulses were applied at 1830 and 3150 ms. With 32 averages, total scan time of the traditional pCASL was 4:54 min. In this study, the total acquisition of the combined sequence of 4D-MRA and perfusion image was similar to the acquisition time of the traditional pCASL scan.

Image Processing of *In Vivo* Data

Image processing was performed offline using SPM 12 and custom-written scripts working in MATLAB.

All single-shot EPI time series for perfusion imaging, including the traditional pCASL scans, were motion-corrected and realigned to the M_0 image. Subsequently, the 3D-TFEPI images and the realigned single-shot EPI images of the simultaneous acquisition scheme were decoded by applying the proper Hadamard matrix, thereby providing 4D-MRA and multiple PLD perfusion images. From the 4D-MRA data sets, maximum intensity projection (MIP) images were generated for each temporal phase in sagittal, transverse and coronal directions. In this study, the first subbolus image was disregarded for 4D-MRA, whereas only the single-shot EPI images of the first subbolus were taken into account as perfusion images. For the traditional pCASL scan, subtraction of the labeled images from the control images was performed to obtain the perfusion images.

The CBF was calculated in accordance with the recommendation from the recent ASL white paper (5). For perfusion images acquired using the te-pCASL simultaneous acquisition sequence, however, an additional cosine term was added to correct for the saturation effects of the MRA readout by assuming that all transverse magnetization is spoiled before the next excitation pulse is applied, as follows:

$$CBF = \frac{6000 \cdot \lambda \cdot \Delta M \cdot \exp\left(\frac{PLD}{T_{1,blood}}\right)}{2 \cdot \alpha \cdot T_{(1,blood)} \cdot M_0 \cdot \left(1-\exp\left(\frac{\tau}{T_{1,blood}}\right)\right) \cdot (\cos\theta)^{\beta}} \quad [1]$$

where ΔM is the perfusion signal intensity, M_0 is the signal intensity of the M_0 image, λ is the brain/blood partition coefficient in mL/g, $T_{1,blood}$ is the longitudinal relaxation time of blood in ms, α is the labeling efficiency, τ is the labeling duration, θ is the flip angle for the 4D-MRA acquisition, and β is the number of excitation pulses per shot. Multi-slice acquisitions (as also used in this study) result in a slice-dependent PLD, which is corrected for in the quantification by prolonging the PLD by 40 ms for each subsequent slice.

In addition, the temporal SNR (tSNR) of each perfusion image was calculated as the mean perfusion signal divided by the standard error of the perfusion signal over the signal averages.

A GM mask was generated from the M_0 image using the segmentation tool on SPM 12 with the threshold set to 60% probability, and used to obtain the mean GM CBF and mean GM tSNR values. The normalized difference of mean GM CBF value over traditional pCASL was calculated as:

$$\text{Normalized difference (\%)} = \frac{CBF_{simul} - CBF_{trad}}{CBF_{trad}} \times 100 \quad [2]$$

where CBF_{simul} and CBF_{trad} are the mean GM CBF value obtained by the simultaneous acquisition and the traditional pCASL sequence, respectively. In addition, paired t-tests were performed using SPSS Statistics version 23 (IBM Corporation) and the mean GM CBF and tSNR values obtained from the simultaneous acquisition sequence were compared to the traditional pCASL, in which significance was set at $p<0.05$ using the Bonferroni method to correct for multiple comparisons.

Results

Bloch equation simulations provided the optimal timings of the two background suppression pulses (1850 and 3200 ms), by taking both the effects from the pre-labeling saturation pulses as well as the excitation pulses of the 4D-MRA acquisition into account, as illustrated in Figure 1 and 2.

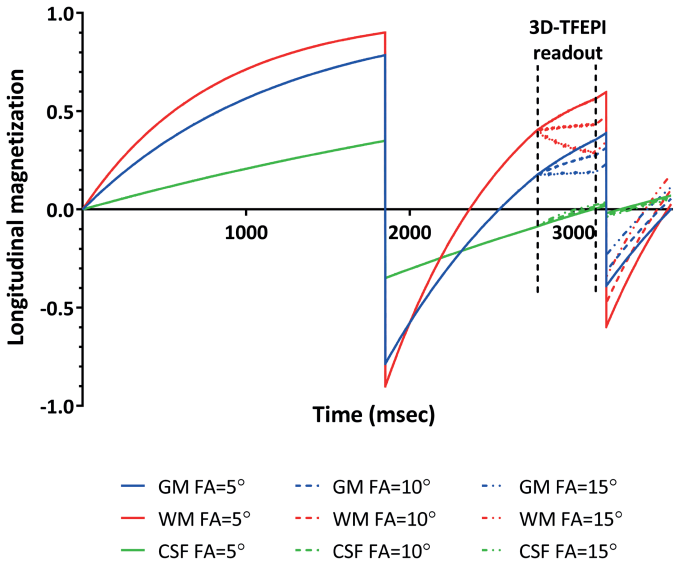


Figure 2: Bloch equation simulation results showing the evolution of the longitudinal magnetization during the sequence. For clarity, results with only flip angles of 5, 10 and 15° are shown.

Figure 3 shows the mean values of tSNR from the GM masked perfusion images acquired with the simultaneous acquisition sequence and the traditional pCASL as a reference, and representative CBF maps acquired with each setting. All flip angles (5, 7.5, 10, 12.5 and 15°) showed statistically significant decrease of tSNR as compared to the traditional pCASL. Moreover, as Table 1 indicates, there was a significant overestimation of the mean GM CBF values as obtained by the highest flip angles (10, 12.5 and 15°) when compared to the values as acquired by traditional pCASL, which suggests that the correction for the saturation effects of the 3D-TFEPI excitation pulses was especially not accurate for these flip angles. Although some overestimation was observed also for lower flip angles (5 and 7.5°), these differences did not reach statistical significance. Furthermore, some of the overestimation is caused by decoding artefacts in volunteer 4 († in Table 1), as illustrated in Figure 4 (high arterial signal indicated with yellow arrows) and elaborated further subsequently. Figure 5 shows that this observed deviation is dependent on the position of the slice. For all flip angles, overestimation was observed either or both top and bottom slices, whereas larger deviations were observed for the higher flip angles.

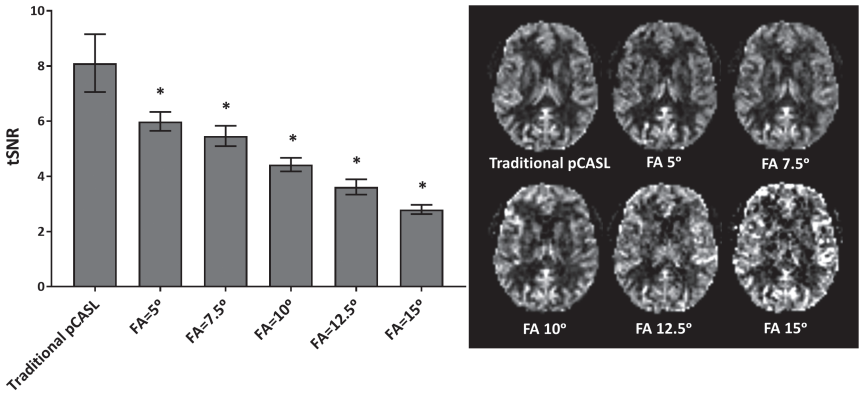


Figure 3: Temporal SNR (tSNR) for the perfusion images as acquired with the combined sequence with different excitation flip angles (FA) of the 4D-MRA acquisition and traditional pCASL. Values are averaged over the whole brain gray matter. Error bars show the standard deviation over six volunteers (* $p<0.05$ after Bonferroni correction). Representative cerebral blood flow (CBF) maps as acquired with each setting are also shown.

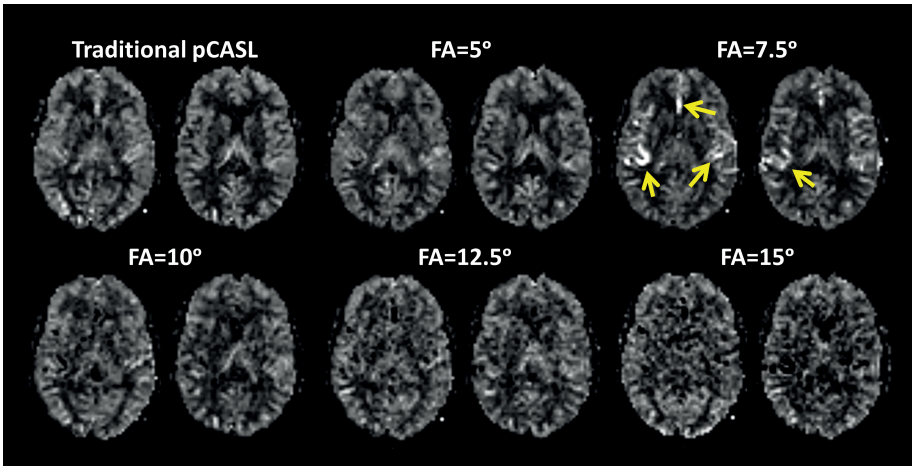


Figure 4: Cerebral blood flow (CBF) maps obtained from volunteer 4 in Table 1. Arrows indicate shine-through artefacts of signal from the angiographic subboli.

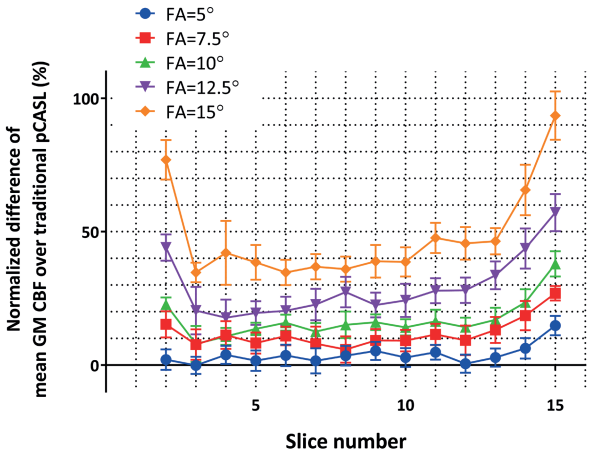


Figure 5: Normalized difference of the mean gray matter (GM) CBF of the combined sequence as compared with the one obtained by the traditional pCASL sequence. Larger deviations are observed for the top and bottom slices. As a result of the applied motion correction, some parts of the top and bottom slices provided incomplete data; therefore the first and last two slices were not included in the graph.

Table 1: Mean gray matter (GM) CBF values from each volunteer for the different excitation flip angle of the 4D-MRA and their normalized difference over CBF value acquired by the traditional pCASL. Shown p-values were obtained by paired t-tests for each flip angle of 4D-MRA acquisition compared to the traditional pCASL, in which significance (*) was set at $p<0.05$ using the Bonferroni correction. In the table (†) shows the increased CBF value suggesting an overestimation due to the residual arterial signal shown in Figure 4 (arrows).

	Volunteer 1	Volunteer 2	Volunteer 3	Volunteer 4	Volunteer 5	Volunteer 6	Mean / SD (p-value)
Traditional pCASL	45.24	43.71	42.79	37.97	56.24	44.76	45.12 / 6.04
Flip angle = 5°	47.22 (4.4%)	45.40 (3.9%)	42.13 (-1.5%)	40.80 (7.5%)	50.88 (-9.5%)	52.26 (16.8%)	46.45 / 4.60 (0.476)
Flip angle = 7.5°	47.92 (5.9%)	47.18 (7.9%)	43.57 (1.8%)	50.30† (32.5%)	56.24 (0.0%)	51.95 (16.1%)	49.53 / 4.36 (0.067)
Flip angle = 10°	54.23 (19.9%)	50.30 (15.1%)	45.19 (5.6%)	49.00 (29.0%)	60.31 (7.2%)	54.43 (21.6%)	52.24 / 5.25 (0.004) *
Flip angle = 12.5°	51.17 (13.1%)	54.16 (23.9%)	57.78 (35.0%)	53.64 (41.3%)	64.86 (15.3%)	61.74 (37.9%)	57.23 / 5.25 (0.001) *
Flip angle = 15°	66.40 (46.8%)	67.04 (53.4%)	59.04 (38.0%)	61.49 (61.9%)	72.46 (28.8%)	61.42 (37.2%)	64.64 / 4.93 (0.000) *

Figure 4 shows the CBF maps obtained from one of volunteers (volunteer 4 in Table 1), in which the CBF map with flip angle of 7.5° showed high arterial signal, which is presumably caused by residual ASL signal within the arteries from other subboli (for 4D-MRA acquisition) that was supposed to be canceled out by decoding. The overestimation of GM CBF when using a flip angle of 7.5° could be partly attributed to the residual arterial signal in this volunteer († in Table 1). More detailed discussion about the residual ASL signal is provided within the discussion.

Representative 4D-MRA images acquired with flip angles of 5, 7.5 and 10° are shown in Figure 6. With a flip angle of 5°, visualization of the peripheral arteries was found to be weak, which obscured depiction of the more distal parts when compared to the images obtained with a flip angle of 7.5°. In contrast, increasing the flip angle to 10° or higher (not shown) did not improve the visualization of the peripheral arteries, although the signal intensity within the larger arteries was increased. In addition, some volunteers showed ghosting of residual arterial signal from the M1 part of the middle cerebral artery from the earlier phases onto later ones (arrows on Figure 7) when using higher flip angles, which is presumed to be the same phenomenon as shown in Figure 4. In this study, a flip angle of 7.5° was found to be an optimal compromise to obtain a sufficient image quality of CBF map, while still achieving reasonable visualization of the arteries (Figure 8).

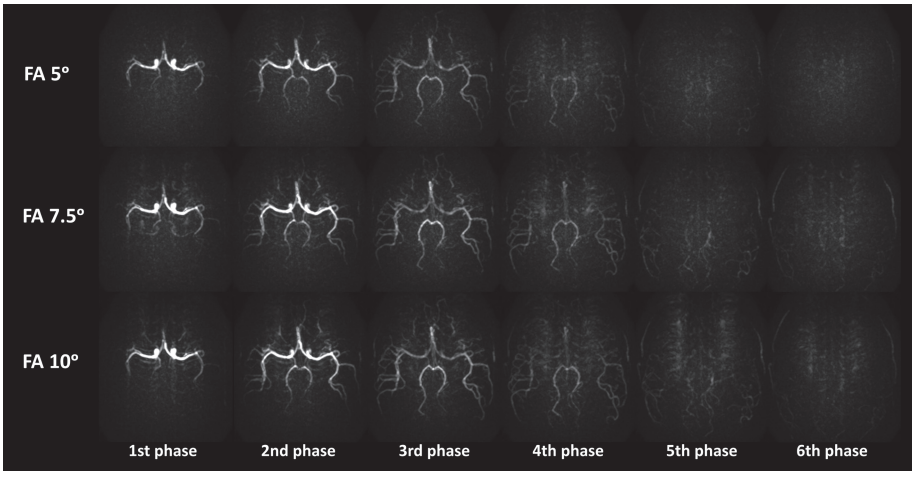


Figure 6: Representative MRA images acquired with flip angles of 5, 7.5 and 10°. With a flip angle of 5°, visualization of the peripheral arteries was found to be weak compared to the images obtained with a flip angle of 7.5°. Although a flip angle of 10° increased the signal intensity of arteries, however, visualization of the distal parts of arteries was not improved.

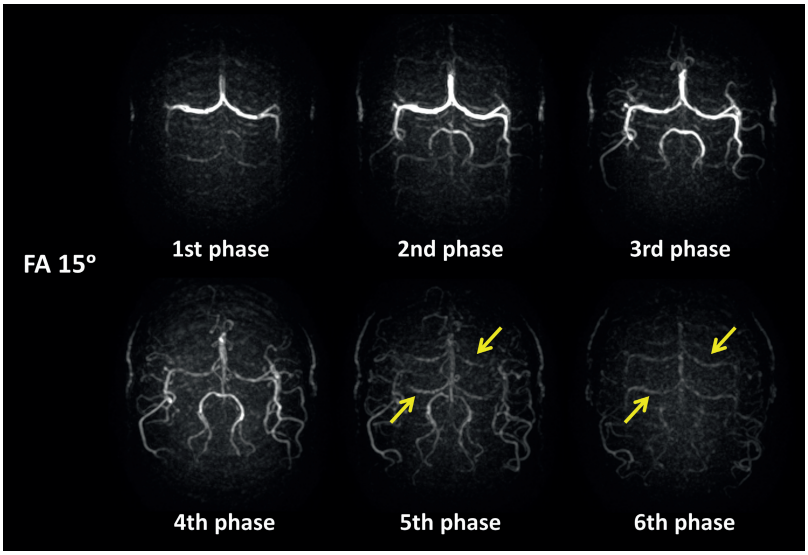


Figure 7: Representative MRA images acquired with a flip angle (FA) of 15°. Arrows indicate ghosting of residual arterial signal from the M1 part of the middle cerebral artery as present during the earlier phases. Ghosting is especially seen when using higher flip angles for the 3D-TFEPI readout.

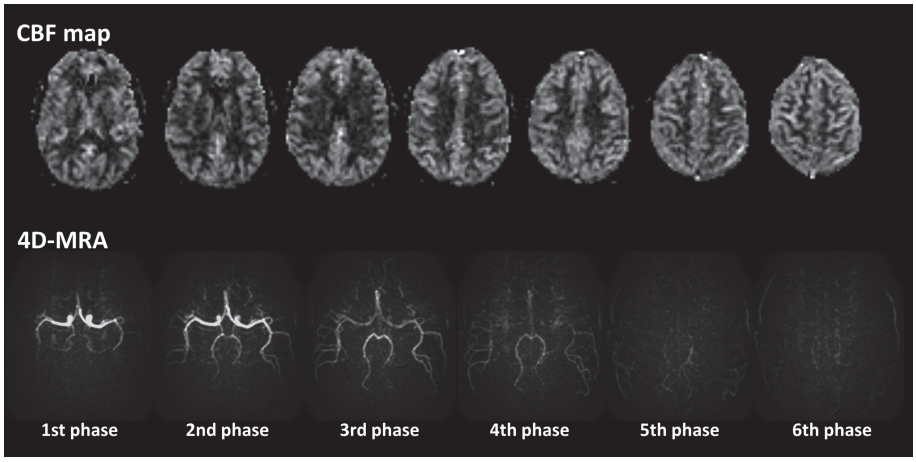


Figure 8: Representative 4D-MRA and perfusion images using flip angle of 7.5°, showing a suitable compromise between sufficient image quality of the CBF maps and visualization of the passage of the labeled blood through the arterial system.

Discussion

In this manuscript we proposed a new technique that allows simultaneous acquisition of perfusion and 4D-MRA images in a single scan. By using te-pCASL with optimized settings of the labeling duration of the subboli, sufficient labeling duration and PLD can be achieved for perfusion imaging, whereas sufficient temporal resolution to allow visualization of the early arterial phase is obtained for 4D-MRA with short labeling duration and PLD. Also, by the use of te-pCASL for obtaining dynamic information instead of the more traditional Look-Locker approach, severe saturation of the labeled blood signal is prevented, thereby still allowing perfusion imaging with sufficient image quality.

In this study, a statistically significant decrease in tSNR as a result of saturation effects was observed for all flip angles. Moreover, the quantitative mean GM CBF values tended to be higher than those acquired with traditional pCASL, which is most probably arising from overcorrection of the saturation effects and could be explained by two possible reasons. Firstly, when some labeled blood would not experience all excitation pulses of the 4D-MRA readout (e.g. because the imaging area was not yet reached) while contributing to the perfusion signal, correction based on all excitation RF pulses would cause an overcorrection. In this study, however, there is an interval of approximately 1 second between the end of the perfusion labeling (subbolus 1) and the start of 4D-MRA acquisition, which is presumably sufficient for all, or at least the vast majority, of the labeled blood to arrive at the imaging volume. The second, and more plausible, reason is that there is a small, but noticeable, discrepancy between the intended flip angle and the nominal flip angle for the volume-selective excitation pulses of the 4D-MRA readout. Although the saturation effects are corrected for by the cosine term in the denominator of equation [1], such a discrepancy in the nominal flip angle is prone to be larger for higher flip angles, thereby resulting in a larger overcorrection of CBF, especially for the highest flip angles of 10, 12.5 and 15°. Although overestimation was also observed with lower flip angles of 5 and 7.5°, it was relatively small and no longer statistically significant. Non-ideal excitation profiles would lead to a larger discrepancy in nominal flip angle near the edges of the imaging volume, which was indeed also the location where the most severe overestimation was observed (see Figure 5). Pulses with better excitation profile or inclusion of the excitation profile into the post-processing could potentially alleviate these issues, but the use of lower flip angles for 4D-MRA is suggested not only to reduce overestimation of CBF values, but also to avoid other imaging artefacts (see e.g. arrows in Figure 7).

In te-pCASL, the acquired images (i.e., before decoding) contain the combined information of static tissue as well as the cumulative effect of the labeling/control conditions from all subboli. During the decoding process, the ASL signal from only one certain subbolus is supposed to add constructively, whereas signal from all other subboli and static tissue are expected to be canceled out. However, because of signal fluctuations, residual ASL signal from other subboli could appear in other phases as a "shine-through effect". Such shine-through effects were most evident as a ghosting of arterial signal in the peripheral and perfusion phases, probably because of two reasons. First, changes in labeling efficiency due to pulsatile flow at the labeling plane causes slight signal fluctuations, preventing complete cancelation of ASL signal from other subboli during decoding. Because the ASL signal has not attenuated much as a result of relaxation in the early arterial phase, and the signal is concentrated in the arteries with little dispersion, the shine-through effects of angiographic signal (e.g. the M1 part of the middle cerebral artery) have a larger risk of causing a shine-through effect to later phases that have a much lower, perfusion type of signal distribution. Another possible reason is also related to the pulsatile flow, although not at the labeling plane, but at the arteries themselves. In ASL based 4D-MRA, the control condition shows high signal intensities in the arteries as a result of inflow effects. This arterial signal intensity could, however, also be affected by pulsation and therefore show signal fluctuations, which causes incomplete cancelation of signal from other subboli. A high flip angle readout will amplify both of these phenomena; therefore, the use of relatively small flip angles is recommended for the 4D-MRA part of the proposed sequence.

Although segmented 3D sequence (e.g. 3D GRASE and 3D stack of spirals) are preferable readout modules for traditional ASL scans, because of optimal background suppression over the whole imaging volume (5), te-pCASL results in an increased temporal foot-print, making segmented 3D readout acquisitions more prone to motion artefacts (20), while single-shot 3D readout approaches suffer from blurring. Therefore, a single-shot multi-slice EPI sequences was used in this study, even though development of improved 3D sequences that allow single-shot readout (or with a low number of segments), while avoiding blurring, could bring further improvements to our approach.

For acquisition of 4D-MRA, an EPI factor of 7 was chosen based on pilot studies optimizing scan time and image quality. The use of TFEPI (segmented EPI) sequence not only reduced the total scan time but also limited the number of RF excitation pulses, thereby preserving more labeled longitudinal magnetization for perfusion imaging. In this study, no obvious artefacts originating from off-resonance effects

near the skull base were observed. In subjects with relatively large paranasal sinuses, however, it is known that off-resonance artefacts may occur, which could require special attention.

There are three important limitations of the proposed approach that should be mentioned. First, the temporal resolution of te-pCASL technique is determined by the durations of the labeling subboli, in which too short subboli (i.e., a higher temporal resolution) would create too little labeled blood to accurately visualize smaller arteries, especially in later phases when label has already decayed to some extent. In this study, the temporal resolution was set to 130 ms as a compromise between temporal resolution and visualization of smaller arteries. This temporal resolution compares well to literature in which clinical studies reported good to excellent agreement between ASL-based 4D-MRA with temporal resolution of 150 – 300 ms and digital subtraction angiography in Moyamoya disease (3), dural arteriovenous fistulas (1) and collateral circulation in steno-occlusive diseases (21).

The second limitation is that the excitation coverage for the 4D-MRA readout should be the same as or larger than the coverage of the perfusion images; otherwise the saturation effects on the perfusion image would differ among slices, which would require more complicated correction approaches of these saturation effects. To achieve whole brain coverage within the limited acquisition time, the spatial resolution of the 4D-MRA readout of this technique is still lower than commonly used 3D time-of-flight MRA, as well as ASL-based 4D-MRA techniques that have the sole goal of acquiring dynamic angiographic images. This originated from our design criterion of achieving a comparable scan time for the combined sequence to a typical pCASL perfusion scan (shorter than 5 minutes). Therefore, the 4D-MRA acquired with this technique is not supposed to act as a replacement of 3D-MRA, and separate acquisition of high resolution 3D time-of-flight MRA is recommended when necessary. In addition, when hemodynamic information of smaller arteries is required (such as visualization of a small feeding artery to an arteriovenous malformation (22), dural arteriovenous fistulas (1), or small collateral arteries (21)), independent 4D-MRA with higher spatial resolution, would be preferred. Instead, the main benefit of the proposed technique is that dynamic, macroscopic hemodynamic information can be added to conventional, static perfusion imaging while still keeping sufficient quality of the perfusion images (see Figure 3 and 8).

Finally, investigation was limited to healthy volunteers in this study. Further validation of this approach in patients with cerebrovascular disease is needed before clinical use is undertaken.

Conclusions

In summary, we have presented a novel technique for simultaneous acquisition of perfusion and 4D-MRA images. In this study, the use of te-pCASL with optimized labeling duration of the subboli provided sufficient labeling duration and PLD for perfusion imaging, while sufficient temporal resolution to visualize the early arterial phase was obtained for 4D-MRA. Reduction of the saturation effects from excitation pulses for 4D-MRA acquisition on the perfusion image was achieved by use of te-pCASL as well as 3D-TFEPI sequence with relatively low excitation flip angles for 4D-MRA, thereby allowing the additional acquisition of 4D-MRA, while maintaining sufficient image quality of the CBF maps.

Acknowledgements

This research was supported by the EU under the Horizon2020 program (project: CDS-QUAMRI)

References

1. Iryo Y, Hirai T, Kai Y, Nakamura M, Shigematsu Y, Kitajima M, Azuma M, Komi M, Morita K, Yamashita Y. Intracranial dural arteriovenous fistulas: evaluation with 3-T four-dimensional MR angiography using arterial spin labeling. Radiology 2014;271(1):193-199.
2. Suzuki Y, Fujima N, Ogino T, Meakin JA, Suwa A, Sugimori H, Van Cauteren M, van Osch MJP. Acceleration of ASL-based time-resolved MR angiography by acquisition of control and labeled images in the same shot (ACTRESS). Magn Reson Med 2018;79(1):224-233.
3. Uchino H, Ito M, Fujima N, Kazumata K, Yamazaki K, Nakayama N, Kuroda S, Houkin K. A novel application of four-dimensional magnetic resonance angiography using an arterial spin labeling technique for noninvasive diagnosis of Moyamoya disease. Clin Neurol Neurosurg 2015;137:105-111.
4. Yan L, Salamon N, Wang DJ. Time-resolved noncontrast enhanced 4-D dynamic magnetic resonance angiography using multibolus TrueFISP-based spin tagging with alternating radiofrequency (TrueSTAR). Magn Reson Med 2014;71(2):551-560.
5. Alsop DC, Detre JA, Golay X, Gunther M, Hendrikse J, Hernandez-Garcia L, Lu H, MacIntosh BJ, Parkes LM, Smits M, van Osch MJ, Wang DJ, Wong EC, Zaharchuk G. Recommended implementation of arterial spin-labeled perfusion MRI for clinical applications: A consensus of the ISMRM perfusion study group and the European consortium for ASL in dementia. Magn Reson Med 2015;73(1):102-116.
6. Alsop DC, Detre JA. Reduced transit-time sensitivity in noninvasive magnetic resonance imaging of human cerebral blood flow. J Cereb Blood Flow Metab 1996;16(6):1236-1249.
7. Gunther M, Bock M, Schad LR. Arterial spin labeling in combination with a look-locker sampling strategy: inflow turbo-sampling EPI-FAIR (ITS-FAIR). Magn Reson Med 2001;46(5):974-984.
8. Wells JA, Lythgoe MF, Gadian DG, Ordidge RJ, Thomas DL. In vivo Hadamard encoded continuous arterial spin labeling (H-CASL). Magn Reson Med 2010;63(4):1111-1118.
9. Gunther M. Highly efficient accelerated acquisition of perfusion inflow series by Cycled Arterial Spin Labeling. In Proceedings of the 16th Annual Meeting of ISMRM 2007:380.
10. Teeuwisse WM, Schmid S, Ghariq E, Veer IM, van Osch MJ. Time-encoded pseudocontinuous arterial spin labeling: basic properties and timing strategies for human applications. Magn Reson Med 2014;72(6):1712-1722.
11. Dai W, Shankaranarayanan A, Alsop DC. Volumetric measurement of perfusion and arterial transit delay using hadamard encoded continuous arterial spin labeling. Magn Reson Med 2013;69(4):1014-1022.
12. Suzuki Y, Teeuwisse WM, Schmid S, Koken P, Van Cauteren M, Helle M, van Osch MJP. Simultaneous acquisition of perfusion maps and 4D MR angiography by means of arterial spin labeling MRI. In Proceesings of the 23th Annual Meeting of ISMRM 2014:720.
13. Wielopolski PA, Adamis M, Prasad P, Gaa J, Edelman R. Breath-hold 3D STAR MR angiography of the renal arteries using segmented echo planar imaging. Magn Reson Med 1995;33(3):432-438.
14. Gai ND, Talagala SL, Butman JA. Whole-brain cerebral blood flow mapping using 3D echo planar imaging and pulsed arterial tagging. J Magn Reson Imaging 2011;33(2):287-295.
15. Henningsson M, Mens G, Koken P, Smink J, Botnar RM. A new framework for interleaved scanning in cardiovascular MR: Application to image-based respiratory motion correction in coronary MR angiography. Magn Reson Med 2015;73(2):692-696.
16. Ordidge RJ, Wylezinska M, Hugg JW, Butterworth E, Franconi F. Frequency offset corrected inversion (FOCI) pulses for use in localized spectroscopy. Magn Reson Med 1996;36(4):562-566.
17. Rydhog AS, van Osch MJ, Lindgren E, Nilsson M, Latt J, Stahlberg F, Wirestam R, Knutsson L. Intravoxel incoherent motion (IVIM) imaging at different magnetic field strengths: what is

feasible? Magn Reson Imaging 2014;32(10):1247-1258.
18. Lu H, Nagae-Poetscher LM, Golay X, Lin D, Pomper M, van Zijl PC. Routine clinical brain MRI sequences for use at 3.0 Tesla. J Magn Reson Imaging 2005;22(1):13-22.
19. Rooney WD, Johnson G, Li X, Cohen ER, Kim SG, Ugurbil K, Springer CS, Jr. Magnetic field and tissue dependencies of human brain longitudinal 1H2O relaxation in vivo. Magn Reson Med 2007;57(2):308-318.
20. van Osch MJ, Teeuwisse WM, Chen Z, Suzuki Y, Helle M, Schmid S. Advances in arterial spin labelling MRI methods for measuring perfusion and collateral flow. J Cereb Blood Flow Metab 2017:271678X17713434.
21. Iryo Y, Hirai T, Nakamura M, Inoue Y, Watanabe M, Ando Y, Azuma M, Nishimura S, Shigematsu Y, Kitajima M, Yamashita Y. Collateral circulation via the circle of Willis in patients with carotid artery steno-occlusive disease: evaluation on 3-T 4D MRA using arterial spin labelling. Clin Radiol 2015;70(9):960-965.
22. Yu S, Yan L, Yao Y, Wang S, Yang M, Wang B, Zhuo Y, Ai L, Miao X, Zhao J, Wang DJ. Noncontrast dynamic MRA in intracranial arteriovenous malformation (AVM), comparison with time of flight (TOF) and digital subtraction angiography (DSA). Magn Reson Imaging 2012;30(6):869-877.

Chapter 6

A Framework for Motion Correction of Background Suppressed Arterial Spin Labeling Perfusion Images Acquired with Simultaneous Multi-Slice EPI

Magn Reson Med 2018: 1-13. https://doi.org/10.1002/mrm.27499

Yuriko Suzuki
Thomas W. Okell
Michael A. Chappell
Matthias J. P. van Osch

Abstract

Purpose: When employing simultaneous multi-slice (SMS-) EPI for background suppressed (BGS-) arterial spin labeling (ASL), correction of through-plane motion could introduce artefacts, since the slices with most effective BGS are adjacent to slices with the least BGS. In this study, a new framework is presented to correct for such artefacts.

Methods: The proposed framework consists of three steps: (i) homogenization of the static tissue signal over the different slices to eliminate most inter-slice differences due to different levels of BGS, (ii) application of motion correction, and, (iii) extraction of perfusion-weighted signal using a general linear model. The proposed framework was evaluated by simulations and a functional ASL-study with intentional head-motion.

Results: Simulation studies demonstrated that the strong signal differences between slices with the most and least effective BGS caused suboptimal estimation of motion parameters when through-plane motion was present. Although use of the M_0 image as the reference for registration allowed 82% improvement of motion estimation for through-plane motion, it still led to residual subtraction errors caused by different static tissue signal between control and label due to different BGS levels. By using our proposed framework, those problems were minimized and the accuracy of CBF estimation was improved. Moreover, the functional ASL study showed improved detection of visual and motor activation when applying the framework as compared to conventional motion correction, as well as when motion correction was completely omitted.

Conclusion: When combining BGS-ASL with SMS-EPI, particular attention is needed to avoid artefacts introduced by motion correction. With the proposed framework these issues are minimized.

Introduction

Simultaneous multi-slice (SMS, a.k.a multiband) EPI excites multiple slices at the same time, and therefore reduces the number of excitation pulses per repetition time (TR) (1,2). This approach has been proven to be very advantageous for functional MRI (fMRI) and diffusion tensor imaging (DTI) (1,3). Whereas for fMRI and DTI the prime advantage of SMS-EPI is the acceleration of the acquisition by shortening TR, for arterial spin labeling (ASL) this is much less beneficial because the preparation module for labeling and post-labeling delay (PLD) is the main time-consuming part of the sequence and not the readout. For measurement of tracer kinetics using multi time-point ASL, however, SMS allows the number of slices to be increased within a limited acquisition window to achieve whole-brain coverage (4,5). Another advantage of SMS for 2D-multislice-ASL is smaller variation of the level of background suppression (BGS) (6) and PLD (7) over the acquired slices. Most ASL sequences now employ BGS to decrease physiological noise and motion artefacts from background static tissue, thereby improving the signal to noise ratio (SNR). BGS is highly effective in 3D multi-shot readout sequences because the image data is acquired after a single excitation per TR, which can be timed to have optimal BGS (8). However, for certain applications such as ASL-fMRI, a single-shot readout is preferred to achieve high temporal resolution, hence multi-slice single-shot EPI is still common as a readout module for ASL (9). In multi-slice ASL, optimal BGS is usually timed to occur for the first slice, whereas longitudinal relaxation will reduce the effectiveness of BGS for more distal slices that are typically acquired hundreds of milliseconds later than the first slice. Similarly, the effective PLD of the distal slices will be hundreds of milliseconds longer than the PLD of the first slice, leading to interpretation issues as well as a loss of SNR in more distal slices. Therefore, shortening the total readout duration by use of SMS-EPI could help to minimize both detrimental effects.

The combination of SMS and BGS, although desirable for the reasons outlined above, could also potentially introduce new problems when motion correction (MoCo) is required as illustrated in Figure 1. In Figure 1 it can be seen that, with the SMS-excitation, slices with the most effective BGS will be adjacent to slices that experience the least effective BGS (see the two slices indicated with yellow circles in Figure 1a), which results in discrete dark lines clearly visible on sagittal and coronal reformatted images as shown in Figure 1b. These will be referred to as "BGS dark-lines" throughout this article. The presence of the BGS dark-lines might hamper a successful registration procedure that is required for good MoCo, because such a registration algorithm might attempt to align the BGS dark-lines, instead of registering the underlying anatomical structures. Therefore, the motion could be poorly estimated, especially when motion

occurs in the slice-selection direction as a result of rotation around the x- or y-axes or translation in the z-direction. Furthermore, and more importantly, even assuming registration works correctly, another problem will occur: when a certain part of the cortex moves in the slice direction during either the label or control condition (e.g. a control image without motion and a labeled image with motion, as illustrated in Figure 1c), the tissue would experience different levels of BGS for the label and control conditions. The difference of BGS effectiveness will be especially significant when tissue moves between slice locations with the most and least effective BGS. In such a situation, even when the registration worked successfully and the tissue is correctly realigned to its original location, severe subtraction errors would occur (red circle in Figure 1c) as a result of the significant difference in static tissue signal for the label and control conditions. This problem will be referred to as "BGS subtraction error" throughout this article.

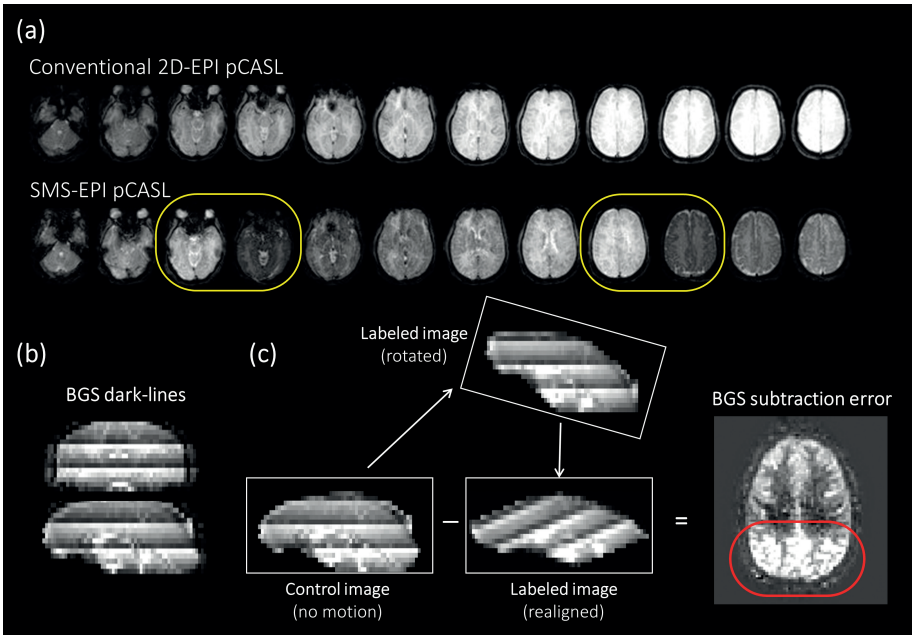


Figure 1: Schematic figures illustrating the potential issues that could arise when motion correction (MoCo) is applied to background suppressed (BGS-) ASL acquired with simultaneous multi-slice (SMS-) EPI: (a) BGS-image of conventional 2D-EPI and SMS-EPI pCASL, where yellow circles show slices with the most effective and poorest BGS immediately next to each other. (b) Dark-lines observed on reformatted images, produced by slices with the most effective and poorest BGS (BGS dark-lines). (c) Subtraction between a control image without motion and a label image with through-plane rotation (realigned). The red circle shows the subtraction errors caused by the different background static signal intensity between control and label images (BGS subtraction errors).

In this article, we present a new framework to deal with both sources of error in background suppressed SMS-ASL imaging, which will enable accurate MoCo realignment as well as a separation of the perfusion-weighted signal from the above-mentioned BGS subtraction errors.

Methods

Correction Framework

The proposed framework consists of three steps:

(i) Homogenization of static tissue signal over the different slices is performed to reduce inter-slice signal intensity differences as caused by the SMS acquisition with BGS. The slice-wise mean BGS effect is estimated by:

$$BGS_{effect}(\text{slice z}) = \frac{\text{mean tissue value of slice z of } M_0 \text{ image}}{\text{mean tissue value of slice z of BGS–ASL image}} \quad [1]$$

where the averaging for the mean tissue value of BGS-ASL was performed over all dynamic volumes, and homogenization is performed by multiplying the BGS-ASL time-series images by BGS_{effect}. Although the main purpose of homogenization is to minimize BGS subtraction errors by homogenizing the inter-slice signal intensity, it will also avoid erroneous MoCo estimation due to the BGS dark-lines as shown in Figure 1(b).

(ii) MoCo registration based on the conventional rigid-body transformation is performed by commonly available software such as SPM (10) or FSL (11), while using the M_0 image as reference, which is chosen based on the absence of dark-lines. In addition, an extra 4D-dataset of the same size is created, which at first has a constant value equal to BGS_{effect} for each slice, but is subsequently resliced according to the motion parameters as estimated by the MoCo for the ASL time-series. This new dataset will be referred to as "resliced BGS_{effect}" and used in the third step.

(iii) Perfusion-weighted signal is extracted. A standard subtraction of label from control images would not extract the perfusion-weighted signal correctly, because the perfusion-weighted signal was scaled by the BGS_{effect} during the homogenization process of step (i). Moreover, because the application of BGS_{effect} only achieves slice-wise homogenization of the static tissue signal, there will remain some BGS-variations at the voxel-level that will still lead to some residual BGS subtraction errors when through-slice motion occurs. To correct for both effects, it is proposed to use a

general linear model (GLM) regression to 1) rescale the perfusion-weighted signal as well as to 2) separate the perfusion-weighted signal from residual errors. The GLM is represented as:

$$y_t = \beta_{baseline} x_{t_baseline} + \beta_{perf} x_{t_perf} + \beta_{error} x_{t_error} + e \quad [2]$$

where y_t is the motion corrected ASL time-series at a certain voxel. The regressors that constitute the design matrix are: $x_{t_baseline} = 1$ for baseline tissue signal, x_{t_perf} that describes the labeling paradigm $[0.5, -0.5, \ldots, 0.5, -0.5]^T$ and x_{t_error} that represents an estimate of the pixel-wise residual error. As mentioned above, because the perfusion-weighted signal was scaled by the BGS_{effect} during the homogenization process, x_{t_perf} was also multiplied by the resliced BGS_{effect} that was generated at the step (ii). It should be noted that the resliced BGS_{effect} will both depend on the location within the images as well as on the temporal profile and extent of the through plane motion. In this study, x_{t_error} was generated from subtraction of the homogenized (BGS-removed) ASL time-series before and after MoCo. This regressor will be dominated by static tissue signal changes and will therefore be a reasonable surrogate for the residual error after MoCo. $\beta_{baseline}$, β_{perf} and β_{error} are fitting coefficients for $x_{t_baseline}$, x_{t_perf} and x_{t_error}, i.e. $\beta_{baseline}$ and β_{perf} represent the homogenized background tissue image and the baseline perfusion-weighted (ΔM) image, respectively. *e* is the fitting error. When ASL-fMRI is performed, an additional regressor is added:

$$y_t = \beta_{baseline} x_{t_baseline} + \beta_{perf} x_{t_perf} + \beta_{act_perf} x_{t_act_perf} + \beta_{error} x_{t_error} + e \quad [3]$$

where $x_{t_act_perf}$ describes the perfusion signal changes as a result of activation and β_{act_perf} is the fitting coefficients for $x_{t_act_perf}$. Please note that $x_{t_act_perf}$ is also multiplied by the resliced BGS_{effect}, similar as described above.

Simulation

All simulations and image processing were performed offline using SPM 12 and custom-written scripts in MATLAB (MathWorks, Natick, MA, USA).

A dataset of single-PLD pseudo-continuous ASL (pCASL), M_0 image, and a quantitative T_1 map, all at the same spatial resolution, were used from a single subject out of a previous in vivo healthy volunteer perfusion study (see Table 1 in ref (12) for acquisition details). The quantitative CBF map was calculated in accordance with the recommendation from the recent ASL white paper (8):

$$CBF = \frac{6000 \cdot \lambda \cdot \Delta M \cdot \exp\left(\frac{PLD}{T_{(1,blood)}}\right)}{2 \cdot \alpha \cdot T_{(1,blood)} \cdot M_0 \cdot \left(1-\exp\left(\frac{\tau}{T_{(1,blood)}}\right)\right)} \quad [4]$$

where ΔM is the perfusion-weighted signal intensity, M_0 is the signal intensity of the M_0 scan, and τ is the labeling duration. The values from the white paper for the brain/blood partition coefficient (λ) of 0.95 mL/g, the $T_{1,blood}$ of 1650 ms, and labeling efficiency (α) of 0.85 were used.

From the M_0 image, seven time-series of 60 dynamic images each were generated and six different types of motion (translation in the x-, y- and z-direction and rotation around the x-, y- and z-axes) were applied to six of them. As illustrated in Figure 2, each type of motion has a four-step pattern in a single time-series: ±1.4 and ±2.8 fractional pixel translation (±4.2 and ±8.4 mm) in the x- and y-direction, ±0.6 and ±1.2 fractional slice shift (±4.2 and ±8.4 mm) in the z-direction, and ±3 and ±6 degree rotation around the x-, y- and z-axes. One time-series was untouched (no-motion dataset).

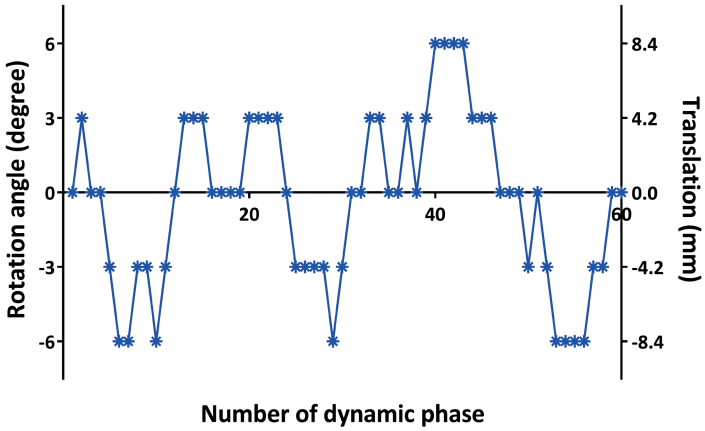


Figure 2: Motion applied to the simulated dataset: ±1.4 and 2.8 fractional pixel translation (±4.2 and 8.4 mm) in the x- and y-direction, ±0.6 and 1.2 fractional slice shift (±4.2 and 8.4 mm) in z-direction and ±3 and 6 degree rotation around the x-, y- and z-axes.

By using the T_1 map, the pixel-wise signal attenuation as a result of two BGS inversion pulses (TI = 1860 and 3150 ms) was calculated, in which different PLDs for the multi-slice acquisition were incorporated by assuming an interval of 30 ms between two subsequent excitation pulses; SMS acquisition with factor 3 was assumed and the following standard Bloch equation was used for calculating the evolution of the longitudinal magnetization:

$$M_z(t) = M_0 \left(1\text{-}\exp\left(-\frac{t}{T_1}\right)\right) + M_z(0)\exp\left(-\frac{t}{T_1}\right) \quad [5]$$

where $M_z(t)$ is the longitudinal magnetization at time-point t, M_0 and T_1 are pixel-wise values from the M_0 image and T_1 map, respectively. Afterward, perfusion-like signal changes were incorporated to the even dynamic numbers to represent the labeled images. Perfusion-like signal was only added to the left side of the brain, thereby keeping the right side without perfusion, in which all signal intensity that would appear after the post-processing will be a measure of the artefactual signal as a result of applied post-processing without any influence of the underlying perfusion pattern. Using these datasets, two studies were carried out:

Simulation-1: *Comparison of MoCo estimation.* First it was studied whether MoCo would indeed be impaired in SMS-ASL data with BGS that exhibit the BGS dark-lines and whether the performance of MoCo would be improved by the homogenization

step (step-(i) of the correction framework) as well as by using the M_0 image as reference for registration, instead of one dynamic out of the SMS-ASL dataset. All six motion-corrupted datasets underwent four types of MoCo registration defined as follows:

MoCo-A: with BGS dark lines present and the use of the firstly acquired ASL image as reference

MoCo-B: with BGS dark lines present and the use of the M_0 image as reference (instead of the firstly acquired ASL image)

MoCo-C: with homogenization and the use of the firstly acquired ASL image as reference

MoCo-D: with homogenization and the use of the M_0 image as reference

As a reference for the MoCo performance comparison, another set of six motion-corrupted datasets was created with exactly the same motion patterns, but without BGS- and perfusion-like signal attenuation, that also underwent the MoCo registration (referred to as "ref-no-BGS"). This separate reference dataset allows any errors resulting from the suboptimal performance of MoCo unrelated to BGS dark-lines to be excluded from the evaluations. For each six time-series with different types of motion as described above, six motion parameters (translation in x-, y- and z-direction and rotation around x-, y- and z-direction) were estimated by *MoCo-A*, *-B*, *-C* and *-D*, and the normalized mean difference with regard to the reference was calculated, which was normalized by the size of the simulated translation and rotation.

Simulation-2: *Separation of the perfusion-weighted signal*. All six motion-corrupted datasets underwent the proposed post-processing framework i.e. the homogenization, MoCo (*MoCo-D* in simulation-1), and GLM as described above, which will be referred to as "*NewMoCo*". Using the obtained β_{perf} map (i.e. ΔM image) and the M_0 image, the CBF map was calculated by applying equation [4]. For comparison, CBF maps were also calculated using ΔM images obtained by GLM but without the homogenization step (*MoCo-B* in simulation-1), referred to as "*StdMoCo*", GLM without both the homogenization step and MoCo, referred to as "*NoMoCo*", and also with the same framework as *NewMoCo,* but without including the error regressor "x_{t_error}" in the design matrix, referred to as "$NewMoCo_{wo_error_reg}$".

All signal intensities observed in the right side of the brain represent the level of artefactual signal arising from the applied post-processing, i.e. the signal intensity will be close to zero when errors such as BGS subtraction errors as well as conventional type of subtraction error due to inaccurate motion estimation (or when MoCo is not applied) are corrected well.

In Vivo ASL-fMRI Study with Healthy Volunteers

The study was approved by the local institutional review board and all volunteers provided written informed consent before inclusion into this study. A total of four volunteers (2 male, 2 female, mean age = 41.8 years [range, 24-59 years]) without known cerebrovascular disease participated in the study.

Three ASL-fMRI scans using pCASL were performed for each volunteer consisting of a blue-and-yellow 8Hz flickering circular checkerboard (for visual stimuli) for 32 seconds alternated with a white fixation cross on a black background for 32 seconds. Volunteers were instructed to also perform a bilateral finger tapping task while the checkerboard was projected. For the first and the last ASL-fMRI scans, volunteers were instructed to move their head during pCASL labeling and/or PLD (not during the readout). For the second ASL-fMRI scan, volunteers were instructed not to move and this scan was used as a reference. After the first ASL-fMRI scan, image data were immediately processed to estimate the motion, so that before the third ASL-fMRI scan the volunteers could be instructed to adjust their degree of motion; we aimed for a few mm and/or degrees of motion. The M_0 scan and was acquired between the first and second ASL-fMRI scans.

All MR scans were performed on a Philips 3.0T Ingenia scanner (Philips, Best, The Netherlands) using a 32-channel head coil. Imaging parameters for SMS-EPI pCASL were as follows: Field of View (FOV) = 240 × 240 mm, scan matrix = 80 × 80, 18 slices acquired with a thickness of 7.0 mm, TE of 16 ms and TR of 4000 ms, and sensitivity-encoding (SENSE) was applied with a factor of 3 in anterior-posterior direction, and the SMS-factor was set to 3. Both labeling duration and PLD were set to 1800 ms. A fat-suppression pre-pulse was applied to avoid water-fat shift artifacts and a WET pre-saturation scheme was inserted before labeling (13,14); BGS pulses were applied using hyperbolic secant pulses (15) at 1830 and 3150 ms after the start of labeling. The timing of the BGS pulses was determined via Bloch simulations. With the number of dynamic scans set to 64, the total scan time was 8:40 min. The M_0 image was acquired without labeling, WET pre-saturation and BGS, but with identical acquisition parameters as the perfusion scan except for the TR, which was set to 2500 ms. Before the quantification process, the M_0 image was multiplied by the factor

$1/(1-\exp(-TR/T_{1_gm}))$, where T_{1_gm} was assumed to be 1200 ms, to correct for incomplete T_1 recovery (8,16).

All three ASL-fMRI datasets were post-processed with the *NewMoCo* framework, and the baseline CBF map was calculated from the β_{perf} map. Moreover, a map which consisted of the t-value of β_{act_perf} was generated to indicate the area where the perfusion changed as a result of the visual and motor tasks. Figure 3 shows an example of the employed design matrix. For the two ASL-fMRI datasets with intentional head movement, *NoMoCo* and *StdMoCo* were also performed for comparison.

On the t-value maps obtained from the ASL-fMRI dataset without intentional head movement, ROIs were manually drawn around the activated visual, and left and right motor area. These ROIs were copied to the t-value maps of the datasets with intentional head movement, and the mean t-values as well as the number of voxels that exhibited a t-value larger than 3.0 were compared between *NewMoCo*, *NoMoCo* and *StdMoCo*. The analysis was performed by a two-way ANOVA followed by multiple comparisons with adjustment of Bonferroni, using SPSS.

Results

Simulation-1: *Comparison of MoCo Estimation*

Figure 4 shows the normalized mean difference of MoCo estimated parameters with *MoCo-A*, *-B*, *-C* and *-D* relative to the reference. For correction of through-plane motion (Figure 4b) *MoCo-A* resulted in the largest mean normalized difference from the reference, which can be attributed to the presence of BGS dark-lines influencing the MoCo estimation. When using the M_0 image as a reference (*MoCo-B*), and homogenization (*MoCo-C*), as well as the combination of these two (*MoCo-D*), the mean normalized difference was much lower. In contrast, for correction of in-plane motion (Figure 4a) differences of MoCo estimation were much smaller for *MoCo-A*, presumably because the presence of BGS dark-lines did not influence the MoCo estimation for in-plane motion. When observing in more detail these results as in the zoomed version of Figure 4c, it becomes clear that *MoCo-B* showed relatively larger mean normalized difference for in-plane motion than the other approaches. It can be speculated that the use of the M_0 image as a reference for registration might introduce small additional errors because of its slightly different contrast as compared to pCASL images.

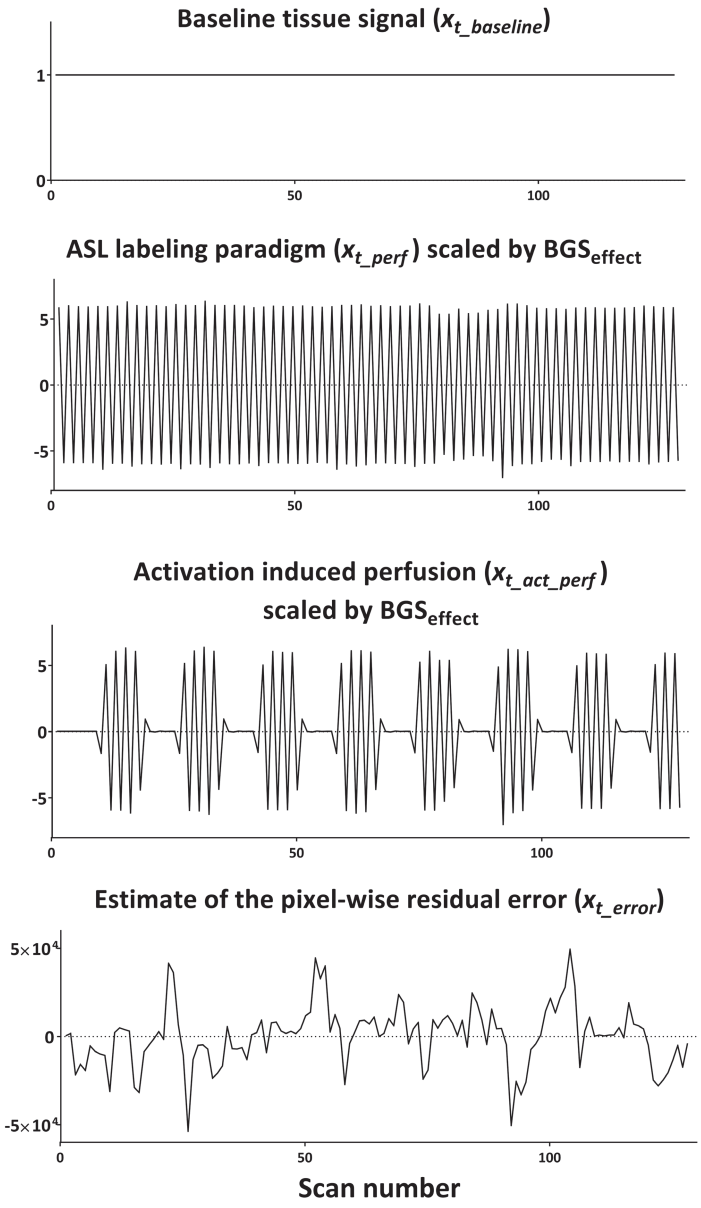


Figure 3: An example of the design matrix employed to the in vivo ASL-fMRI study, in which $x_{t_baseline} = 1$ for baseline tissue signal, x_{t_perf} represents the signal changes as a result of the ASL labeling paradigm, and $x_{t_act_perf}$ describes the ASL signal changes induced by activation. Because the perfusion-weighted signal is scaled by the BGS_{effect} during the homogenization process, x_{t_perf} and $x_{t_act_perf}$ were multiplied by the resliced BGS_{effect} that was generated at the step (ii), to include the pixel by pixel scaling of the perfusion-weighted signal. x_{t_error} represents an estimate of the pixel-wise residual error.

For further simulations (simulation-2, see next section) and the in vivo study, *MoCo-B* and *MoCo-D* were chosen and will be referred to as *StdMoCo* and *NewMoCo*, respectively.

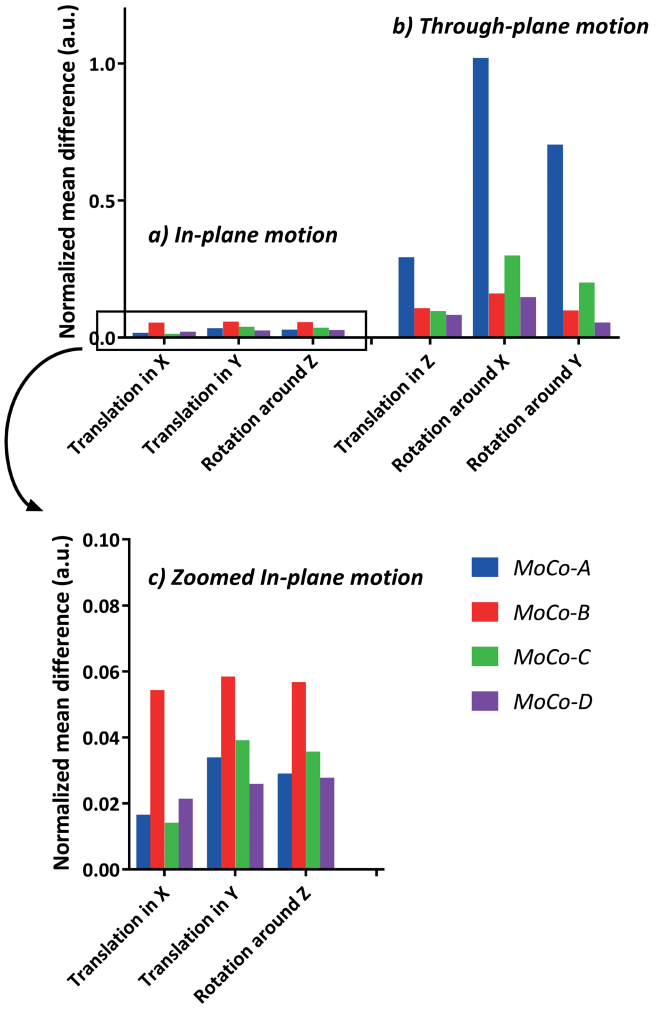


Figure 4: Normalized mean difference of MoCo estimation for (a) in-plane motion, and (b) through-plane motion obtained from simulation-1. In (c) the result of in-plane motion shown in (a) is given in more detail. *MoCo-A:* with BGS dark lines present and the use of the firstly acquired ASL image as reference, *MoCo-B*: with BGS dark lines present and the use of the M_0 image as reference (instead of the firstly acquired ASL image), *M_0Co-C*: with homogenization and the use of the firstly acquired ASL-image as reference, *MoCo-D*: with homogenization and the use of the M_0 image as reference.

Simulation-2: *Separation of Perfusion-Weighted Signal*

Figure 5 illustrates the simulation results from the slice that exhibited the largest difference in static tissue signal intensity compared to a neighboring slice, and therefore most prone to the BGS subtraction errors. In *StdMoCo*, severe BGS subtraction errors were observed for through-plane motion (severe signal increase in the anterior part of the brain in combination with a decrease in signal at the posterior side, as illustrated in Figure 5i), whereas such BGS subtraction errors were not observed in images with in-plane motion (Figure 5e). By use of the *NewMoCo*-approach, the BGS subtraction errors were substantially reduced for through-plane motion (Figure 5f). When employing *NoMoCo*, the presence of in-plane motion appeared as a blurring of the CBF map (Figure 5d). In contrast, for through-plane motion (Figure 5h) such a blurring was less obvious. In both types of motion, however, the conventional subtraction errors (due to motion) were observed clearly along tissue boundaries of the right side of the brain (without perfusion). When removing the error regressor "x_{t_error}" from the design matrix ($NewMoCo_{wo_error_reg}$), a small increase of blurring was observed in the image with through-plane motion, especially along the boundary between gray and white matter (Figure 5g).

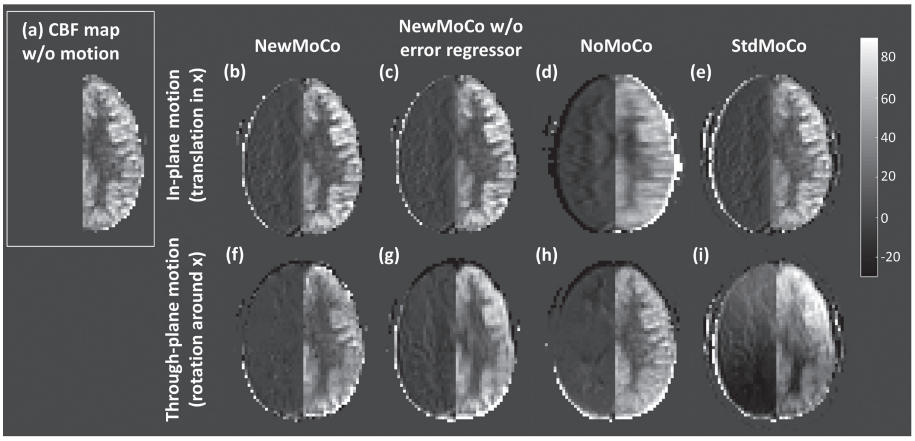


Figure 5: Representative CBF maps obtained from simulation-2. In the right hemisphere, no perfusion signal was simulated, and therefore all signal intensity in the right hemisphere indicates motion-related errors. (a) Reference CBF map obtained from the dataset without motion. (b)-(e) Respectively *NewMoCo*, *NewMoCo* without error regressor, *NoMoCo* and *StdMoCo* are applied to in-plane motion (translation in the x-direction), and (f)-(i) to through-plane motion (rotation around the x-axis).

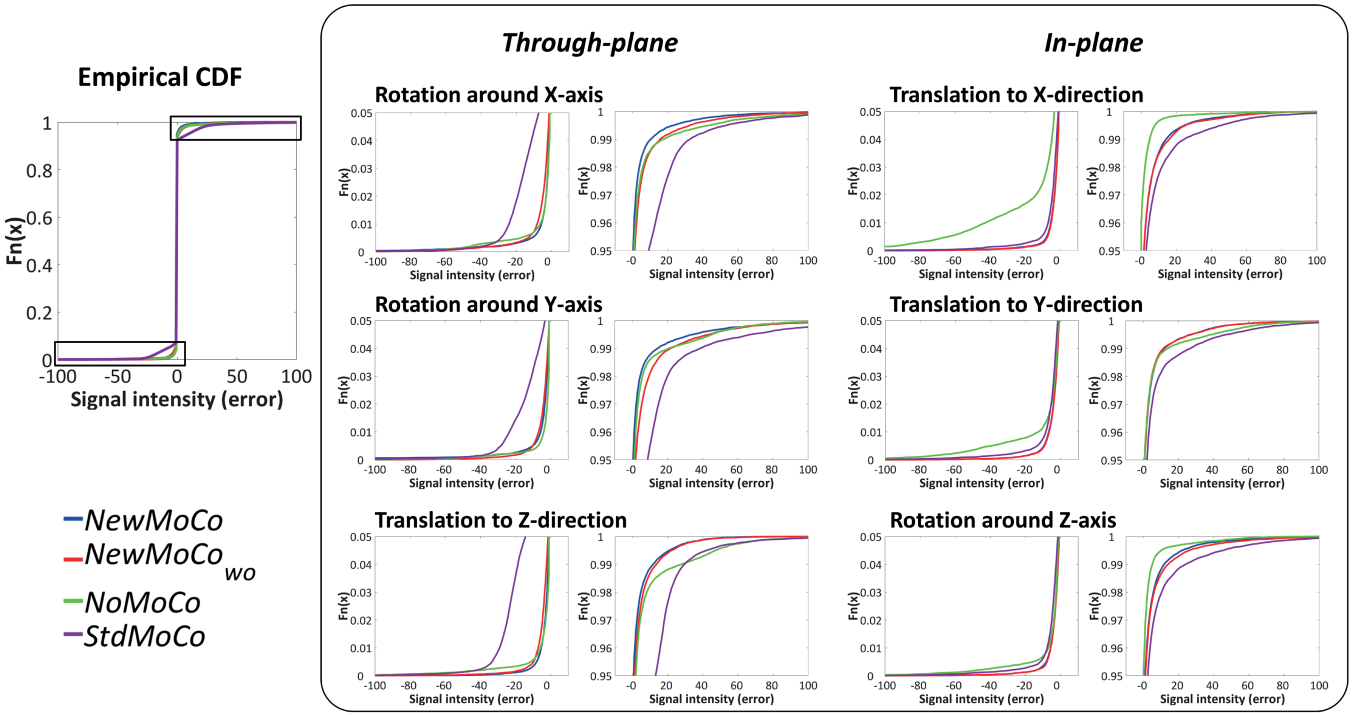


Figure 6: The empirical cumulative distribution function (CDF) of the signal intensity in the right side of the brain (without perfusion) obtained from simulation-2, which indicates the level of artefactual signal that arises mostly from conventional subtraction errors due to motion as well as the above-mentioned BGS subtraction errors. The value is ideally close to zero when both sources of errors are well corrected. For magnified presentation, only plots with the cumulative distribution from 0 to 0.05 and 0.95 to 1.00, and signal intensity between -100 to 100 are shown.

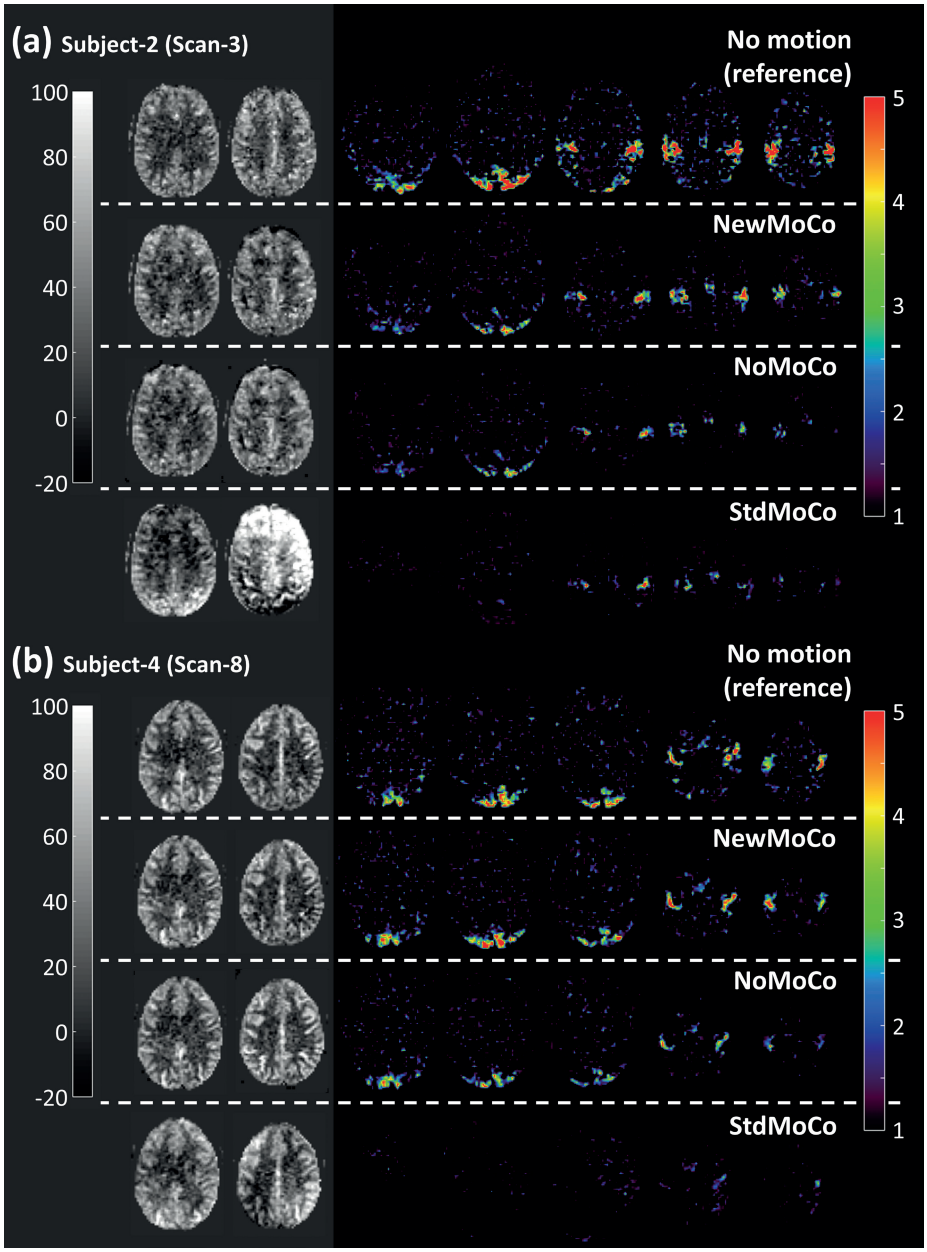


Figure 7: Representative baseline CBF maps and t-value maps showing the activated regions by the visual stimulus and finger tapping obtained from the ASL-fMRI study with intentional head movements processed by *NewMoCo*, *NoMoCo* and *StdMoCo*. As reference, maps acquired without intentional head movement are also shown on top of them.

For a more quantitative observation of the artefactual signal changes, Figure 6 shows the empirical cumulative distribution function (CDF) of the signal intensity in the right side of the brain (without perfusion), in which without any errors present (i.e. all voxels are zero) the empirical CDF would be a step function at zero, whereas significant deviation from this step-function at zero implies the presence of voxels with large errors. (The asymmetry in the empirical CDF between positive and negative signal intensities is attributed to the fact that the signal intensity was analyzed only for one side of the brain.) Similar to the qualitative results as shown in Figure 5, more pixels with signal intensity far from zero were observed as a result of *StdMoCo* applied to data corrupted by through-plane motion, whereas the distribution was closer to the step-function for in-plane motion. For some motion patterns (not clearly divided by the category "through-plane" and "in-plane motion"), *NoMoCo* resulted in mild elevation of artefactual signal, which reflects the blurring as also observed in Figure 5d. With the *NewMoCo*-approach, both types of subtraction errors were substantially reduced independent of the direction of motion.

In Vivo Healthy Volunteer Study

Figure 7 shows representative results of the ASL-fMRI experiments showing the baseline CBF maps as well as the activated regions evoked by the visual stimulus and finger tapping. In the motion corrupted datasets, the activated regions were depicted much more clearly when applying *NewMoCo* as compared to *StdMoCo,* whereas *NoMoCo* provided results in between of these two approaches. The results of the ROI analysis from all volunteers confirmed that the highest mean t-value (Figure 8a) as well as highest number of activated voxels (Figure 8b) were obtained by *NewMoCo*. All differences were statistically significant ($p < 0.05$) except the difference between *NoMoCo* and *StdMoCo* of the number of voxels that exhibited a t-value larger than 3.0.

As baseline CBF maps from all scans show (Figure 9), the BGS subtraction errors on the baseline CBF map were corrected well by *NewMoCo*. For the two datasets with the most severe head-motion (scan-7 from volunteer-4 and scan-1 from volunteer-1), however, correction was not sufficient for slices with the largest BGS difference between neighboring slices, as indicated by red arrows in Figure 9. For the baseline CBF maps, *NoMoCo* generally resulted in reasonable image quality without BGS subtraction errors, although some blurring can be observed. The estimated motion parameters from all volunteers are shown in Figure 10.

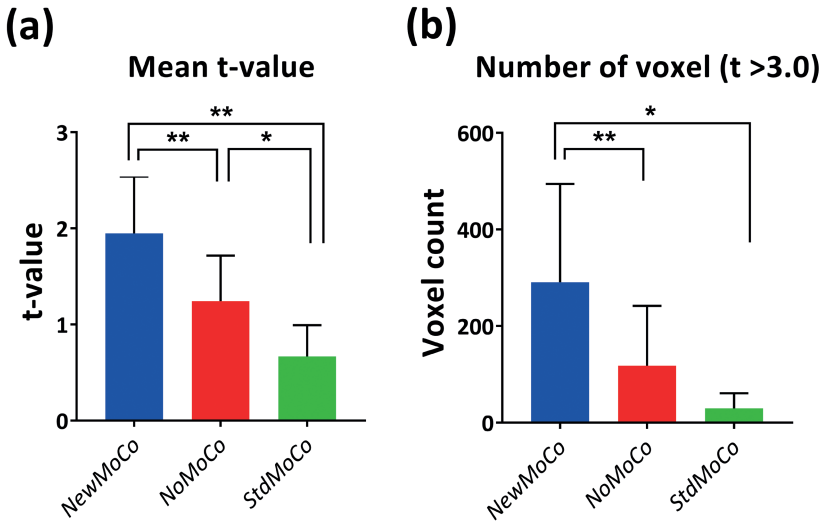


Figure 8: The results of the ROI analysis. (a) the mean t-values, and (b) the number of voxels that exhibited a t-value larger than 3.0 from dataset processed by *NewMoCo*, *NoMoCo* and *StdMoCo* as well as dataset obtained without intentional head movement for reference.

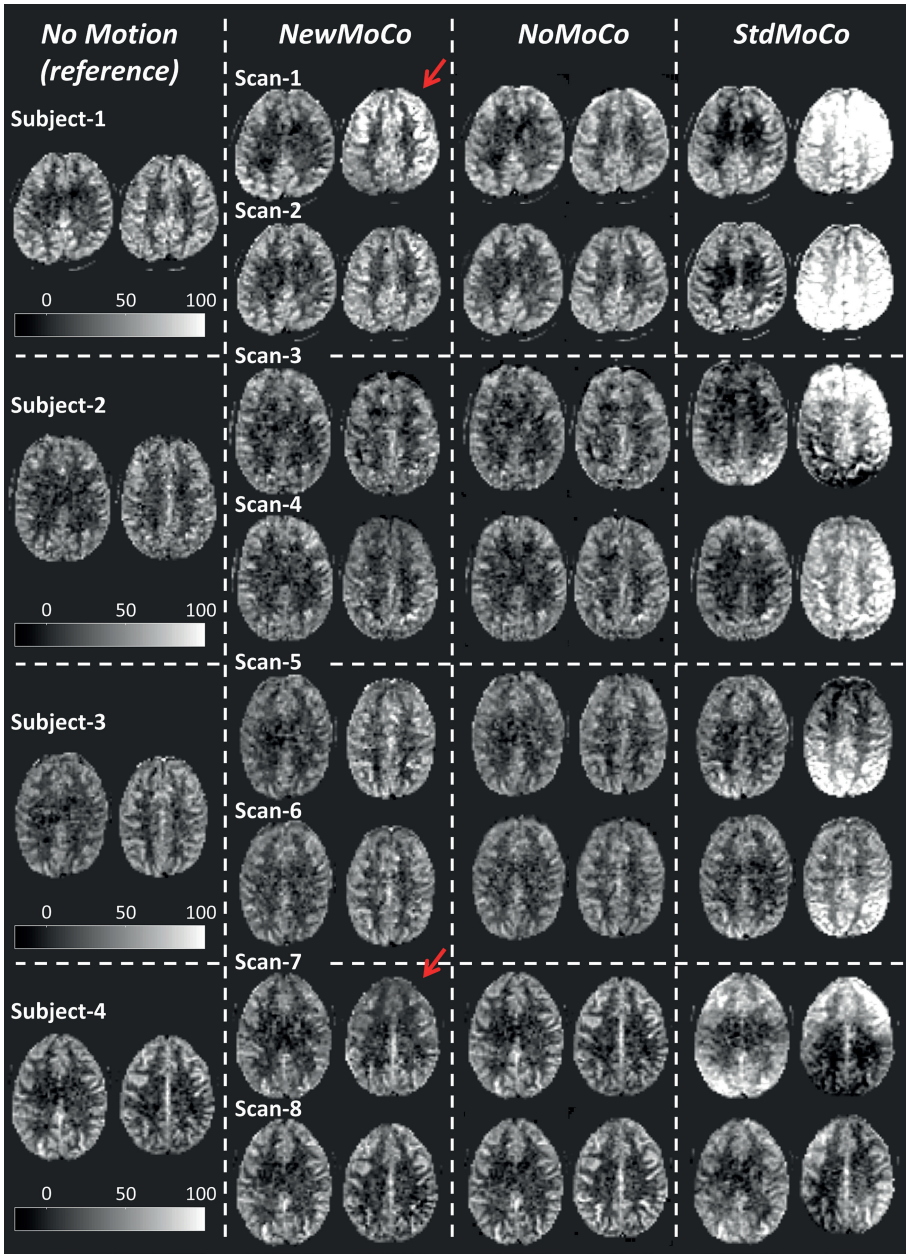


Figure 9: The baseline CBF maps from all scans, showing two slices with largest difference of BGS efficiency from the neighboring slices. Red arrows indicate the residual error from two scans with the most severe head-motion.

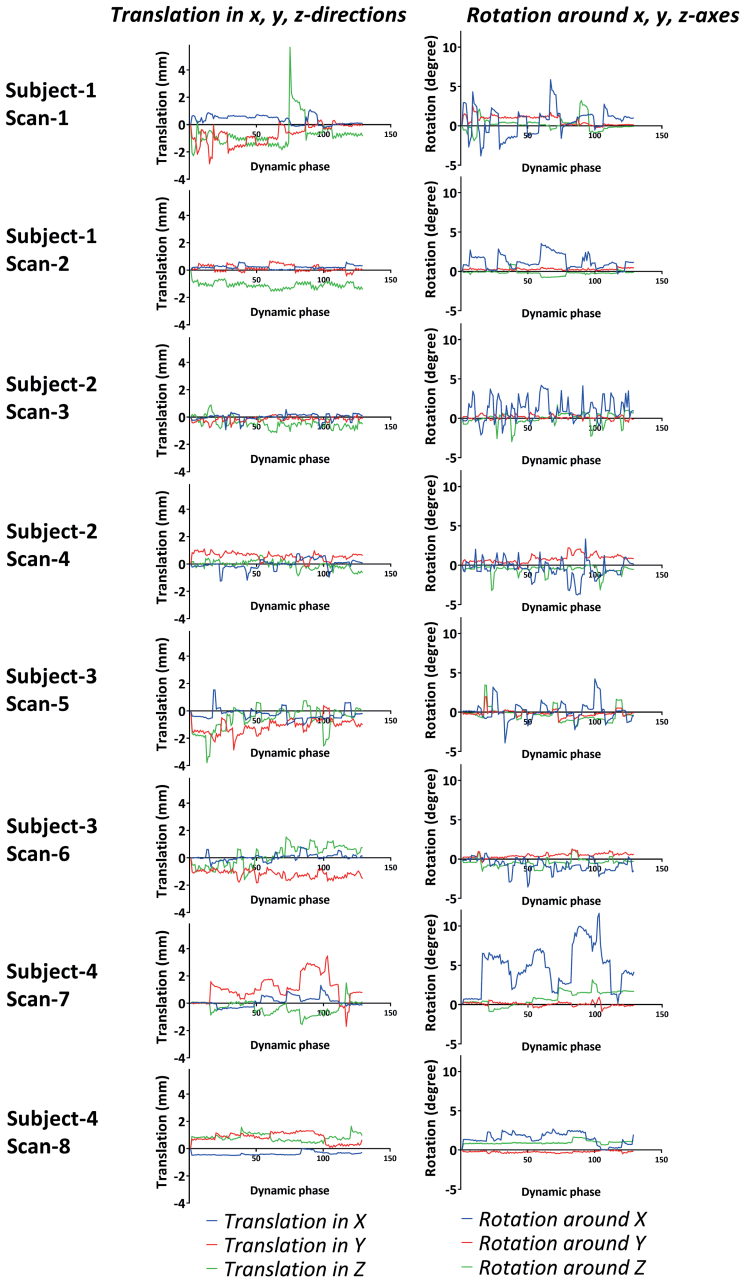


Figure 10: Estimated motion parameters of all scans.

Discussion

In this article, we demonstrated two major issues that can affect ASL measurements when using a 2D multi-slice readout with SMS and BGS: suboptimal estimation of motion parameters by MoCo and the occurrence of BGS subtraction errors, which can be very severe. Our simulation studies showed that these problems predominantly occur when through-plane motion (translation in z-direction, or rotation around the x- or y-axes) is present, pointing to the large influence of the BGS dark-lines. Although MoCo estimation was already improved to a great extent by the use of the M_0 image as the reference for MoCo registration, successful realignment still led to BGS subtraction errors in the perfusion-weighted signal, as was also evident in the ASL-fMRI study. By use of our proposed framework, the BGS subtraction errors were minimized and the depiction of activated regions was improved, while still allowing the use of conventional MoCo methodology as available in commonly applied neuroscience software. The benefit of our framework was most obvious in the ASL-fMRI experiments, in which application of MoCo is especially important to detect statistically significant activation from small regions of interest.

In general, MoCo methods such as those implemented in SPM and FSL estimate motion parameters based upon an error-measure calculated from the similarity between images. Therefore, strong contrast as imposed by the BGS dark-lines could overwhelm differences as a result of anatomical misalignment and cause an erroneous estimation of motion parameters. By using the M_0 image, which does not exhibit BGS dark-lines, as the reference image for MoCo estimation, the MoCo will not be biased due to a tendency to keep BGS dark-lines aligned and will therefore be better able to pick up the real motion and thus improve the MoCo estimation. This was found to be true for through plane motion, both with and without homogenization. However, for in-plane motion, the use of M_0 image as a reference resulted in slightly poorer performance when homogenization had not been applied, although to an extent that was much smaller than the improvement for through-plane motion. The poorer performance of the M_0-approach (*MoCo-B*) for in-plane motion can most probably be attributed to the difference in contrast between the M_0 and BGS-pCASL images. The improvement observed by combining the M_0-approach with the homogenization (*MoCo-D*) reinforces this argument, in which further reduction of the normalized mean difference was achieved for all types of motion.

The source of subtraction errors as identified in this study can be categorized into two groups: the first type of errors are conventional subtraction errors occurring when anatomical structures are not stable at the same location as a result of

inaccurate motion estimation due to BGS dark-lines (or when MoCo is not applied), i.e. the 'normal' type of motion artefacts. One important target of BGS is to minimize this type of subtraction error by lowering the signal intensity of static tissue (8). In multi-slice ASL, however, even when SMS is applied, multiple excitation pulses will still be needed and the level of BGS will not be optimal in all (sets of) slices, thereby increasing the severity of these subtraction errors. In our experiments such artefacts can be observed in the *NoMoCo* data (i.e. subtraction without applying motion correction).

The second type of error arises from subtraction of signals with different levels of BGS (BGS subtraction error). These errors are evident in the *StdMoCo* data in which MoCo does assure that anatomical structures are realigned, although signal intensity differences of static tissue result in artefacts due to the fact that an anatomical structure was part of a different slice during the label versus the control condition (e.g. a certain anatomical structure moves from a location with optimal BGS for the control acquisition to a position with lower BGS efficiency during the label condition). We propose to eliminate this second type of subtraction errors by homogenization of the static tissue signal over slices before MoCo is performed. This homogenization is, however, only performed by equalizing the mean signal of a slice relative to the mean signal of the same slice of the M_0 image. This implies that at the level of individual pixels this homogenization will not be perfect and residual BGS subtraction errors can still occur. To minimize such residual errors, the use of a GLM was proposed with additional regressors, besides a subtraction-regressor that extracts the perfusion-weighted signal from the unsubtracted ASL data. In this study, we employed the subtracted pixel value of the homogenized ASL data before and after MoCo as an additional regressor. This metric is a measure of static tissue signal change after MoCo reslicing, which is the main cause of BGS subtraction errors. In the simulation study, the calculated CBF map showed increased errors along the boundary between gray and white matter when applying *NewMoCo* without this error regressor, which most likely represents residual BGS subtraction errors.

It should be noted that, as Figure 9 shows, when the motion was very large *NewMoCo* could fail to generate reliable baseline CBF maps at the slices with the largest difference in BGS between neighboring slices (at the BGS dark-lines), and *NoMoCo* resulted in better quality. When ASL is performed for clinical diagnostic purposes, the main goal will be to achieve high quality resting-state baseline CBF map, in which some motion-blurring can be tolerated. Therefore, performing both *NewMoCo* and *NoMoCo* would be recommended to avoid potential misinterpretation due to residual BGS subtraction errors on the CBF map as obtained by *NewMoCo*. However, when

functional ASL is performed, small location changes might result in one becoming blind for the brain activation, thereby making MoCo more essential. In fact, the ROI analysis performed on the ASL-fMRI scans resulted in higher mean t-value and higher number of activated voxels by *NewMoCo* than *NoMoCo* for *all* 8 scans.

Another approach to avoid BGS subtraction errors would be to limit the inter-slice BGS signal differences by changing the acquisition. Such an approach was proposed recently by Shao et al via a slice-dependent signal preparation, i.e. pre-saturation is not performed at a single moment in time for all slices, but slice-dependent preparation pulses are applied to ensure optimal BGS for each slice (6). With this approach, the largest differences in signal intensity of static tissue between neighboring slices can be avoided, thereby lowering the risk for the most severe subtraction artefacts, although not excluding these completely. Moreover, when motion occurs between the saturation module and readout, i.e. including the labeling duration and PLD, the carefully optimized scheme could be affected and inter-slice signal differences could appear. Therefore, it would be interesting to see whether the currently proposed approach would also improve motion-corrupted SMS-ASL data acquired with the slice-dependent pre-modulation approach. It could be expected that both approaches would enhance each other's performance.

Several limitations of the current study should be mentioned. First of all, the most important message of this article is to demonstrate the issues that could be introduced by combined use of SMS and BGS in an ASL study. Although we employed the subtraction of pixel values before and after MoCo of the homogenized ASL data as an additional error regressor, it does not mean that we can assure that this is the most optimal regressor. In fact, as discussed above, there is certainly room for further improvements when severe motion is present, especially for the baseline CBF maps. Secondly, the proposed method does not correct for other well-known sources of artefacts in motion corrupted MRI data. For example, distortions due to B_0 inhomogeneities and residual water-fat shift artifacts (even though fat suppression was applied) are dependent on the head orientation and can thus change during head-motion. Therefore, after MoCo realignment, such artifacts will be repositioned to different locations, again resulting in subtraction errors. In this study, only rigid-body MoCo was applied, which cannot correct for such artifacts. Moreover, motion that happened during the readout might introduce additional artifacts that cannot be corrected by rigid-body MoCo. In future work, further investigation of even more appropriate regressors and application of more advanced MoCo approaches should be studied.

Conclusion

In ASL with combined use of SMS and BGS, severe BGS subtraction errors can occur when through-plane motion is corrected by traditional MoCo procedures. With the proposed framework, these BGS subtraction errors can be minimized, resulting in improved accuracy of CBF estimation while still allowing the use of conventional MoCo approaches as available in widely used software packages.

Acknowledgements

This research was supported by the EU under the Horizon2020 program (project: CDS-QUAMRI, project number 634541). The authors thank Prof. Aart J. Nederveen and Dennis F.R. Heijtel, PhD, the department of Radiology and Nuclear Medicine of the Amsterdam Medical Center (Amsterdam, The Netherlands) for providing the volunteer dataset as employed in the simulations study. MC received funding from the EPSRC UK (EP/P012361/1). TO is funded by the UK Royal Academy of Engineering. The Wellcome Centre for Integrative Neuroimaging is supported by core funding from the Wellcome Trust (203139/Z/16/Z).

References

1. Moeller S, Yacoub E, Olman CA, Auerbach E, Strupp J, Harel N, Ugurbil K. Multiband multislice GE-EPI at 7 tesla, with 16-fold acceleration using partial parallel imaging with application to high spatial and temporal whole-brain fMRI. Magn Reson Med 2010;63(5):1144-1153.
2. Setsompop K, Gagoski BA, Polimeni JR, Witzel T, Wedeen VJ, Wald LL. Blipped-controlled aliasing in parallel imaging for simultaneous multislice echo planar imaging with reduced g-factor penalty. Magn Reson Med 2012;67(5):1210-1224.
3. Feinberg DA, Moeller S, Smith SM, Auerbach E, Ramanna S, Gunther M, Glasser MF, Miller KL, Ugurbil K, Yacoub E. Multiplexed echo planar imaging for sub-second whole brain FMRI and fast diffusion imaging. PLoS One 2010;5(12):e15710.
4. Zhang K, Yun SD, Shah NJ. Tripled Readout Slices in Multi Time-Point pCASL Using Multiband Look-Locker EPI. PLoS One 2015;10(11):e0141108.
5. Feinberg DA, Beckett A, Chen L. Arterial spin labeling with simultaneous multi-slice echo planar imaging. Magn Reson Med 2013;70(6):1500-1506.
6. Shao X, Wang Y, Moeller S, Wang DJ. A constrained slice-dependent background suppression scheme for simultaneous multislice pseudo-continuous arterial spin labeling. Magn Reson Med 2017.
7. Kim T, Shin W, Zhao T, Beall EB, Lowe MJ, Bae KT. Whole brain perfusion measurements using arterial spin labeling with multiband acquisition. Magn Reson Med 2013;70(6):1653-1661.
8. Alsop DC, Detre JA, Golay X, Gunther M, Hendrikse J, Hernandez-Garcia L, Lu H, MacIntosh BJ, Parkes LM, Smits M, van Osch MJ, Wang DJ, Wong EC, Zaharchuk G. Recommended implementation of arterial spin-labeled perfusion MRI for clinical applications: A consensus of the ISMRM perfusion study group and the European consortium for ASL in dementia. Magn Reson Med 2015;73(1):102-116.
9. Ivanov D, Poser BA, Huber L, Pfeuffer J, Uludag K. Optimization of simultaneous multislice EPI for concurrent functional perfusion and BOLD signal measurements at 7T. Magn Reson Med 2017;78(1):121-129.
10. Ashburner J, Friston K. CHAPTER 4 - Rigid Body Registration. Statistical Parametric Mapping. London: Academic Press; 2007. p 49-62.
11. Jenkinson M, Bannister P, Brady M, Smith S. Improved optimization for the robust and accurate linear registration and motion correction of brain images. Neuroimage 2002;17(2):825-841.
12. Heijtel DF, Mutsaerts HJ, Bakker E, Schober P, Stevens MF, Petersen ET, van Berckel BN, Majoie CB, Booij J, van Osch MJ, Vanbavel E, Boellaard R, Lammertsma AA, Nederveen AJ. Accuracy and precision of pseudo-continuous arterial spin labeling perfusion during baseline and hypercapnia: a head-to-head comparison with ^{15}O H_2O positron emission tomography. Neuroimage 2014;92:182-192.
13. Ogg RJ, Kingsley PB, Taylor JS. WET, a T1- and B1-insensitive water-suppression method for in vivo localized 1H NMR spectroscopy. J Magn Reson B 1994;104(1):1-10.
14. Golay X, Petersen ET, Hui F. Pulsed star labeling of arterial regions (PULSAR): a robust regional perfusion technique for high field imaging. Magn Reson Med 2005;53(1):15-21.
15. Silver MS, Joseph RI, Hoult DI. Selective spin inversion in nuclear magnetic resonance and coherent optics through an exact solution of the Bloch-Riccati equation. Phys Rev A Gen Phys 1985;31(4):2753-2755.
16. Lu H, Nagae-Poetscher LM, Golay X, Lin D, Pomper M, van Zijl PC. Routine clinical brain MRI sequences for use at 3.0 Tesla. J Magn Reson Imaging 2005;22(1):13-22.

Chapter 7

Summary and general discussion

In this doctoral thesis, several new techniques for dynamic MR angiography (4D-MRA) and perfusion imaging were developed based on different Arterial Spin Labeling (ASL) techniques, which include pulsed ASL (PASL), pseudo-continuous ASL (pCASL), vessel-encoded (ve) pCASL, time-encoded (te) pCASL as well as simultaneous multi-slice (SMS) pCASL. The underlying motivation of these developments is to reduce the burden on patients by employing non-invasive ASL techniques as potential alternatives to X-ray digital subtraction angiography, contrast-enhanced MRA and perfusion imaging. In each study, the optimum ASL technique was carefully chosen by considering the pros and cons of the technique to achieve better clinical usability, while improving robustness against potential artifacts.

In chapter 2, a novel accelerated time-resolved ASL-MRA technique, ACTRESS, was presented by using PASL. In the ACTRESS approach, a single control image is acquired before the labeling pulse in a Look-Locker multi-delay readout, and this single phase control image is subtracted from the other labeled images acquired with the multi-delay readout. It means that only a single Look-Locker readout is required for the acquisition of both labeled and control images, instead of separate pair-wise acquisitions, thereby reducing the scan time by close to a factor of two as compared to the conventional ASL-based 4D-MRA. To achieve similar image quality to conventional 4D-MRA, optimization of the labeling pulse was carefully performed. Qualitative assessment demonstrated that ACTRESS-MRA could generate 4D-MRA with similar image quality to conventional ASL-based 4D-MRA.

In chapter 3, ve-pCASL was employed to achieve vessel-selective 4D-MRA. It was determined how changes in the gradient settings for pCASL labeling influence the spatial modulation of the inversion profile, and optimizations were performed to achieve a narrower labeling condition, a broader and flatter control condition and a sharper transition between the two conditions. The optimized settings enabled 4D-MRA acquisition by using four Hadamard encodings, instead of eight Hadamard encodings previously proposed in the literature, which means half the scan time compared to this previous study. It was also shown that the use of these new settings lowered the risk of partial labeling of untargeted arteries.

Additionally, in chapter 4, we have presented a combination of vessel-selective pCASL and ACTRESS. By employing pCASL for vessel-selective labeling, instead of PASL as used in the original ACTRESS approach proposed in chapter 2, signal elevation of the static tissue resulting from the intersection of the labeling slab and the imaging volume could be avoided. Moreover, separate visualization of the internal and external carotid arteries could be achieved, which is difficult for PASL because a PASL

labeling slab with its large coverage will also label arterial blood in the common carotid artery that feeds both the internal and external carotid arteries. Application of a pre-saturation pulse and the use of optimized parameter settings minimized the static tissue signal fluctuations over the Look-Locker readout, which is essential to avoid elevated background signal that could hinder the visualization of small arteries. This approach allowed vessel-specific visualization of 4D-MRA with very short scan time of 2 – 3 minutes, which will improve the clinical usability dramatically.

In chapter 5, simultaneous acquisition of perfusion and 4D-MRA was proposed by using te-pCASL, in which an optimized labeling duration of each subbolus provided sufficient labeling duration and PLD for perfusion imaging, as well as sufficient temporal resolution to depict the early arterial phase in 4D-MRA. Moreover, reduction of the saturation effects caused by the MRA readout on the perfusion image was achieved not only by using te-pCASL instead of the conventional Look-Locker readout, but also by using relatively low excitation flip angles and a segmented EPI readout inserted after each excitation pulse. These advanced sequence designs allowed the additional acquisition of 4D-MRA within a typical pCASL perfusion imaging scan time, while maintaining sufficient image quality of the perfusion CBF maps.

In chapter 6, an important pitfall of ASL perfusion imaging when combined with SMS and background suppression (BGS) was reported, in which severe subtraction errors can occur when through-plane motion is corrected by traditional motion correction procedures. A new framework was proposed to correct such subtraction errors, which results in improved accuracy of CBF estimation while still allowing the use of conventional motion correction approaches as available in widely used software packages.

ASL-based 4D-MRA technique for clinical examination

As stated in several chapters, one of the advantages of ASL-based 4D-MRA is that both higher spatial and temporal resolution can be obtained compared to contrast-enhanced 4D-MRA. However, the scan time tends to become longer. When aiming for development of techniques for clinical examinations, it is important to be reminded that many MR examinations have time restrictions due to, e.g. fully booked MR scanners and the finite ability of patients to keep still during the examination. Therefore, keeping the scan time short is one of the most important factors to be considered for a successful introduction of new MRI sequences. At the same time, there is another factor that should be considered about clinical examinations: the condition of patients is not always ideal to obtain the best image quality. For example, patients could be more prone to move during scans. Moreover for ASL techniques, slow blood flow as associated with certain diseases tends to result in poor depiction

of flow, sometimes even poorer than the actual flow reduction, thereby causing underestimation or misinterpretation. Therefore, although reduction of scan time may reduce the risk of patient motion, careful optimizations should be done so that the reduction of scan time would not result in a compromise for reliable diagnosis. For example, in the ACTRESS approach as presented in chapter 2, we achieved a reduction of scan time to nearly half of that of the conventional ASL-based 4D-MRA, while avoiding artifacts due to off-resonance effects by optimizing the labeling pulse. However, there is a remaining concern for the patient scans: in ACTRESS approach, it is very important that the control image acquired in the first phase does not contain residual labeled blood from the previous Look-Locker readout cycle. Otherwise, remaining labeled blood in the control image would cancel the ASL signal in those arteries. In the healthy volunteer study, such lowered visualization of arteries with slow flow, such as occipital artery, was minimized by setting a sufficiently long duration of the total Look-Locker readout cycle. However, for patients with even slower or/and delayed flow, special attention is required to use adequate parameter settings for proper diagnosis.

For successful clinical implementation with shorter scan time while avoiding a decrease in diagnostic reliability, such as in the above described example of ACTRESS, a close collaboration with people working in the clinical environment is essential: they have the expert knowledge on what they need, what are essential requirements for diagnosis, and what could be compromised without affecting the clinical usability. In fact, such a collaboration motivated some of studies in this thesis and provided direction to them. Further collaboration is desirable so that the newly proposed techniques in this thesis will be applied to clinical examinations and thereby provide helpful information for diagnosis.

Possible avenues for future research

The application of ASL-based 4D-MRA can be useful for several cerebrovascular diseases, such as arteriovenous malformation (AVM), arteriovenous fistula (AVF) and steno-occlusive disease including Moyamoya disease. Temporal information obtained by 4D-MRA could provide insight about the flow velocity and existence of retrograde flow. Vessel-selective visualization could help to identify the feeding artery of pathology and to assess the function of a bypass artery. Such information could be obtained by using the techniques with relatively short scan time that were developed and optimized in this thesis. However, what is also clinically important but could not be achieved within the context of this thesis projects is improved visualization of even more peripheral arteries with even slower arrival. For example, velocity-selective labeling (1-3) could help an improved visualization of peripheral

arteries because the labeling can be applied within these arteries or at least much closer to these peripheral vessels. However, further investigation will be necessary to achieve 4D visualization of inflowing blood.

Also, temporal information obtained by 4D-MRA in this thesis was solely used for visualization, although it could also provide *quantitative* information by using appropriate post-processing, such as kinetic models (4). In the simultaneous acquisition of 4D-MRA and perfusion imaging as presented in chapter 5, there is further potential not only via complementary visual interpretation of macrovascular and microvascular ASL images, but also by calculating additional quantitative measures by combining both measurements.

References

1. Norris DG, Schwarzbauer C. Velocity selective radiofrequency pulse trains. J Magn Reson 1999;137(1):231-236.
2. Wong EC, Cronin M, Wu WC, Inglis B, Frank LR, Liu TT. Velocity-selective arterial spin labeling. Magnetic Resonance in Medicine 2006;55(6):1334-1341.
3. Qin Q, Shin T, Schar M, Guo H, Chen HW, Qiao Y. Velocity-selective magnetization-prepared non-contrast-enhanced cerebral MR angiography at 3 Tesla: Improved immunity to B0/B1 inhomogeneity. Magnetic Resonance in Medicine 2016;75(3):1232-1241.
4. Okell TW, Chappell MA, Schulz UG, Jezzard P. A kinetic model for vessel-encoded dynamic angiography with arterial spin labeling. Magn Reson Med 2012;68(3):969-979.

7

Nederlandse samenvatting

Dit proefschrift beschrijft de ontwikkeling van diverse nieuwe MRI technieken voor het verbeteren van dynamische angiografische MRI en/of MR perfusiebeelden. Deze technieken zijn gebaseerd op de generieke techniek van “arteriele spin labeling” (ASL) MRI en meer specifiek maken zij gebruik van de varianten puls ASL (PASL), pseudo-continue ASL (pCASL), vaat-encryptie pCASL (ve-pCASL), tijdencryptie (te) pCASL en simultane multi-slice (SMS) pCASL. De motivatie om deze technieken te ontwikkelingen komt voort uit de wens om de belasting voor de patiënt te verminderen door deze niet-invasieve technieken te gebruiken als alternatief voor invasieve en in meer-of-mindere mate risicodragende technieken, zoals digitale subtractie angiografie, contrastmiddel MR angiografie en contrastmiddel perfusiemetingen. De keuze en instellingen van elk van deze nieuwe technieken zijn zorgvuldig gekozen en geoptimaliseerd om succesvol gebruik in de kliniek mogelijk te maken, met name door de robuustheid en onderdrukking van potentiële artefacten te verbeteren.

In Hoofdstuk 2 wordt een nieuwe dynamische ASL MR angiografie (MRA) sequentie, genaamd ACTRESS, voorgesteld die gebaseerd is op PASL en een verkorting van de scantijd mogelijk maakt. De ACTRESS-techniek is gebaseerd op het opnemen van slechts een controle beeld, welke wordt opgenomen direct vóór de labeling pulse waarna een Look-Locker uitleesreeks volgt die de meerdere dynamische label beelden opneemt. Vervolgens worden door het aftrekken van dit ene controle beeld van de serie label beelden de angiografische beelden gereconstrueerd. Dit betekent dat maar een enkel controle beeld nodig is in plaats van de gebruikelijke paarsgewijze label/control opnamen, wat vrijwel tot een halvering van de scantijd leidt vergeleken met de standaard 4D-MRA opname. Om gelijkwaardige kwaliteit beelden te verkrijgen was het echter noodzakelijk om de labeling puls te optimaliseren. Door middel van het scoren van de kwaliteit van de ACTRESS-beelden vergeleken met de standaard 4D-MRA opname, werd aangetoond dat deze twee scans vergelijkbare kwaliteit opleveren.

In Hoofdstuk 3 wordt ve-pCASL ingezet om vaat-specifieke (vs) 4D-MRA opnames mogelijk te maken. Om dit te bereiken werd bepaald hoe de instellingen van de pCASL labeling, en dan met name de instellingen van de gradiënt, de overgang van het spatiële inversie profiel beïnvloeden, dus hoe scherp de overgang tussen de label en de controle conditie is en over welke afstand deze twee condities optreden. Door deze optimalisatie kon een scherpere overgang en een bredere en vlakkere controle conditie bereikt worden. Door het inzetten van deze optimale instellingen was het voldoende om een 4-Hadamard encryptie te gebruiken in plaats van de 8-Hadamard,

zoals eerder beschreven in de literatuur. Hierdoor halveert de benodigde scantijd. Daarnaast werd door deze nieuwe instellingen het risico om ongewild ook andere vaten te labelen verkleind.

Vervolgens wordt in Hoofdstuk 4 beschreven hoe vs-pCASL gecombineerd kan worden met de ACTRESS-methode. Door pCASL te gebruiken om vaat-specificiteit te bereiken, in plaats van PASL waarop de oorspronkelijke ACTRESS-methode van Hoofdstuk 2 gebaseerd is, kunnen ongewilde signaal-fluctuaties in het afbeeldingsvlak worden voorkomen, die ontstaan wanneer het labelingsvolume dit vlak zou doorsnijden. Ook geeft pCASL meer mogelijkheden dan vs-PASL om een specifieke afbeelding van de carotis interna te bereiken zonder dat ook de carotis externa wordt afgebeeld. Voor PASL is dit laatste moeilijk omdat de grote reikwijdte van het PASL-labeling volume ook tot labeling van de arteria carotis communis zou leiden welke zowel de carotis interna als de externa voedt. Door het gebruik van een saturatie-puls voor de pCASL-labeling en het gebruik van optimale instellingen van de gehele sequentie, konden de signaal-fluctuaties over de Look-Locker uitleestrein beperkt worden. Dit is essentieel om subtractiefouten te voorkomen, welke zouden leiden tot meer signaal in de achtergrond hetgeen de zichtbaarheid van kleine, perifere vaten beperkt. Met deze verbeteringen is het mogelijk om met een scantijd van slechts 2-3 minuten vaat-specifieke MRA scans te maken, wat de klinische bruikbaarheid sterk doet toenemen.

In Hoofdstuk 5 wordt een gecombineerde opname van perfusie en 4D-MRA voorgesteld. Door te-pCASL te gebruiken waarvan het eerste labeling blok een voldoende duur van de labeling combineert met een relatief lange wachttijd tot het moment van afbeelden worden correcte perfusiemetingen verkregen. De overige blokken van de te-pCASL hebben een veel kortere labelingsduur en wachttijd om een voldoende tijdsresolutie voor de 4D-MRA te bewerkstelligen waarbij ook de vroege, arteriële fase goed wordt afgebeeld. Het minimaliseren van de saturatie-effecten van de MRA uitlezing op de perfusiebeelden, werd niet alleen bereikt door het gebruik van te-pCASL in plaats van een traditionele Look-Locker uitlezing, maar ook door gebruik te maken van kleinere fliphoeken en een gesegmenteerde EPI-uitlezing voor de 4D-MRA data. Door deze aanpassingen aan de scan werd het mogelijk om een 4D-MRA als extra informatie op te nemen tijdens een perfusiescan, terwijl de kwaliteit van die perfusiebeelden in tact blijft.

In Hoofdstuk 6 wordt een belangrijke valkuil van ASL beschreven, welke kan optreden wanneer SMS gebruikt wordt tijdens de uitlezing van een ASL-scan met achtergrond-onderdrukking. Ernstige subtractiefouten kunnen namelijk optreden wanneer beweging in de plak-selectie richting plaatsvindt en normale correctiemethodes op

de data worden toegepast. Een nieuwe uitwerkmethodiek wordt in dit hoofdstuk voorgesteld om dergelijke subtractiefouten te voorkomen, terwijl nog steeds de gebruikelijke public-domain software voor bewegingscorrectie toegepast kan worden.

Acknowledgements

All the work during my PhD could not have been achieved without a huge support from my co-supervisor, Prof. Matthias (Thijs) van Osch. He always found time to help me out: particularly during the last six months whilst I was finishing two manuscripts, managing a new project for ISMRM, writing the thesis and getting a new job at the same time. I could never have managed it without him. And, I always enjoyed my discussions with him: usually just dropping by his room, sometimes bugging him several times in a single day, and always being inspired at the end. Now I have left LUMC, I really miss it very much. Also, I would like to thank to my supervisor, Prof. Andrew Webb for encouraging me to finish my PhD earlier, considering my previous career.

It was extremely lucky for me that I could meet Dr. Thomas (Tom) Okell during my PhD. He welcomed me into his physics group as a visiting student, and since then has always helped me and been most kind and friendly. I am very grateful for the fruitful collaboration with him, which encouraged me to pursue further career in Europe.

I would not be here now without Dr. Marc Van Cauteren, my former supervisor in Philips, who provided me with a chance for a position as a clinical scientist regardless of my academic degree (I only had a bachelor's degree). He never failed to answer my thousands of questions, and I would like to proudly say that he made me who I am today. He was always very supportive and gave me a lot of opportunities for my growth. As a result I was inspired to pursue a career in academia, but he sent me off with warm encouragement. Also, I want to thank all of my former colleagues. I still think of the days when we worked together, which makes me feel encouraged.

My love of Arterial Spin Labeling started during the time I was visiting Dr. Noriyuki Fujima and Dr. Hiroyuki Sugimori at Hokkaido University, with Mr. Akira Suwa. We had a lot of discussions and experiments, often until late at night, and their professional opinions always inspired me. Dr. Fujima still gives me insightful suggestions, which help bridge my technical knowledge with the clinical requirements. When I joined LUMC, I wished that one day I could help their research and diagnostic work through my newly obtained knowledge and experience. Although this has not yet been achieved, it has been one of my biggest motivators.

I would also like to thank Prof. Michael Chappell for a fruitful research collaboration, for providing me with a new challenge in the post-processing field and for giving me a chance to work with and learn from him in Oxford.

During my PhD I was very happy to share the office room with Nathalie, Thomas and Wyger: Nathalie passed on to me a lot of knowledge and advice, which were extremely helpful for finishing/submitting/printing my thesis and preparing for the defence. She was also very supportive in many ways during the job-hunting. Thomas knew everything about LUMC and the PhD system (even though he joined LUMC on the same day as I did), and answered all my questions. He also had excellent taste in chocolate, which completely matched my own. Wyger was always very kind and friendly, and impressed me with his wide knowledge of MRI sequences. I would also like to thank the whole group from the C.J.Gorter Center.

I have to confess that I might have failed to get the position at the University of Oxford without a lot of help from Kate, my English teacher. For me she was not just a great English teacher: I was always consoled very much by her friendly and warm encouraging words (and her Periwinkle), especially when I was nervous by job-hunting.

Also, I want to send huge thanks to Rita, a good friend of mine. Even during the difficult moments in my PhD, she always listened to me and cared about me and her warm empathy always soothed me. And, I am always motivated by her success in academia after the transition from the industry.

Finally, I would like to thank my family, for supporting me, caring about me and always believing in me. It's so comforting to know that you are always there for me.

Curriculum vitae

Yuriko Suzuki was born on August 10th 1977 in Ibaraki, Japan. After graduating from Mito First High School, she studied Physics at Meiji University and obtained her bachelor's degree in 2000 with her academic dissertation "Simulating neuronal firing with the Hodgkin-Huxley model". Immediately after graduating, she joined Philips Medical Systems as a MR Application Specialist. In 2002, she obtained an opportunity of an internship at Philips head office in Best, the Netherlands. From 2004, she continued her career in Philips as a MR Clinical Scientist and experienced many collaborative research projects in areas such as MR spectroscopy, cardiac imaging, liver imaging and brain imaging. Since 2011, she has been focusing her research on the brain using diffusion imaging, susceptibility weighted imaging, amide proton transfer imaging and arterial spin labelling (ASL). In 2013, she received the Stefan Fischer Prize for her development of a new accelerated ASL-based 4D-MRA sequence and obtained an opportunity to work as a neuro clinical scientist in the head office in Best, the Netherlands. During this three-month exchange program, she started a collaborative research project with Prof.dr.ir. Matthias van Osch in Leiden University Medical Center on ASL-based 4D-MRA. In March 2015, she obtained her master's degree in radiation diagnosis from Juntendo University Graduate School of Medicine, with her academic dissertation "Estimation of Mean Axon Diameter and Intra-Axonal-Space Volume Fraction in the Human Corpus Callosum: Diffusion Q-space Imaging with Low q-values".

In October 2015, she started a PhD at the C.J. Gorter Center for High Field MRI at Leiden University Medical Center under the supervision of Prof.dr.ir. Matthias van Osch. Her main research topics are the development and optimization of ASL-based 4D-MRA and perfusion techniques. From September to December in 2016, she was a visiting student at Nuffield Department of Clinical Neurosciences within the University of Oxford and started a collaborative research project with Dr. Thomas Okell under his supervision.

She finished her PhD in March 2018, and started a postdoctoral position in modeling and analysis of cerebral perfusion imaging at the Institute of Biomedical Engineering within the University of Oxford.

Publications that are part of the thesis

1. **Suzuki Y**, Okell TW, Fujima N, Chappell MA, van Osch MJP. Acceleration of Vessel-Selective Dynamic MR Angiography by pCASL in Combination with Acquisition of Control and Labeled Images in the Same Shot (ACTRESS). submitted to Magn Reson Med, in revision
2. **Suzuki Y**, Okell TW, Chappell MA, van Osch MJP. A Framework for Motion Correction of Background Suppressed Arterial Spin Labeling Perfusion Images Acquired with Simultaneous Multi-Slice EPI. Magn Reson Med 2018;00:1-13. https://doi.org/10.1002/mrm.27499
3. **Suzuki Y**, van Osch MJP, Fujima N, Okell TW. Optimization of the Spatial Modulation Function of Vessel-Encoded Pseudo-Continuous ASL and its Application to Dynamic Angiography. Magn Reson Med 2018;00:1-13. https://doi.org/10.1002/mrm.27418
4. **Suzuki Y**, Helle M, Koken P, Van Cauteren M, van Osch MJP. Simultaneous acquisition of perfusion image and dynamic MR angiography using time-encoded pseudo-continuous ASL. Magn Reson Med 2018;79(5):2676-2684.
5. **Suzuki Y**, Fujima N, Ogino T, Meakin JA, Suwa A, Sugimori H, Van Cauteren M, van Osch MJ. Acceleration of ASL-based time-resolved MR angiography by acquisition of control and labeled images in the same shot (ACTRESS). Magn Reson Med 2018;79(1):224-233.

Other Peer-Review Publication

6. van Osch MJ, Teeuwisse WM, Chen Z, **Suzuki Y**, Helle M, Schmid S. Advances in arterial spin labelling MRI methods for measuring perfusion and collateral flow. J Cereb Blood Flow Metab 2017:271678X17713434.
7. Sugimori H, Fujima N, **Suzuki Y**, Hamaguchi H, Ishizaka K, Kudo K. Fast acceleration of ASL-based time-resolved magnetic resonance angiography by acquisition of control and labeled images in the same shot (fast ACTRESS): An optimization study. Magn Reson Imaging 2017;43:136-143.
8. Yamashita K, Hiwatashi A, Togao O, Kikuchi K, Yamaguchi H, **Suzuki Y**, Kamei R, Yamasaki R, Kira JI, Honda H. Cerebral blood flow laterality derived from arterial spin labeling as a biomarker for assessing the disease severity of parkinson's disease. J Magn Reson Imaging 2017;45(6):1821-1826.
9. Kikuchi K, Hiwatashi A, Togao O, Yamashita K, Yoshimoto K, Mizoguchi M, Suzuki SO, Iwaki T, **Suzuki Y**, Honda H. Correlation between arterial spin-labeling perfusion and histopathological vascular density of pediatric intracranial tumors. J Neurooncol 2017;135(3):561-569.
10. Kamiya K, Hori M, Irie R, Miyajima M, Nakajima M, Kamagata K, Tsuruta K, Saito A, Nakazawa M, **Suzuki Y**, Mori H, Kunimatsu A, Arai H, Aoki S, Abe O. Diffusion imaging of reversible and irreversible microstructural changes within the corticospinal tract in idiopathic normal pressure hydrocephalus. Neuroimage Clin 2017;14:663-671.
11. Takemura MY, Hori M, Yokoyama K, Hamasaki N, Suzuki M, Kamagata K, Kamiya K, **Suzuki Y**, Kyogoku S, Masutani Y, Hattori N, Aoki S. Alterations of the optic pathway between unilateral and bilateral optic nerve damage in multiple sclerosis as revealed by the combined use of advanced diffusion kurtosis imaging and visual evoked potentials. Magn Reson Imaging 2017;39:24-30.
12. **Suzuki Y**, Hori M, Kamiya K, Fukunaga I, Aoki S, M VANC. Estimation of the Mean Axon Diameter and Intra-axonal Space Volume Fraction of the Human Corpus Callosum: Diffusion q-space Imaging with Low q-values. Magn Reson Med Sci 2016;15(1):83-93.
13. Hori M, Kamiya K, Nakanishi A, Fukunaga I, Miyajima M, Nakajima M, Suzuki M, **Suzuki Y**, Irie R, Kamagata K, Arai H, Aoki S. Prospective estimation of mean axon diameter and extra-axonal space of the posterior limb of the internal capsule in patients with idiopathic normal pressure hydrocephalus before and after a lumboperitoneal shunt by using q-space diffusion MRI. Eur Radiol 2016;26(9):2992-2998.

14. Kamagata K, Shimoji K, Hori M, Nishikori A, Tsuruta K, Yoshida M, Kamiya K, Irie R, Suzuki M, Kyogoku S, **Suzuki Y**, Sato N, Aoki S. Intersite Reliability of Diffusion Tensor Imaging on Two 3T Scanners. Magn Reson Med Sci 2015;14(3):227-233.
15. Sugimori H, Fujima N, **Suzuki Y**, Hamaguchi H, Sakata M, Kudo K. Evaluation of cerebral blood flow using multi-phase pseudo continuous arterial spin labeling at 3-tesla. Magn Reson Imaging 2015;33(10):1338-1344.
16. Togao O, Hiwatashi A, Keupp J, Yamashita K, Kikuchi K, Yoshiura T, **Suzuki Y**, Kruiskamp MJ, Sagiyama K, Takahashi M, Honda H. Scan-rescan reproducibility of parallel transmission based amide proton transfer imaging of brain tumors. J Magn Reson Imaging 2015;42(5):1346-1353.
17. Togao O, Yoshiura T, Keupp J, Hiwatashi A, Yamashita K, Kikuchi K, **Suzuki Y**, Suzuki SO, Iwaki T, Hata N, Mizoguchi M, Yoshimoto K, Sagiyama K, Takahashi M, Honda H. Amide proton transfer imaging of adult diffuse gliomas: correlation with histopathological grades. Neuro Oncol 2014;16(3):441-448.
18. Hori M, Yoshida M, Yokoyama K, Kamagata K, Kumagai F, Fukunaga I, Kamiya K, Suzuki M, Masutani Y, Hamasaki N, **Suzuki Y**, Kyogoku S, Hattori N, Aoki S. Multiple sclerosis: Benefits of q-space imaging in evaluation of normal-appearing and periplaque white matter. Magn Reson Imaging 2014;32(6):625-629.
19. Hori M, Tsutsumi S, Yasumoto Y, Ito M, Suzuki M, Tanaka FS, Kyogoku S, Nakamura M, Tabuchi T, Fukunaga I, **Suzuki Y**, Kamagata K, Masutani Y, Aoki S. Cervical spondylosis: Evaluation of microstructural changes in spinal cord white matter and gray matter by diffusional kurtosis imaging. Magn Reson Imaging 2014;32(5):428-432.
20. Kamiya K, Hori M, Miyajima M, Nakajima M, **Suzuki Y**, Kamagata K, Suzuki M, Arai H, Ohtomo K, Aoki S. Axon diameter and intra-axonal volume fraction of the corticospinal tract in idiopathic normal pressure hydrocephalus measured by q-space imaging. PLoS One 2014;9(8):e103842.
21. Sekine T, Amano Y, Takagi R, Matsumura Y, **Suzuki Y**, Murai Y, Kumita S. Four-dimensional flow magnetic resonance imaging assessment of hemodynamics in patients after extracranial-intracranial bypass surgery. J Nippon Med Sch 2013;80(1):2-3.
22. Fukunaga I, Hori M, Masutani Y, Hamasaki N, Sato S, **Suzuki Y**, Kumagai F, Kosuge M, Hoshito H, Kamagata K, Shimoji K, Nakanishi A, Aoki S, Senoo A. Effects of diffusional kurtosis imaging parameters on diffusion quantification. Radiol Phys Technol 2013;6(2):343-348.
23. Hori M, Fukunaga I, Masutani Y, Taoka T, Kamagata K, **Suzuki Y**, Aoki S. Visualizing non-Gaussian diffusion: clinical application of q-space imaging and diffusional kurtosis imaging of the brain and spine. Magn Reson Med Sci 2012;11(4):221-233.
24. Hori M, Aoki S, Fukunaga I, **Suzuki Y**, Masutani Y. A new diffusion metric, diffusion kurtosis imaging, used in the serial examination of a patient with stroke. Acta Radiol Short Rep 2012;1(1).
25. Hori M, Fukunaga I, Masutani Y, Nakanishi A, Shimoji K, Kamagata K, Asahi K, Hamasaki N, **Suzuki Y**, Aoki S. New diffusion metrics for spondylotic myelopathy at an early clinical stage. Eur Radiol 2012;22(8):1797-1802.
26. Amano Y, Sekine T, **Suzuki Y**, Tanaka K, Takagi R, Kumita S. Time-resolved three-dimensional magnetic resonance velocity mapping of chronic thoracic aortic dissection: a preliminary investigation. Magn Reson Med Sci 2011;10(2):93-99.
27. Watanabe H, Kanematsu M, Kitagawa T, **Suzuki Y**, Kondo H, Goshima S, Kajita K, Bae KT, Hirose Y, Miotani S, Zhou X, Fujita H. MR elastography of the liver at 3 T with cine-tagging and bending energy analysis: preliminary results. Eur Radiol 2010;20(10):2381-2389.
28. Nakamura T, Miyati T, Kasai H, Ohno N, Yamada M, Mase M, Hara M, Shibamoto Y, **Suzuki Y**, Ichikawa K. Bulk motion-independent analyses of water diffusion changes in the brain during the cardiac cycle. Radiol Phys Technol 2009;2(2):133-137.
29. Amano Y, **Suzuki Y**, van Cauteren M. Evaluation of global cardiac functional parameters using single-breath-hold three-dimensional cine steady-state free precession MR imaging with two types of speed-up techniques: comparison with two-dimensional cine imaging. Comput Med Imaging Graph 2008;32(1):61-66.

30. Tsuchiya K, Fujikawa A, Honya K, Nitatori T, **Suzuki Y**. Diffusion tensor tractography of the lower spinal cord. Neuroradiology 2008;50(3):221-225.
31. Arai N, Miyati T, Matsunaga S, Motono Y, Ueda Y, Kasai H, **Suzuki Y**, Matsuda T. [New method of determining regional fat fraction with modulus and real multiple gradient-echo (MRM-GRE)]. Nihon Hoshasen Gijutsu Gakkai Zasshi 2007;63(3):312-318.
32. Kanematsu M, Goshima S, Kondo H, Tsuge Y, Yokoyama R, Kajita K, Onozuka M, **Suzuki Y**, Van Cauteren M, Moriyama N. Gadolinium-enhanced multiphasic 3D MRI of the liver with prospective adaptive navigator correction: phantom study and preliminary clinical evaluation. AJR Am J Roentgenol 2007;188(4):W309-316.
33. Tsuchiya K, Fujikawa A, **Suzuki Y**. Diffusion tractography of the cervical spinal cord by using parallel imaging. AJNR Am J Neuroradiol 2005;26(2):398-400.

Review

1. **Suzuki Y**, Zimine I, Obara M, Okuaki T, Ogino T, Van Cauteren M. MR Perfusion Imaging Using Arterial Spin Labeling. JJMRM. 2007: 27(4): 239-252 (Japanese)

Book chapter

1. "k-t BLAST" in: Takahara T, Ougi K, eds. Clinical MRI at your fingertips (in Japanese: MRI応用自在). MEDICAL VIEW, 2004; 72-75, ISBN: 978-4-7583-0826-7
2. "Diffusion Weighted Imaging Sequence" in: Nishimura T, Yamada K, Ito H, eds. The vast expanse of diffusion and perfusion MRI for diagnostic imaging (in Japanese: diffusion, perfusion MRI 一望千里). MEDICAL VIEW, 2006; 24-28, ISBN: 978-4-7583-0659-1
3. "Parallel Imaging" in: Niitsu M, Isobe, T, Kamimaki T, Sato E, eds. MR・超音波・眼底　基礎知識図解ノート, 2012, ISBN: 978-4-307-07107-9

Patent

Suzuki, Yuriko. 2014. MR Imaging using Arterial Spin Labeling with Improved Temporal Resolution. International Publication Number, WO 2014/162237 A1, published October 9 2014. International Application Number, PCT/IB2014/060119, filed March 25 2014. Patent Pending.

Publications in conference proceedings

(only first authorship)

1. **Suzuki Y**, Okell TW, van Osch MJP. Acceleration of Vessel-Selective 4D-MRA by pCASL in combination with ACTRESS. P186, Proceesings of 26th Annual Meeting of ISMRM, 2018
2. **Suzuki Y**, Okell TW, Teeuwisse WM, Schmid S, van der Plas M, Chappell MA, van Osch MJP. Solving the dark-sides of multiband-ASL: A framework to correct for increased motion aftefacts in MB-ASL due to sharp transitions in the level of background suppression. P3616, Proceedings of the 25th Annual Meeting of ISMRM, 2017
3. **Suzuki Y**, van Osch MJP, Okell TW. Improved spatial encoding for vessel-selective pCASL: improving efficiency, minimizing mis-labeling, and shortening scan-time for artery specific MRA. P3617, Proceedings of the 25th Annual Meeting of ISMRM, 2017
4. **Suzuki Y**, Ogino T, Meakin JA, Suwa A, Ushijima D, Van Cauteren M. Improved Visalization of the Accelerated ASL-based Time-resolved MRA with Single Acquisition of Labeled and Control Imges. P879, Proceeding of the 23th Annual Meeting of ISMRM, 2015

5. **Suzuki Y**, Teeuwisse WM, Schmid S, Koken P, Van Cauteren M, Helle M, van Osch MJP. Simultaneous Acquisition of Perfusion Map and 4D MR Angiography by Means of Arterial Spin Labeling MRI. P720, Proceeding of the 22th Annual Meeting of ISMRM, 2014
6. **Suzuki Y,** Teeuwisse WM, Schmid S, Helle M, Van Cauteren M, van Osch MJP. Improving 4D PCASL Angiography by Combining Hadamard Time-Encoding with Look-Locker Readout. P2512, Proceeding of the 22th Annual Meeting of ISMRM, 2014
7. **Suzuki Y**, Fujima N, Sugimori H, Ogino T, Van Cauteren M. ASL-Based Time-Resolved MRA Acquiring Labeled and Control Images in a Single Look-Locker Like Acquisition. p2150, Proceeding of the 21th Annual Meeting of ISMRM, 2013
8. **Suzuki Y,** Van Cauteren M. Investigation of Diffusion Kurtosis Imaging of Organ with Plenty of Perfusion/Flow Effect. p3134, Proceeding of the 21th Annual Meeting of ISMRM, 2013
9. **Suzuki Y**, Van Cauteren M. Investigation of Liver Diffusion Kurtosis Imaging and Perfusion Effect. p4119, Proceeding of the 20th Annual Meeting of ISMRM, 2012
10. **Suzuki Y**, Kuroki Y, Van Cauteren M. Improving Accuracy in Measurement of Choline as a Predictor of Early Response to Neoadjuvant Chemotherapy: Correction of Internal Reference using External Reference. p3061, Proceeding of the 19th Annual Meeting of ISMRM, 2011